UNIVERSITÀ DEGLI STUDI DI PADOVA

DIPARTIMENTO DI INGEGNERIA INDUSTRIALE

CORSO DI LAUREA MAGISTRALE IN INGEGNERIA DEI MATERIALI

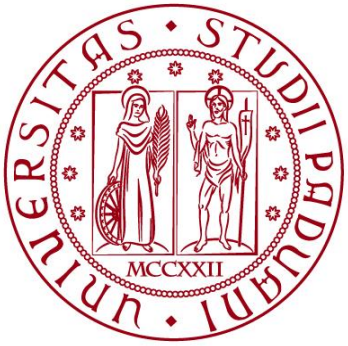

TESI DI LAUREA MAGISTRALE IN INGEGNERIA DEI MATERIALI

Zinc oxide nanowires decorated with gold nanorods for photovoltaic applications

Relatore: Prof. Alessandro Martucci
Correlatore: Prof. Alberto Vomiero

Laureando: Enrico Rossi
Matricola: 1132702

ANNO ACCADEMICO 2017-2018

Abstract

Solar cells are promising devices to convert solar energy into electricity. However, a consistent part of the absorbed radiation cannot be converted due to the relatively low efficiencies of the most common solar cell architectures.

Modern devices use nanomaterials technologies in order to improve both light absorption and charge transport properties in thin solar cells. Focusing on the optical properties, metallic nanoparticles exhibit plasmonic properties, which enable Sun light absorption at specific wavelengths. In particular, Sun radiation can induce LSPR (Localized Surface Plasmon Resonance), a collective oscillation of free electrons in the nanoparticle: this contributes to create more charge carriers in the active absorbing layer of the solar cell. Some effects related to LSPR which improve light absorption are strong scattering, near-field enhancement and direct as well as plasmon-induced energy transfers. In this work, gold nanorods were added at the surface of zinc oxide single crystal nanowires to exploit their plasmonic properties, improving light absorption.

Gold nanorods were synthetized using a seed-mediated growth, while zinc oxide nanowires were synthetized through a two-step hydrothermal method using hexamethylenetetramine (HMT) as shaping assistant.

The integration of the gold nanorods on the surface of ZnO nanowires was carried out by dropping the gold nanorod solution on the nanowire array. The presence of gold in the final composite system was proven by scanning electron microscopy (SEM) and XRD analysis.

The optical characterization allowed to demonstrate the absorption by ZnO at 377 nm, related to the absorption of photons with enough energy to create electron-hole pairs in the semiconductor. After gold deposition, two new absorption peaks showed up at the resonance wavelengths, due to transverse and longitudinal plasmonic bands of gold nanoparticles.

The photoluminescence properties of ZnO nanowires were tested before and after gold nanorod deposition. Without gold, ZnO excited at 325 nm showed two emission peaks, one in the UV region and one in the visible; the former was related to excitonic recombination, the latter was attributed to trap energy levels. The UV emission, called Near Band Emission (NBE), and the visible emission, called Deep Level Emission

(DLE), can be modulated by annealing treatments, which promote defects passivation and a suppression of DLE peak. Gold deposition contributed to increase NBE/DLE ratio in un-annealed samples, whereas an opposite trend was noticed in annealed samples. This may be explained in terms of LSPR: un-annealed samples are characterized by a visible emission able to excite gold, that acts like an electron pump from ZnO defect levels to its conduction band. Moreover, a bleaching effect on the characteristic zinc oxide near-band emission was seen after continuous exposition of the composite material to UV radiation. A hypothesized relation between the intensity of this phenomenon and the amount of gold deposited has been discussed, since higher nanorods concentrations were always related to lower quenching effects and vice-versa.

The results open up new prospects for successful implementation of gold nanorods in photovoltaic cells. Further research can be focussed on electrical properties to demonstrate the electrons flux increase due to gold nanorods LSPR, for example through IV curves before and after decoration. Moreover, some experiments can help the understanding of the energy transfer arising between gold and ZnO: a physical separation such as the deposition of Al_2O_3 layer between ZnO and Au may stop some transfers; photo-induced absorption (PIA) can point out faster processes than photoluminescence. Finally, alternative deposition methods such as spin-coating and electrodeposition may be useful to obtain a more homogeneous distribution of nanorods on ZnO nanowires.

Acknowledgements

I would like to express the deepest appreciation to my supervisors, Professor Alessandro Martucci and Professor Alberto Vomiero, who gave me the golden opportunity to work on this project. Their constant guidance and support significantly enhanced my academic development as well as my personal growth.

As far as nanomaterials are concerned Professor Alessandro Martucci represents the key figure who introduced me to this topic: my interest in it came from his valuable lectures.

Professor Alberto Vomiero made me feel an important figure in his research group. I will be forever grateful to him for introducing me to the research world, enabling me to understand the importance of scientific rigorousness, sustained efforts and collaboration between colleagues.

This thesis is nothing but the result of what I learnt from them: they were my primary sources of information and of valuable clarifications.

I am also indebted to everyone who helped me at Luleå University of Tecnhology. A special mention is deserved by the whole Vomiero's group of research, a group of brilliant people always ready to clarify my doubts.

Among all of them, I am deeply grateful to my co-supervisor Dr. Shujie You for her continuous and unconditional support at any time of my experimental work, especially when I needed a guide to overcome any kind of difficulty. It was a pleasure to share thoughts, expectations and many laboratory efforts with her.

I also want to thank Dr. Mojitaba Gilzan Kohan and Dr. Raffaello Mazzaro, who spent a lot of their time to help me with my experimental part, whenever I could not work alone. Their precious advice was fundamental to carry out my project successfully and, together with Dr. Shujie You, they represent to me the perfect inspiration of how a researcher should be.

I am thankful to the Teaching and Administrative Staffs of Università degli Studi di Padova and Luleå University of Tecnhology, for assuring a comprehensive and meaningful academic path.

I would like to express my greatest appreciation to all my fellow master students in Luleå for making the department much more than a working place: they and many other

Erasmus students shared with me precious moments both inside and outside the academic context. I firmly believe that living in a foreign country, sharing experiences and supporting one another made us grow more open-minded about other cultures and more self-confident.

Finally, I am sincerely grateful to any other person who contributed to make me the person I am today: my family for their unconditional love and for teaching me the values which really matter in life, such as kindness and respect for other people, supporting me morally and emotionally as well as economically; all my fellow students and friends in Padova for giving me strength and motivation to reach better results; all those friends who have been sharing precious life moments with me every day.

List of figures

Figure 1 - Carbon dioxide emissions in the last five years 2
Figure 2 - Net electricity generation: past, present and future 3
Figure 3 – Solar spectral energy distribution 5
Figure 4 – Photons of different energies interacting with a semiconductor 7
Figure 5 – Efficiency/cost ratio plot of the three solar cell generations 9
Figure 6 - NREL efficiency chart.. 9
Figure 7 - Silicon doping to obtain an n-type semiconductor. 12
Figure 8 - Recombination processes that occur in a semiconductor. 13
Figure 9 - Absorption coefficient in different semiconductors. 16
Figure 10 - Schematic illustration of the LSPR 17
Figure 11 - Resonance peaks of Ag and Au in different shapes 17
Figure 12 – Plasmonic properties are highly dependent from shape and size. 19
Figure 13 - Scattering by plasmonic metal nanoparticles. 21
Figure 14 - Near-field plasmonic effect 22
Figure 15 - Plasmonic effects of a nanoparticle at LSPR conditions 24
Figure 16 - Schematic representation of the two possible kind of band-gaps 26
Figure 17 - Schematic of the atomic structure and lattice polarity along the c-axis of the wurtzite ZnO crystal 27
Figure 18 - Energy band diagram showing ZnO possible defects emissions 29
Figure 19 - Nanorods plasmonic oscillations and effect of the aspect ratio on the plasmonic wavelength 31
Figure 20 - Schematic structure of the nanocomposite system obtained 35
Figure 21- Scheme of the two-step hydrothermal growth process to get ZnO nanowires 40
Figure 22 - Sample preparation in two different autoclaves. 41
Figure 23 - Schematic representation of the mechanisms proposed to explain silver role in Au NRs growth 43
Figure 24 - Gold deposition on ZnO nanowires 44
Figure 25 - Gold nanorods concentration gradient within one sample 45
Figure 26 - Batches look comparison 46

Figure 27 - Photoluminescence measurement settings. 49
Figure 28 - Photoluminescence spectrometer scheme used in Luleå University of technology 50
Figure 29 - Picture of the samples decorated with gold used in the laboratory and their names 53
Figure 30 - TEM pictures of Au nanorods 56
Figure 31 – Nanorods dimensions distributions coming from measurements on TEM pictures 57
Figure 32 - HREM and FFT confirm the gold nature of the nanorods 57
Figure 33 - XRD peaks are showed above, while the corresponding patterns of hexagonal wurtzite and cassiterite are expressed by black and red lines, respectively, at the bottom 59
Figure 34 - SEM pictures of ZnO nanowires 60
Figure 35 - Diameters distribution of three samples belonging to different batches. 61
Figure 36 - ZnO nanowires in a cross-section SEM image 61
Figure 37 - XRD analysis after Au decoration 62
Figure 38 - SEM images taken in two parts at different gold concentrations 63
Figure 39 - EDS analysis for qualitative measurement 64
Figure 40 - CTAB chemical structure 64
Figure 41 - SEM cross-section images after Au decoration on high concentrated sample 65
Figure 42 - Absorbance, transmittance and reflectance spectra of batch 1 ZnO samples 67
Figure 43 - Comparing transmittances of sample with different mean diameter nanowires 68
Figure 44 - Picture of the samples in batch 3 68
Figure 45 - Transmittance spectra of four different batches 69
Figure 46 - Reflectance spectra of four batches 69
Figure 47 - Tauc plots of batch 1 samples 71
Figure 48 - Photoluminescence of ZnO nanowires 72
Figure 49 - Annealing effect on 2E6 sample 73

Figure 50 - Plasma treatment as alternative to annealing 74
Figure 51 - Transmittance spectra of two bare ZnO samples, two "light" and two "dark" gold samples, referring to the colour and related to the concentration of gold inside. 76
Figure 52 - First derivative of the transmittance data 77
Figure 53 - Reflectance of 2E4 sample before (blue line) and after (red line) addition of gold 77
Figure 54 - NBE enhancement after decoration with gold 79
Figure 55 - Photoluminescence results before and after Au addition for not-annealed (6E2) and annealed (6E4) samples..... 80
Figure 56 - Sample 6E2 NBE and DLE peaks before and after gold addition, normalized to the highest value of each DLE 81
Figure 57 - Multiple emission scans of Au-decorated ZnO NWs 83
Figure 58 - Photoluminescence emissions on different spots of the same sample . 85
Figure 59 - Focus on the DLE for three dark and three light spots 86

List of tables

Table 1 - Seed layer solution details for a typical synthesis in the laboratory..... 38
Table 2 - Nanowires growth typical preparation 38
Table 3 - Batches and sample labels used in this research..... 51
Table 4 – Synthesized samples details..... 52
Table 5 - XRD data of FTO/ZnO system..... 58
Table 6 - Band-gap estimation of samples belonging to batches 1, 2, 3 and 7..... 71
Table 7 - Transverse plasmonic peak position for the four gold samples..... 75
Table 8 - NBE/DLE ratio values of not-annealed 6E2 sample..... 81

Table of contents

Abstract ..... **i**

Acknowledgements ..... **iii**

List of figures ..... **v**

List of tables ..... **ix**

Table of contents ..... **xi**

Introduction **1**

1.1 Background – From fossil fuels to renewable resources 1

1.2 Solar energy, photovoltaic technologies and solar cells 4

1.3 Solar cells: functionality and generations 6

1.4 Semiconductors for photovoltaics: structure and properties 10

1.4.1 Carrier concentration and semiconductor doping 10

1.4.2 Charge carrier recombination 12

1.5 The plasmonic effect 15

1.5.1 Plasmonics in solar cells 20

1.5.2 Light scattering 21

1.5.3 Near-field effect 22

1.5.4 Energy transfer: HEI and PIRET 23

1.6 Materials used: nanostructures supremacy 25

1.6.1 Zinc oxide nanowires properties 25

1.6.2 Gold nanorods properties 30

Objectives **33**

Experimental Part **35**

3.1 Nanocomposite development: FTO glass, ZnO and Au 35

3.1.1 A transparent conductive substrate: FTO glass 36

3.1.2 ZnO nanowire synthesis: hydrothermal process 36

3.1.3 Gold nanorods synthesis: the seed-mediated method 41

3.2 Gold deposition and further treatments 44

3.3 Morphological, structural and optical characterization 46

3.3.1 Structural and morphological characterization: XRD and electron microscopies 47

3.3.2 Optical characterization: UV-Vis and photoluminescence spectroscopies 48

3.4 List of the samples 51

Results and discussion 55

4.1 Morphological and structural characterization 55

4.1.1 Gold nanorods – TEM characterization 56

4.1.2 ZnO nanowire structure and morphology: XRD and SEM 58

4.1.3 Au nanorods decoration on nanowires: XRD, SEM and EDS 62

4.2 Optical characterization 65

4.2.1 Pristine ZnO nanowires – UV-vis and PL results 66

4.2.2 ZnO/Au system: plasmonic enhancement 75

4.2.3 ZnO/Au system: single emission photoluminescence 78

4.2.4 ZnO/Au system: multiple emission photoluminescence 83

Conclusion and future work 89

Italian Summary 91

Bibliography 95

Chapter 1

Introduction

1.1 Background – From fossil fuels to renewable resources

The demand of energy is increasing year by year due to industrialization, modernization, people's increasing living standards and population growth, increased by 2 billion in just one generation. The first one is considered to be the key factor in pushing the energy need to higher levels, expecting an electricity generation increase from $20\ x\ 10^{15}\ W \cdot h$ in 2010 to $31.2\ x\ 10^{15}\ W \cdot h$ in 2030[1]. Nowadays the main problem is trying to supply this exceeding amount of energy through renewable sources rather than not sustainable ones, but this is not an easy task.

Combustion of fossil fuels (which are oil, coal and natural gas) is still in the first place on the ranking of energy consumption worldwide[2]. This is mainly due to the transport sector, in which it is even more difficult to find an alternative energy source to gasoline and diesel, even if there have been progresses in the usage of renewable fuel derived from biomass. For example, fuels from Fischer-Tropsch synthesis, bioethanol, biomethanol and biohydrogen are getting more and more attention because they guarantee a strong improvement about energy security and environmental concerns[3], key factors to prefer other resources over common fuels.

The 1970s were very important for the future development of renewable resources. As a matter of fact, the oil crisis happening in that period permitted for the first time a more convinced focus on the need of alternative energy sources for terrestrial use.

The firm belief about the importance of improving sustainable energy sources lies primarily in the awareness of the climate change issue, with carbon dioxide (CO_2) depicted as one of the greenhouse gases responsible of global warming together with methane (CH_4), nitrous oxide (N_2O) and chlorofluorocarbons (CFCs). From the Intergovernmental Panel on Climate Change (IPCC) of 2011 some events have been identified as clear sign of greenhouse effect increase.

The most critical ones are:

- the 1990s were the warmest decade since records began;
- global snow cover and the extent of ice caps has decreased by 10% since 1960s;
- non-polar glaciers are undergoing widespread retreat;
- global mean sea level rose by 0.1-0.2 m during the 20th century.

To stop this trend, many governments have accepted the assessment of the United Nations Framework Convention on Climate Change (UNFCCC) that the maximum mean global temperature value accepted is 2°C above the pre-industrial level, and to do so it is fundamental to reduce the greenhouse gas emissions in the atmosphere, meaning to reduce the combustion of fossil fuel or to catch the emission at point sources before their dispersion in the air. The domestic reduction of greenhouse gas emissions has to reach the 40% by 2030 and 80% by 2050, from a 1990 baseline, according to European Union guidelines; moreover, the target is to supply the 30% of total energy requirement from renewable sources by 2030, and 100% by 2050[4].

The much higher concentration of CO_2 in comparison with the other gases brings the belief that its greenhouse effect is also much stronger. Even if it is not the only source, burning of hydrocarbons surely releases a huge quantity of this gas. As a matter of fact, in June 2018 the atmospheric CO_2 concentration is reaching about $410\ ppm$, while in the pre-industrial times the value was $280\ ppm$, meaning an increase of 46.4%[5].

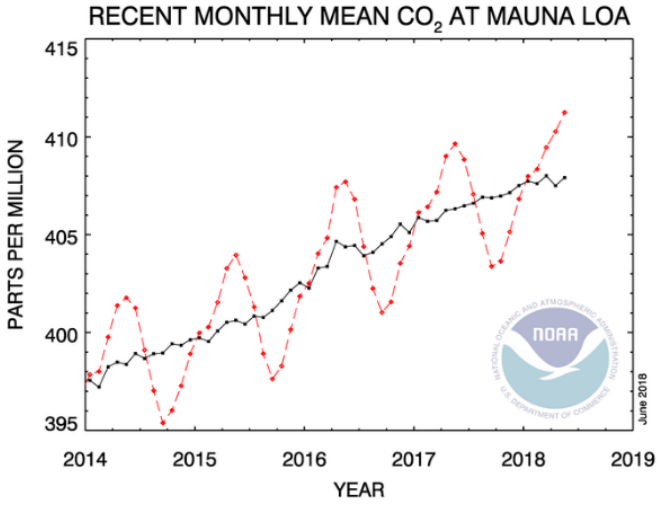

Figure 1 - Carbon dioxide emissions in the last five years. The dashed red line with diamond symbols represents the monthly mean values, centred on the middle of each month. The black line with the square symbols represents the same, after correction for the average seasonal cycle. From ref. (5).

Moreover, reserves of easily extracted oil, gas and coal are losing reliability due to both geological depletion and restricted policy from energy exporting countries to gain political leverage[6]. This does not mean that fossil fuels are running out right now, but that continuing to mine coal and pumping oil will lead to dangerous rise in global temperature and level of air pollution.

The only way to control the global warming and at the same time provide all the growing population the necessary amount of energy is to rely more on renewable energy sources, meaning they are inexhaustible within the time horizon of humanity. Some authors, for example M. Jacobson and M. Delucchi, state that it is possible to provide worldwide energy for all purposes through wind, water and sunlight; their plan would require only 0.41% and 0.59% more of the world's land for footprint and spacing, respectively, and that the barriers obstructing this project are mainly social and political[7]. As a matter of fact, there are many forms of renewable energies: wind power, hydropower, solar energy, geothermal energy and bio energy are the most popular.

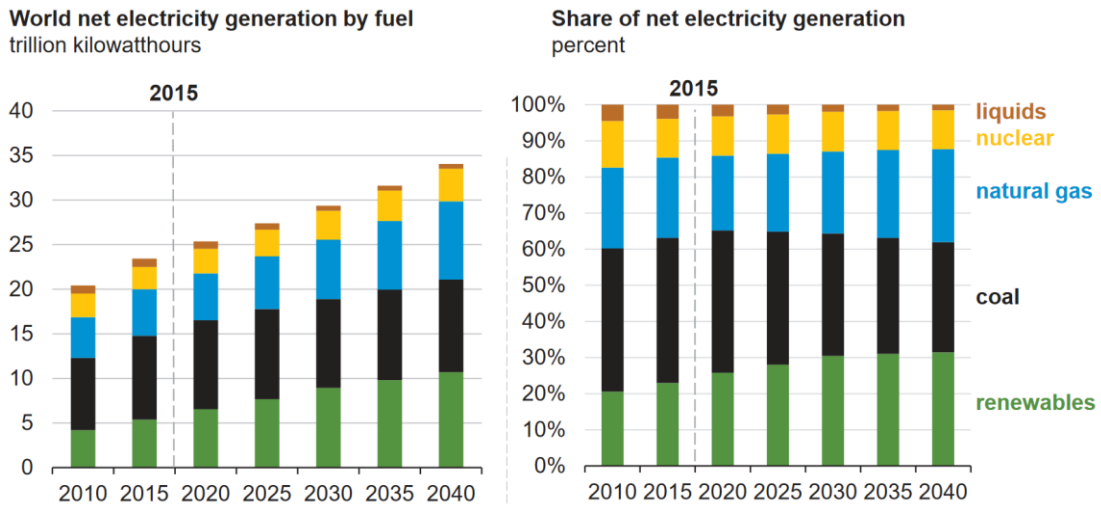

Figure 2 - Net electricity generation: past, present and future. On the left, the expected increase of the world net electricity generation in the next years, in terms of trillion kilowatthours. On the right, the fuels used to get the electricity per year. From ref. (8)

It is possible to refer to many books and authors for an in-depth examination of all the renewable energies technologies, for example B. Towler[1], M. Letcher[9] and A. Sayigh[10]. The work of this thesis deals with solar energy technology. For this reason, we will focus on the description of this specific renewable energy source in the following section.

1.2 Solar energy, photovoltaic technologies and solar cells

The Sun is such a big source of energy that every day provides all the global needed energy 10,000 times. This huge amount of energy comes from the interior of the Sun, according to overall reaction:

$$4\ {}^{1}H \rightarrow\ {}^{4}He + 2e^{+} + 2\nu_e + Energy \qquad (1)$$

The radiant power per unit area perpendicular to the direction of the Sun outside the Earth's atmosphere, at the mean Earth-Sun distance is essentially constant. This radiation intensity is referred to as "solar constant" or "air mass zero (AM0) radiation".
Even if the value of the radiation is still under debate, the generally accepted value is $F_S = 1365\ \frac{W}{m^2}$ (NASA value[11]). When the sun is at an angle θ from the Zenith, the air mass (AM) is defined as:

$$AM = \frac{1}{\cos\theta} \qquad (2)$$

When increasing the air mass values, keeping constant all the other atmospheric variables, the energy reaching Earth's surface is attenuated.

Moreover, the spectrum of the Sun emission at around 6000 Kelvin is similar to a blackbody spectrum, whereas the radiation reaching Earth's surface has got a different spectrum because of the peculiar transmittivities through the atmosphere of the different wavelengths. Of all the initial energy, in fact, a fraction is absorbed passing through the layers of the Earth's atmosphere, so that terrestrial sunlight is very different both in intensity and in spectral composition. In the upper atmosphere energy is absorbed to dissociate molecules N_2 and O_2 into atoms; in the ionosphere energy is absorbed for the ionization of chemical individuals; in the ozonosphere energy absorption leads to O_3 dissociation. Then, part of the transmitted radiation is reflected into space according to the number of *albedo* which takes into account the reflection due to Earth's surface, aerosols, dust, ashes and clouds; 31% of the radiation is calculated to be reflected in these ways. A little part is also absorbed by the clouds. At this point the energy successfully absorbed by the surface is ~46% of the initial irradiated energy and it is approximately

$E_S = 1.2 \times 10^{17} W$, which is converted into heat, into kinetic energy in the wind, takes part in the hydrological Earth circle and production of biomass[12].

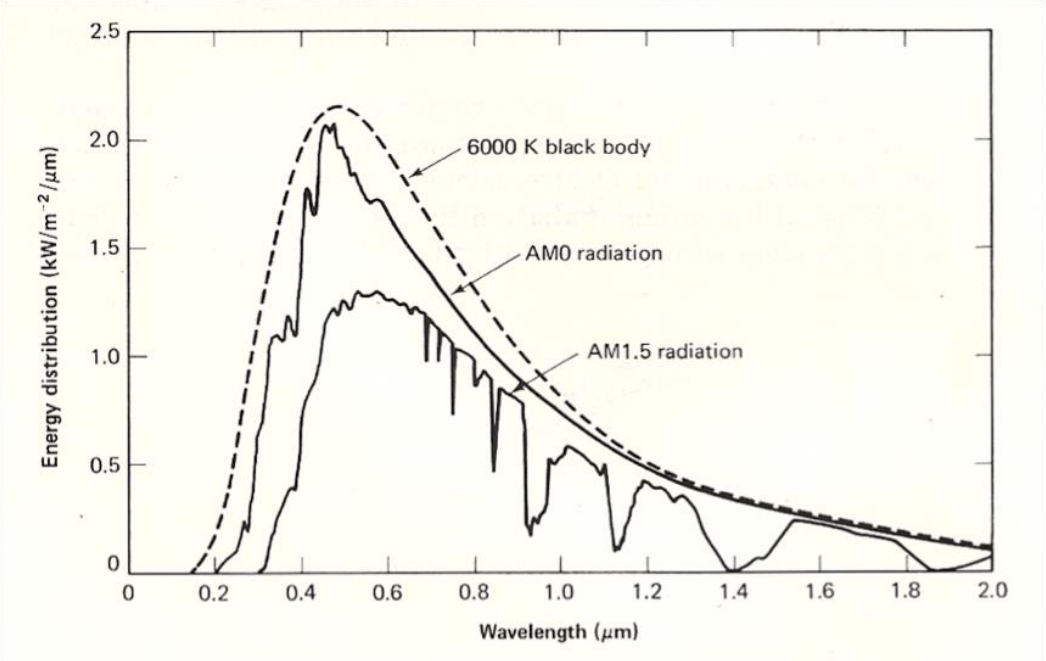

Figure 3 – Solar spectral energy distribution. Radiation spectra coming from the Sun if it were a black body, solar constant (AM0 radiation) and radiation on Earth's surface following the terrestrial standards (AM1.5 radiation). From ref. (13)

The part of solar energy successfully reaching Earth's surface can be used in different ways and it is easy to find examples of its implementation in countless technologies worldwide and in very different social realities.

Industrial processes such as sterilising, pasteurising, drying, hydrolysing, washing and cleaning could need mean temperature levels in the range $60°C \div 120°C$. A system made up of solar collectors, a circulating pump and a storage tank is common in industries where hot water or low-pressure steam are employed to achieve such processes[14].

In modern buildings, heating and air conditioning are responsible of big energy consumption, and they also have an impact on carbon dioxide emissions: passive solar technologies based on buoyancy and evaporative effects can be exploited to heat and/or cool house spaces[15]; water heating is a major process daily used in buildings, too: solar assisted water systems are possible and are thought to be valuable alternatives to get a positive impact on economic, environmental and energy conservation perspectives[16].

In developing countries, consumption of food and water are major everyday issues: solar energy can be used to cook food using box type and parabolic solar cookers[17]; saline water, abundant in the world, can be converted to potable water through membrane and non-membrane desalination processes assisted by solar energy, and used in that regions which are under severe stress due to water scarcity and pollution[18].

The dominant technology able to exploit this big amount of solar energy and to directly convert it in electricity, without the intermediation of any heat engine, is photovoltaics (PV). Among all the renewable energies technologies, PV has become the one with the highest growth rate (more than 40% per year over the past decade[19]), showing the increasing interest in its application despite its high cost.

A solar cell structure is always composed by some kind of light absorbing material capable of activate the photovoltaic effect, the direct responsible of the conversion from sunlight to electrical energy. When light, and specifically photons, shine on a photovoltaic cell, they can transfer their energy to the electrons of the absorbing material, making them pass from the valence to the conduction band, where they're free to move. This can only happen if the photon energy is higher than the energy band gap of the semiconducting material, which means that the incident radiation needs to be of a suitable wavelength. In the meantime, a hole is generated in the valence band to keep the energetic balance constant. In a p-n junction, excited electrons and holes can both move, in their respective bands, under the effect of an electric field, making them effective charge carriers and giving the possibility to drive a current through a circuit.

1.3 Solar cells: functionality and generations

It is possible to define three solar cells generations. Each generation is characterized by some peculiar materials or technology, so that they can achieve different efficiencies and they can be more or less expensive. Efficiency is defined as the ratio between power output and power input when the cell undergoes STC (standard test conditions), that are solar irradiance equals to $1000\ \frac{W}{m^2}$, temperature on the device kept constant at 25°C, no wind and air mass number equals to 1.5 (AM1.5, defines how solar rays go through atmosphere and what's the angle between solar rays and the reference point on Earth). Higher efficiencies mean more sunlight successfully transformed into usable electricity;

however, monocrystalline silicon solar cells, the most popular commercialized ones, reach efficiencies around 20-25%, meaning that three quarters of the solar radiation cannot be converted into electricity. There must be some processes happening in the cell that drop the efficiency. The main reason is that the solar radiation shining on the cell covers a wide range of wavelengths, and only some of the photons can be absorbed from the device. Knowing the absorption process happening in a semiconductor, it's clear that only some of that photons will eventually participate in the creation of charge carriers: photons with energies below the band-gap are not absorbed by the electrons because their energy is not high enough to overcome the energetic barrier between the two electronic bands; photons with energies above the band-gap will excite electrons, that will eventually lose the excess energy by thermalization processes, which can be described as heat loss phenomena i.e. loss of efficiency. It is possible to refer to this issue as spectral mismatch, underling the fact that the wide solar spectrum cannot be entirely absorbed by the cell active layer. This also explains why multi-junction cells show higher efficiencies: they can absorb a wider range of wavelengths, due to the presence of more band-gaps, simultaneously removing thermalization processes, so that a bigger portion of the solar spectrum can be captured and successfully converted into electricity.

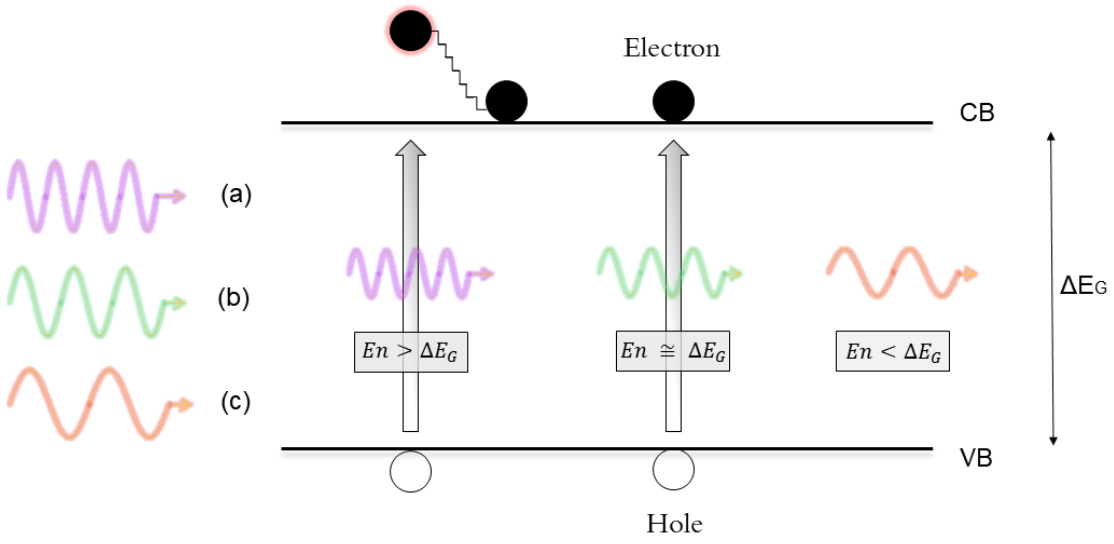

Figure 4 – Photons of different energies interacting with a semiconductor. The blue photon has higher energy than the band-gap: it can create electron-hole pair, but the excess energy will be lost as heat. Red photon has lower energy than the band-gap: it will be transmitted through the semiconductor. Green photon has the same energy (or slightly higher) than the band-gap: it will create electron-hole pair.

The target of the photovoltaic research is to improve solar cell efficiency without increasing the cost. That is, the evolution trend from the first to the third generation solar cells is to increase the efficiency/cost ratio, as it can be seen from Figure 5 in the next page.

The first generation includes crystalline silicon solar cells, which are the most popular and have been dominating the markets for years, also because they are the one mainly seen on rooftops. Moreover, the knowledge about this kind of material has been supported by microelectronic industries for many years, so that processes have been optimized and improved a lot by now. The working principle is very simple and is based on the processes characterizing a p-n junction. Some advantages are the huge availability of the raw material, good efficiency (up to 27.6%, Figure 6) and a long life time; the main disadvantage is the high energy consumption requested for their production, that also turns into a long payback time, that is the period of activity of the solar cell needed to produce the quantity of energy employed to make the cell itself.

Second generation devices were designed to limit cost by reducing the quantity of material used, and they are known as thin-film technologies. Amorphous Si, copper indium gallium selenide (CIGS) and CdTe are the most popular solar cells belonging to this category. They are characterized by lower efficiencies than first generation solar cells, but they show some degrees of flexibility that allows a wider range of applications and design possibilities. However, the lower efficiencies represent a strong limitation to their stabilization in the market.

Third generation, the last one, has the aim of increasing efficiencies, possibility exploiting different techniques: intermediate band solar cells (IBSCs) are constituted by more than one band-gap, or rather, are characterized by more energy levels within the energy gap, which are able to absorb photons simultaneously with the original band-gap related absorption; hot carriers cells permit to collect carriers excited at higher energies avoiding thermalization processes; multiple exciton generation solar cells manage to create more than one electron-hole pair after the absorption of one highly energetic photon; optical nanoantennas can be added to solar cells in order to strongly confine the electromagnetic field within it, storing the incident energy in a localized surface plasmon mode and increasing the chance of absorption by the surrounding semiconductor. This energy conversion is only efficient when the absorption rate in the semiconductor is larger

than the reciprocal of the typical plasmon decay time, as otherwise the absorbed energy is dissipated in the metal by ohmic damping[20]. Cells of the third generation that exploit these processes are for example dye-sensitized cells, perovskite cells, organic cells, quantum dots cells and multi-junction cells.

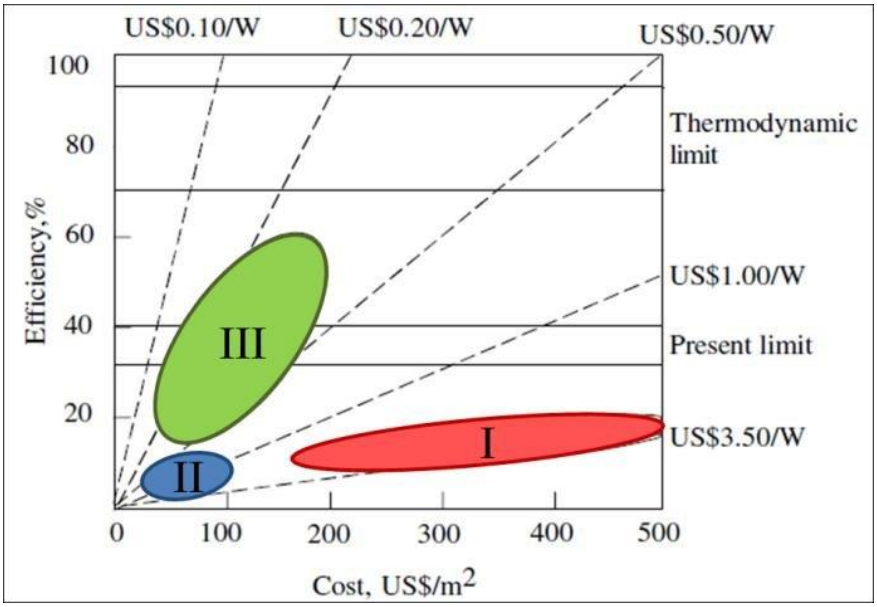

Figure 5 – Efficiency/cost ratio plot of the three solar cell generations. The plot shows the trend to improve the efficiency per cost ratio from first to third generation solar cells. From ref. (21)

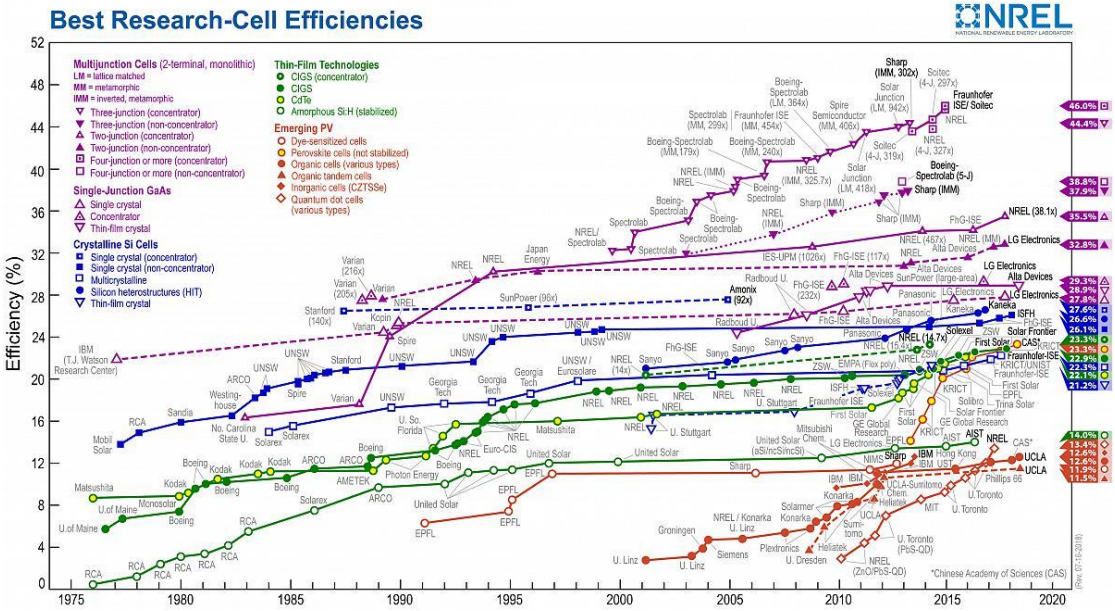

Figure 6 - NREL efficiency chart. Evolution in the efficiencies of different kind of solar cells: crystalline Si cells (first generation), thin-film technologies (second generation), emerging PV and multijunction cells (third generation). This plot is courtesy of the National Energy Laboratory, Golden, CO.

1.4 Semiconductors for photovoltaics: structure and properties

Generally, referring to semiconductors for photovoltaic means to consider atoms from group IV such as Ge and Si; a combination of atoms from group III (like Al, Ga and In) with atoms from group V (P, As and Sb) or combination between group II (Zn, Cd) with group VI (S, Se, Te). The structure of the semiconductor can be made up of one single element, can be a compound (GaAs, InP, CdTe) or even an alloy (Si_xGe_{1-x}).

The crystal lattice of semiconductors is composed by atoms linked together with covalent bonds: the electrons responsible of these bonds at 0°K are unable to move, they fill up the valence band while the conduction band is completely empty; on the other hand, at higher temperatures, the electrons can access to some higher permissible quantum mechanical energy state, which falls in the conduction band, acting as they would act in a conductor material. This is possible because the band-gap is not as big as the one typical of insulators, thus electrons can be excited more easily and the chances increase together with temperature: in general, a material with band-gap $< 3\ eV$ is considered a semiconductor, while if the energy bandgap is $> 3\ eV$ the material is defined an insulator. Considering the photovoltaic field of application, it is significant to underline that different semiconductors are characterized by different band-gap values, thus electrons absorb different energies (in this case in the form of a photon) to be excited into the conduction band, leaving a hole in the valence band, with the possibility of being accelerated in a circuit to obtain current. Therefore, it is clear that the choice of the material, as long as the tuning of the band-gap, is of major importance to absorb specific wavelengths and to convert light into electric power.

1.4.1 Carrier concentration and semiconductor doping

It is possible to directly modify the semiconductors structure by addition of impurities in their lattice, modifying their properties; when this happens, the semiconductor passes from being intrinsic to doped and one of the most important differences to be noted is the concentration of charge carriers. In an intrinsic semiconductor, the carrier concentration refers to the number of free electrons in the conduction band or the holes in the valence band; in un-doped condition, the two

concentrations must be equal, because an electron reaching the high energy state always involves the generation of a hole in the valence band:

$$n = p = n_i \tag{3}$$

Where *n* is the free electron concentration, *p* is the hole concentration and *ni* is called intrinsic concentration. Therefore, in this case, the carrier concentration depends only on band-gap and temperature; lower band-gaps and higher temperatures will favour higher carrier concentrations because of easier electrons detaching from their bonds. In the temperature range between 200 K and 400 K, the intrinsic concentration *ni* varies approximately according to:

$$n_i^2 \cong T^3 e^{-\Delta E_G / kT} \tag{4}$$

where *T* is the absolute temperature (in Kelvin), ΔEG is the band-gap energy and *k* is the Boltzmann constant. It is evident how an increase in the temperature can quickly generate many carriers. In pure semiconductors, the intrinsic concentration *ni* is in the range $10^6 \div 10^{13}\ cm^{-3}$; for example, silicon has an intrinsic carrier concentration $n_i \cong 9.65 \times 10^9\ cm^{-3}$ at 300 K[22].

It is possible to vary the carrier concentration by adding impurities in the semiconductor lattice. There are two possible interesting approaches: one is to insert in the structure some atoms of an element constituted by a larger number of electrons in its outer shell, while the other is doing the same thing with atoms consisting of a lower number of electrons. For example, considering silicon, which belongs to group IV, it is possible to substitute some silicon atoms with group III or group V atoms, for instance Al and P, respectively. Aluminium will produce a disequilibrium in the carriers concentration increasing the hole concentration, having one electron less than the substituted silicon: in this case the obtained material is a p-type semiconductor; on the other hand, phosphorous will create a disequilibrium in favour of electrons, having one electron more in comparison with the silicon: it is defined an n-type semiconductor (Figure 7). The effect is a disparity in the number of carriers, so that they can be divided in majority and minority carriers: in n-type semiconductors the majority carriers are the

electrons, while in p-type semiconductors the majority carriers are the holes. For this reason, when light creates electron-hole pairs, the increase of the majority carriers is not as evident as the one of minority carriers.

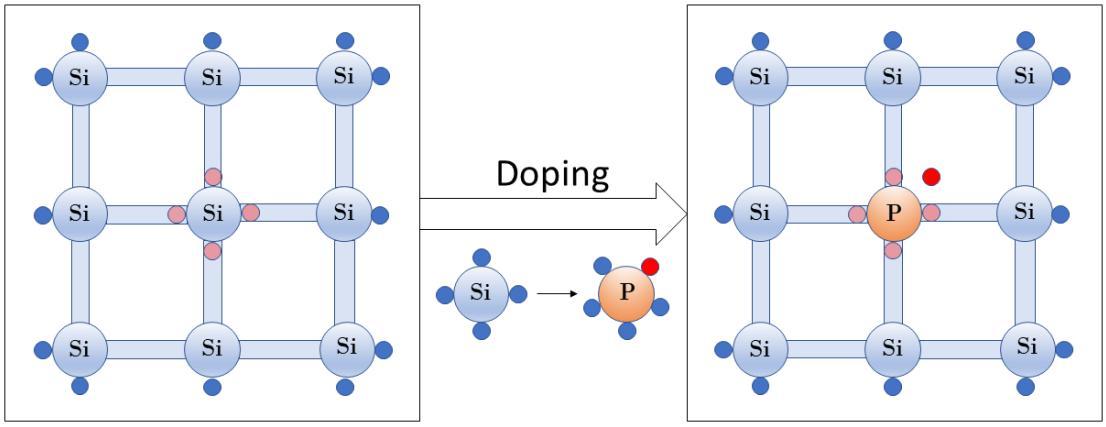

Figure 7 - Silicon doping to obtain an n-type semiconductor. The central Si atom is bonded through four shared electrons. When it is substituted with a P atom, one more electron enters the lattice. In this way, the density of electrons will be easily higher than the holes density, and the semiconductor becomes an n-type semiconductor.

In an n-type semiconductor, some excess electrons will eventually occupy pre-existing holes; in a p-type semiconductor, some excess holes will eventually catch pre-existing electrons. Therefore, in both cases, it is possible to observe a decrease in the number of the minority carriers, explained by the mass action law:

$$np = n_i^2 \tag{5}$$

In each kind of doping there is an increase of the majority carriers combined with a decrease of the minority carriers, and the product of their concentration depends on the intrinsic concentration, which in turns depends on temperature as said before.

1.4.2 Charge carrier recombination

In a solar cell, a large number of carriers is desired. To obtain this, a doping of the original semiconductor is possible; another way is to enhance light absorption and interaction with light, to create a larger number of electron-hole pairs. However, a process exists that strongly limits this possibility: it is called recombination. In fact, in solar cells,

recombination restores the non-equilibrium light generated electron hole pair population to its thermal equilibrium value.

In a bulk semiconductor, three different recombination processes are possible:

- Radiative (or band-to-band) recombination;
- Non-radiative (or Schockley-Read-Hall) recombination;
- Auger recombination;

where radiative and Auger recombination are basic properties of the specific semiconductor material used, while the non-radiative recombination depends on the quality of the material, and in particular on the defect density. The three processes can be schematically represented as follows:

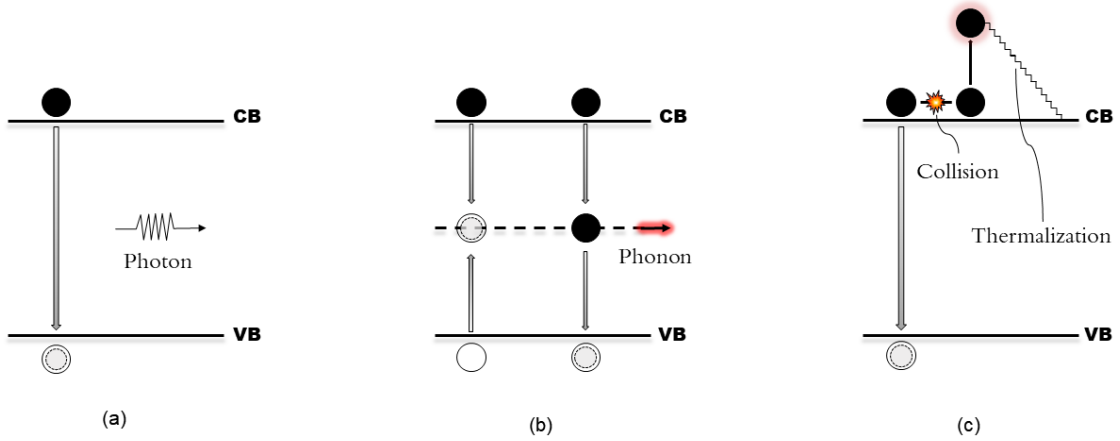

Figure 8 - Recombination processes that occur in a semiconductor. Radiative recombination is so-called because implies the emission of a photon (a); non-radiative recombination implies the emission of a phonon when an electron and a hole recombine in a trap state or when an electron reaches a hole after passing a trap state within the band-gap (b); Auger recombination implies the transfer of energy to another electron through collision, which afterwards loses energy in the form of heat by a thermalization process.

Radiative recombination deals with an electron that moves from the conduction band (high energy state) to a hole in the valence band (low energy state), resulting in the emission of a photon with an energy equal to the band-gap energy (Figure 8a). This process is more likely to happen in direct band-gap materials rather than indirect ones. As a matter of fact, the radiative recombination coefficient, which is directly proportional to the rate of recombination, is bigger for direct band-gap materials ($10^{-9} \div 10^{-11}\, cm^3/s$) than indirect band-gap materials ($10^{-13} \div 10^{-15}\, cm^3/s$)[23]. This also means that in indirect bandgap materials there should be a different recombination process to be

considered, and this is the trap-assisted recombination. It is really difficult to obtain a highly pure semiconductor; there will be always a certain degree of impurities growing inside the material. In fact, these impurities actively generate new energy levels within the band-gap, called trap levels, which can catch delocalized free carriers. As distinct from radiative recombination, in this case the energy is re-emitted in form of phonons (Figure 8b). This process is considered to be the most important one related to solar cell efficiency loss. Lastly, in the Auger recombination an electron recombines with a hole in a band-to-band transition; differently from a radiative recombination, here the resulting energy is given off to another electron (Figure 8c) or to a hole. It is known that this carrier will tend to decrease its energy state to the edge, through a dissipation process called thermalization: specifically, electrons emit some phonons decreasing their energy until an energy level near the band edge is reached. This kind of process is common in highly doped materials.

As stated before, an excitation can increase the number of minority charge carriers that will eventually recombine to reach their equilibrium state. Lifetime is the average time that a carrier spends in an excited state between its recombination and photogeneration. Usually it is common to refer to minority carrier lifetime because, after photogeneration of new electron-hole pairs, the increase in the number of majority carriers is negligible as compared to the one of minority carriers. An expression for the minority carrier lifetime is given by:

$$\tau = \frac{\Delta n}{R} \tag{6}$$

where τ is the carrier lifetime, Δn is the excess minority carrier concentration and R is the corresponding recombination rate. Additionally, it is important to underline that recombination processes can occur both on the surface and in the bulk of the semiconductor, so that the effective lifetime (τ_{eff}) is related to the bulk lifetime (τ_b) and to the recombination velocity of the surfaces (τ_s) in this way:

$$\frac{1}{\tau_{eff}} = \frac{1}{\tau_b} + \frac{1}{\tau_s} \tag{7}$$

Furthermore, it is possible to break up the bulk lifetime τ_b into the three different processes contribution to recombination (Figure 8):

$$\frac{1}{\tau_b} = \frac{1}{\tau_{rad}} + \frac{1}{\tau_A} + \frac{1}{\tau_{SRH}} \tag{8}$$

where τ_{rad} is the radiative lifetime, τ_A is the Auger lifetime and τ_{SRH} is the non-radiative (Shockley-Read-Hall) lifetime.

On the surface, instead, recombination processes occur especially due to the crystal lattice interruption, where the structure periodicity is undermined by the presence of incomplete dangling bonds. However, it is possible to intervene directly on the semiconductor surface to complete these dangling bonds through a process called passivation: the growth of a supplementary layer on the surface (for example silicon nitride on silicon solar cells) or thermal treatments such as annealing can accomplish this task.

1.5 The plasmonic effect

One of the main problem responsible to slow down photovoltaic growth is the high cost of this technology. The expense is mostly related to photoactive layer material cost, commonly silicon. Therefore, one way to reduce the overall cell cost is to use less material, so build thinner photoactive layers; however, this leads to low light absorption, because the light path length becomes shorter, meaning lower efficiency. In fact, the absorption coefficient determines how far in the material photons of a certain wavelength can travel before being absorbed: it is clear that low absorption coefficient would let photons penetrate deeper in the material, and, if the active layer is thin, this could lead the absorption process not to happen in time. The absorption coefficient depends on the material and on the wavelength of the incident light, because photons can be absorbed or not according to the material band-gap. Semiconductors show a sharp edge in the absorption coefficient related to their band-gap: photons with lower energy cannot be absorbed efficiently thus the coefficient is zero. For higher energy photons, instead, it is still possible to excite electrons to the conduction band, even if in solar cells this is not

related to efficiency enhancement because the excess energy will be lost as heat following a thermalization process (Figure 4).

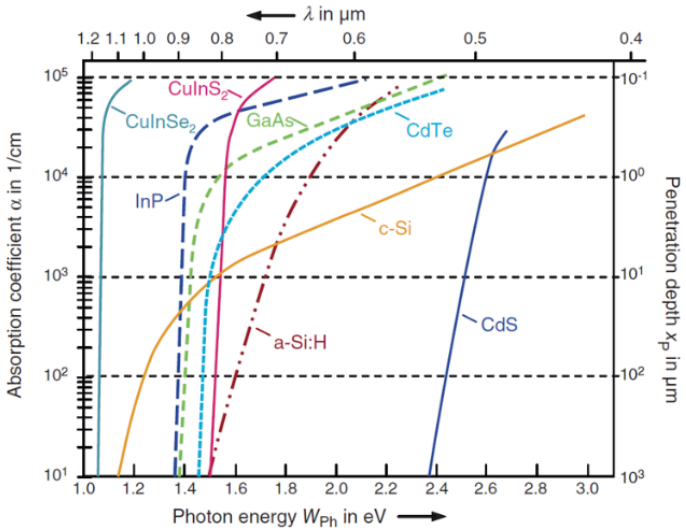

Figure 9 - Absorption coefficient related to wavelength in different semiconductors. In direct semiconductors, the steep curve is related to the band-gap, which represents the minimum energy for the photon to be absorbed. Crystalline silicon (c-Si) has a smoother curve being an indirect semiconductor, that is a phonon is also needed to complete the absorption of a photon. From ref. (24)

Light trapping is a way to improve solar cell performances, and it has been achieved modifying different kinds of solar cells, for example organic cells, thin film silicon cells and dye-sensitized cells through the addition in the device of periodic nanostructures, diffraction gratings or metallic nanoparticles[25,26]. One of the typical methods was to use surface textures such as inverted or upright pyramids to improve scattering inside the cell, but this approach is unsuitable for thin solar cell for two reasons: first, an efficient texture would be thicker than the photoactive layer; second, the texture would enlarge the surface area, increasing minority carrier recombination hence leading to higher recombination losses[20].

The metallic nanoparticles (NPs) approach is advantageous because of the easy and numerous possibilities existing to supplement nanoparticles in the active absorbing layer, on the surface or on the back of the cell. Their function is to scatter the incident light and trap it in the semiconductor or enhance the absorption through strong near field effect arising in the nanoparticle surroundings[20]; these processes will be discussed later in this chapter.

Metals can be considered plasmas from an electromagnetic point of view: they're made up of fixed, positive ion cores surrounded by mobile electrons, whose collective oscillations can be exploited to improve solar cell optical properties. Briefly, the increased light absorption derives from larger scattering cross section and near-field intensification, possible when a condition called localized surface plasmon resonance (LSPR) is reached. When the nanoparticle size is similar or lower than the wavelength of an incident radiation, a strong interaction can originate between the electromagnetic field and the free conduction electrons of the metal NPs (Figure 10).

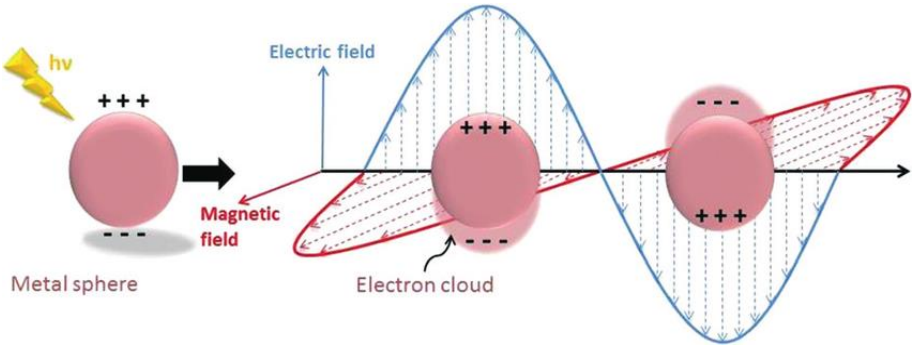

Figure 10 - Schematic illustration of the LSPR. The free electrons of a metal nanosphere starts to oscillate coherently when a radiation of a certain wavelength interact with the metal. From ref. (27)

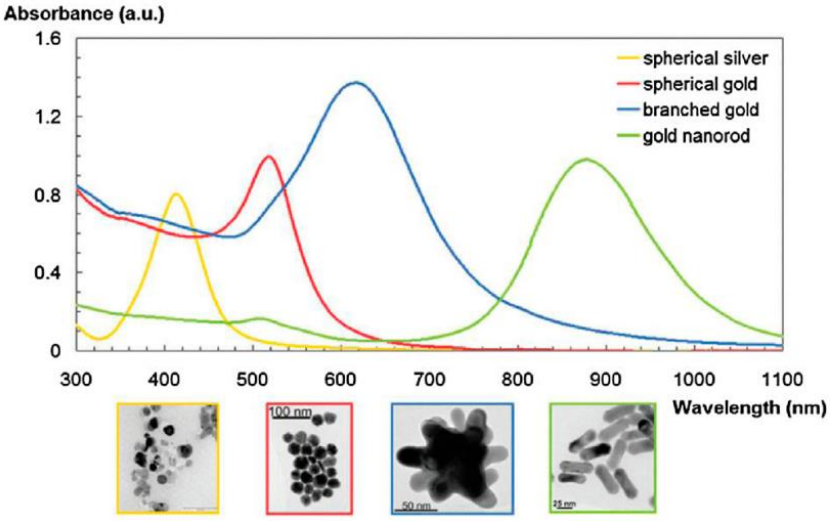

Figure 11 - Resonance peaks of Ag and Au in different shapes. Silver and Gold spherical nanoparticles show plasmonic resonance at ~ 420 nm and ~ 520 nm respectively; Au nanoparticle of different shapes show different peak positions: plasmonic resonance is strongly dependent by size, shape and material of the nanoparticles. From ref. (28)

The strongest possible interaction arises when the frequencies of the incident light and of the electrons oscillation are equal. Plasmonic nanostructures of noble metals such as copper, silver and gold show high absorption cross-sections and great charge carrier mobility; for these materials the resonances occur mainly in the visible regions of the electromagnetic spectrum.

It is important to notice that, given the solar radiation spectrum received from Earth's surface (Figure 3), resonance can produce enhanced absorption exactly at the wavelengths characterizing the maximum intensity of solar radiation, so that it is a phenomenon perfectly fitting photovoltaic applications. Moreover, it is possible to further tune the absorption position on the spectrum modifying the nanoparticle dimensions.

One characteristic of the plasmon resonance is that it is very sensitive to changes in shape of the nanoparticles, and it is also sensitive to variations in dielectric properties of the surrounding medium. Modulation of nanoparticle shape (the surrounding medium is often fixed and not interchangeable for certain applications) allows to control the wavelengths for which resonance is activated, meaning that it is possible to tune resonance effects (i.e. absorption) on prearranged wavelengths. Nanoparticles size heavily affects the interaction with light: from Mie scattering theory for spherical particles, it is possible to approximate NP scattering cross section (σ_{sca}) and absorption cross section (σ_{abs})[29]:

$$\sigma_{sca} = \frac{k^4}{6\pi} |\alpha|^2 \tag{9}$$

$$\sigma_{abs} = kIm(\alpha) \tag{10}$$

where k is the wave number and α is the particle polarizability, which for small spherical particles can be calculated as:

$$\alpha = 3V_p \frac{\varepsilon - \varepsilon_m}{\varepsilon + 2\varepsilon_m} \tag{11}$$

where V_p is the particle volume, ε is the dielectric function of the NP material and ε_m is the dielectric function of the surrounding medium, both wavelength dependent. For this approximation to be acceptable, conditions $ak \ll 1$ and $|m|ak \ll 1$ must be satisfied,

where a is the particle radius and m is the relative refractive index of the particle in the medium. Equation 11 is modified when the nanoparticle is ellipsoidal, following the electrostatic (or dipole) approximation[29]:

$$\alpha_i = V_p \frac{\varepsilon - \varepsilon_m}{\varepsilon_m + L_i(\varepsilon - \varepsilon_m)} \tag{12}$$

for $i = 1, 2, 3$ representing the dimensions and L_i geometry factors along these directions; in spheres $L_i = 1/3$ which leads again to equation 11.

Equations 9 – 12 express the dependence of scattering and absorption from NP size (V_p), electrical properties of NP material as well as surrounding medium ($\varepsilon, \varepsilon_m$), NP shape ($L_i$) and of course wavelength. Considering NP size, σ_{sca} varies with V_p^2 while σ_{abs} varies with V_p: absorption dominates for smaller nanoparticles which are mainly used for solar glazing or therapeutic applications, while for photovoltaic applications larger nanoparticles are more efficient since scattering is improved. In fact, when NPs interact with light radiation and a resonant condition is reached, the originated surface plasmons can afterwards decay through non-radiative processes (mainly release of heat) when interband or intraband excitations occur in the conduction band; or through radiative processes with emission of photons, *i.e.* scattering[30].

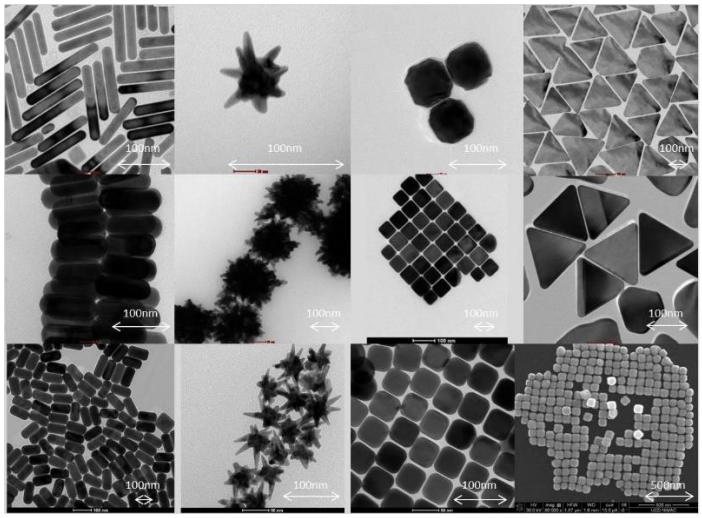

Figure 12 – Plasmonic properties are highly dependent from shape and size. For gold, the most typical shapes are spherical and rod-like, but many other shapes can be obtained. Library of nanoparticle shapes: TEM and SEM micrographs gold nanoparticles. By Dr. Željka Krpetić (CBNI,UCD).

If metal NPs can enhance light absorption in plasmonic solar cells, in dye-sensitized solar cells this improvement comes from the dye; however, it has been shown that gold nanospheres of $40\,nm$ in diameter present an absorption cross-section five orders of magnitude higher than conventional absorbing dyes, while gold nanorods are even better because they offer the same performance at lower dimensions, showing per-micron absorption and scattering coefficients one order of magnitude higher than those of nanosphere: in particular high AR nanorods along with smaller effective radius are optimized photoabsorbers, high AR nanorods with larger effective radius act better as scattering objects[31]. Moreover, this effective optical tunability is not possible in dyes, giving nanoparticles a second advantage. A deeper analysis about differences between nanorods and nanoparticles considering plasmonic properties will be presented in the following section.

1.5.1 Plasmonics in solar cells

The first aim in photovoltaic field is to improve photon absorption, because it results in the improvement of photon-to-electron conversion efficiency, too. That's why the study of new photovoltaic technologies was heavily focussed on metallic nanostructures able to generate plasmonic resonance. Just to recall the general concept of the previous paragraph, surface plasmons set at the interface between the metal and the surrounding dielectric material and originate from collective oscillation of free electrons given by the metal nanostructure. A further step is necessary to understand how this phenomenon can lead to an increased absorption, thus increased solar cell efficiency. Actually, this enhancement can be achieved through different mechanisms:

- light scattering;
- near-field enhancement;
- hot electron injection (HEI);
- plasmon-induced resonance energy transfer (PIRET).

Light scattering and near-field enhancement simply guide and focus photons toward the semiconductor material, which is entitled to represent the ultimate source of electron hole pairs; thus, the only photons able to produce them are the ones with energies above the semiconductor band-gap. It is possible to refer to this mechanisms as photonic effects.

The remaining processes, HEI and PIRET, deal with energy transfer that can arise even for energies below the semiconductor band-gap, depending, instead, on the nanomaterial physical and geometrical properties.

1.5.2 Light scattering

Scattering causes an increase in the path length of the photons through the absorbing medium, which is the semiconductor active layer, hence raises the probability of absorption. This is also possible through a decrease of the reflections on the irradiated surface, when the NPs are placed on the top surface and so the light can previously interact with them. Scattering effect helps to overcome the problem of non-absorption related to photons transmitted through the active layer, in particular when this is very thin. A metal NP set on the interface between a semiconductor and an electrolyte will preferentially scatter light towards the material with larger refractive index, which in most case is represented by the semiconductor[32]. Therefore, a very powerful possibility is to add NPs on the top active layer surface as well as at the bottom surface: this can lead to a back-and-forth path through which photons will eventually be absorbed.

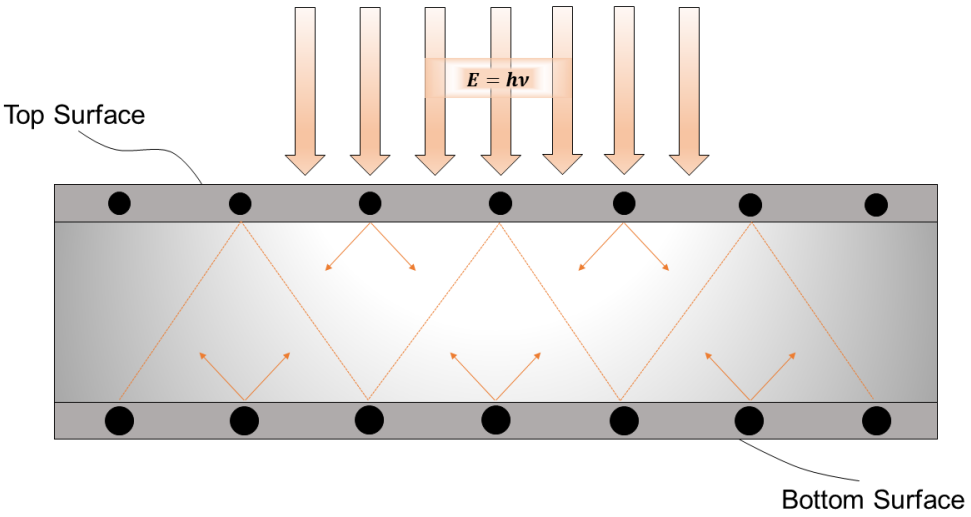

Figure 13 - Scattering by plasmonic metal nanoparticles. When a radiation interact with the semiconductor, metal nanoparticles scatter light in the direction of the active layer; instead, nanoparticles at the bottom surface can reflect back photons towards the absorbing layer, generating a back-and-forth path. When the resonance wavelength is reached, the scattering cross-section is higher and so it is the effect.

1.5.3 Near-field effect

The second mechanism, the near-field enhancement, is the confinement of a high energy electromagnetic field at the surface of plasmonic structures. This kind of effect can be related to two different propagation systems: surface plasmon polaritons (SPPs) and localized surface plasmon resonance (LSPR). The first possibility is found on planar metal films, where the near-field originated by the collective electrons oscillation propagating along the surface. Therefore, the absorption enhancement is brought from the propagation of this near-field along the surface, which is particularly effective on thin-film solar cells, where a full absorption is hard to get (Figure 14a). On the other hand, LSPR occurs in materials characterized by a curved or kinked surface, where the plasmons are enclosed in the nanoparticle volume without the possibility of propagation on a planar film, as SPPs can do; thus, in this case, the high energy near-field effect is localized at the NP surface (Figure 14b and Figure 14c).

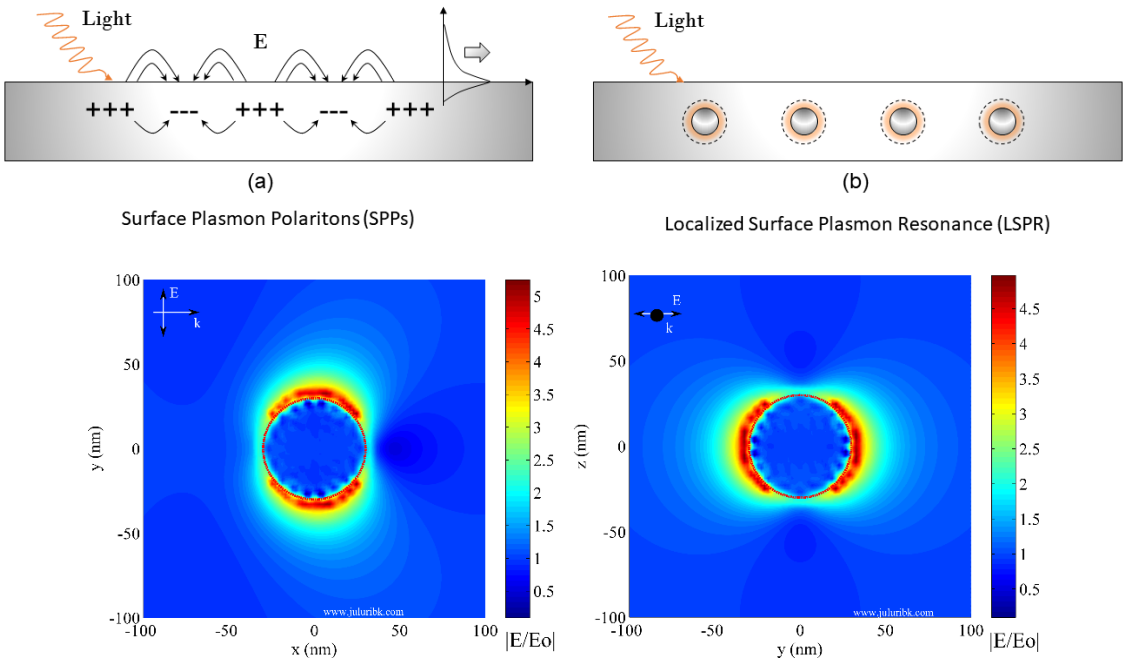

Figure 14 - Near-field plasmonic effect. The interaction with a radiation of the resonance wavelength leads to the formation of concentrated electromagnetic field which can propagate on a planar thin surface (a) or limited around a nanoparticle (b). Below, the near-field enhancement around a 60 nm gold spherical nanoparticle in water at LSPR (532 nm) using Discrete Dipole Scattering (DDSCAT). From ref (33)

Dimensions and shape of the NPs are of primary importance to understand the near-field effect, because the confinement is highly dependent on the resonant mode profiles

that can originate. For example, a spherical NP shows one fundamental LSPR mode, while a rod-shaped NP exhibits two LSPR modes, considering the presence of two different axial directions (transversal and longitudinal). In this light concentration mechanism, it is possible to consider the NPs such as optical antennas that manage to gather photons in the near semiconductor material, hence increasing electron-hole pair formation through a radiative process. The rate of pair generation is proportional to the square of the local electric field intensity, so that the higher the field intensity, the higher the number of electron hole pairs created.

The semiconductor must have the time to exploit this field enhancement: therefore, a relation with the plasmon life-time is expected. In fact, it is only when the plasmon decay rate is smaller than the absorption rate of the semiconductor that the process can be considered efficient[20]; the probability of absorption increase if the near-field effect lasts longer, thus when the plasmon life-time is longer.

1.5.4 Energy transfer: HEI and PIRET

Finally, transfer mechanisms are also possible in order to improve solar cells efficiencies. The first one deals with the generation of plasmon-induced hot carriers. The near-field manages to excite metal electrons to a higher energy state (above the Fermi energy level) through intraband or interband transitions; afterwards, it is possible to move these hot carriers directly from the metal to the semiconductor conduction band. The injection is possible if the energy achieved by the carrier (E_{hc}) is higher than the difference between the work function of the metal (φ_m) and the electron affinity of the semiconducting material (χ_s), referred to as Schottky barrier (φ_{Sb})[34]:

$$(E_{hc}) > \varphi_{Sb} = \varphi_m - \chi_s \tag{13}$$

If the energy is not enough to overcome the Schottky barrier $(E_{hc} < \varphi_{Sb})$, then a relaxation is needed through electron-electron or electron-phonon collisions, with loss of heat. Another limitation comes from the fact that HEI is only possible when NP and semiconductor are in direct contact between each other.

Another possibility is a resonant energy transfer, known as plasmonic-induced resonant energy transfer (PIRET) that is a specific kind of the broader mechanism called

Förster resonance energy transfer (FRET), where a donor and an acceptor interact through a dipole-dipole coupling arising within a certain distance. In the case of PIRET, plasmonic materials act as donors, giving energy to the acceptors that are the absorber elements in the solar cell. The energy transfer comes from the non-radiative decay of the surface plasmon; the acceptors can be the semiconductor material, a dye, perovskite or others: in any case, knowing the photovoltaic effect, the transferred LSPR dipole coming from the plasmonic material can afterwards create electron hole pairs inside the acceptor, which can be divided and collected[34]. The interesting fact about this process is that it is possible to take advantage of photons with lower energies, evading the band-gap energy constriction. The difference between this mechanism and the light trapping ones is that in PIRET it is possible to couple and employ low energy states; the difference with HEI is that PIRET does not require a perfect alignment along the Fermi energy level of the metal NP; then, PIRET does not have the limitation represented by the Schottky barrier. On the other hand, PIRET can only occur if the acceptor is located within the decay length of the plasmonic field and when the absorption spectra of semiconductor and metal overlap somewhere.

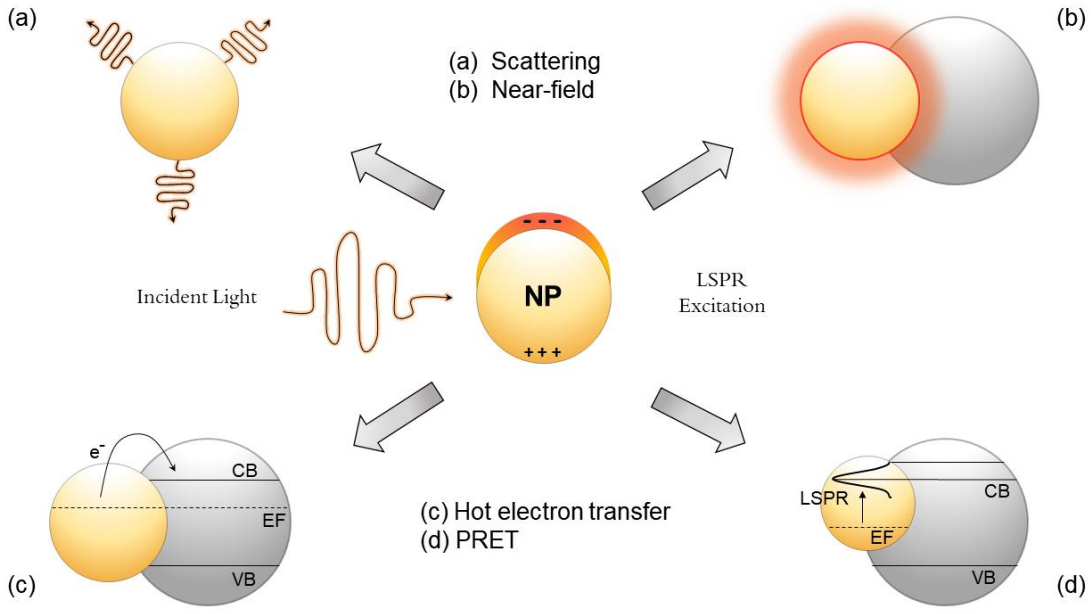

Figure 15 - Plasmonic effects of a nanoparticle at LSPR conditions. The light can be scattered (a), can produce a near-field effect (b), can promote the transfer from the metal to the semiconductor of hot electrons (c) or promote lower energy electrons after excitation with LSPR (d).

1.6 Materials used: nanostructures supremacy

In this research, two fundamentals materials were used: zinc oxide nanowires (ZnO NWs) and gold nanorods (Au NRs), both defined as nanomaterials.

Today, a single internationally accepted definition for nanomaterials does not exist: different organizations define nanomaterials in different ways[35]. According to ISO/TS 27687:2008, nanomaterial is "*a material with any external dimension in the nanoscale or having internal structure or surface structure in the nanoscale*", where nanoscale is defined as "*the size range from approximately* $1\ nm$ *to* $100\ nm$"[36]. It's possible to notice that a nanomaterial can have more than one dimension in the nanoscale, so a further clarification is needed. According to the British Standards Institution, nanoparticles are nano-objects with three eternal nanoscale dimensions, whereas nanofibers have two similar exterior nanoscale dimensions and a third larger dimension. Nanorods and nanoplates are nanoparticles where the longest and the shortest axes lengths are different. According to this definition, nanowires are included within the nanofibers.

1.6.1 Zinc oxide nanowires properties

Zinc oxide is a semiconducting material characterized by wide direct band-gap of $3.37\ eV$ at room temperature and large exciton binding energy of $60\ meV$ at room temperature.

Direct band-gap is present when the minimum energy in the conduction band and the maximum energy in the valence band share the same value of the crystal momentum; instead, when there's a difference in the crystal momentum the band-gap is called indirect. Silicon solar cells are the most common in the market (par. 1.3) and silicon is an indirect band-gap material; therefore, it can be interesting to understand the consequences in using one kind of band-gap or the other. Focusing on optical properties, direct band-gap materials show stronger optical transitions between valence and conduction bands than indirect semiconductors; in the latter, absorption or emission of a photon must be combined with absorption or emission of a phonon to accomplish the necessary momentum variation (Figure 16). Being this process harder to succeed, also the absorption will be harder in silicon solar cells (and in general in indirect semiconductors), which must be thick in order to get a larger number of photons, to rise the probability of

absorption. On the other hand, the minority carrier diffusion length must be considered, too. The diffusion length should be bigger than the thickness of the cell, in order to effectively collect carriers. Even if silicon solar cells must be thick to enhance absorption (to overcome the difficulties of the indirect band-gap), minority carriers can move longer before recombining, that is they have higher minority carrier diffusion lengths. Instead, ZnO-based solar cells can be thinner because the absorption is efficient (direct band-gap) and even if the diffusion length is shorter, is good enough to collect carriers. Therefore, both direct and indirect band-gap semiconductors can be used to make solar cells.

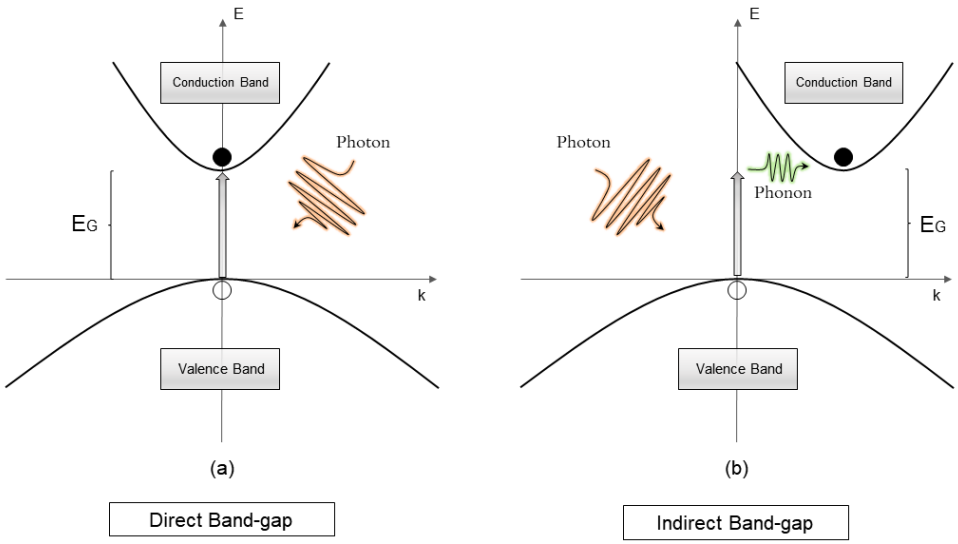

Figure 16 - Schematic representation of the two possible kind of band-gaps. A direct band-gap semiconductor can directly absorb a photon to create electron-hole pairs (a); an indirect band-gap semiconductor needs the intermediation of a phonon because conduction and valence bands present different crystal momentum values on the wavenumber (k) axis (b).

ZnO is also characterized by a high exciton binding energy. The exciton is the quasiparticle originated by the electrostatic attraction between electron and hole, so it arises when a photon can create electron-hole pairs. When the binding energy is high, the emission related to the excitonic radiative recombination process is very sharp even at room temperature and it can be used in applications such as LEDs.

Furthermore, ZnO is environmental friendly (it doesn't contain heavy metal elements), it has high electron mobility (up to $1000\ cm^2Vs^{-1}$ in an isolated nanowire) and can be fabricated with different technologies and many morphologies, among which 1D nanostructures are particularly interesting for light harvesting[37].

The most common ZnO crystalline structure is the hexagonal wurtzite structure with lattice parameters $a = 0.3296, c = 0.52065\ nm$[38], where the lack of a symmetry centre gives to ZnO piezoelectric properties. It's possible to imagine ZnO structure as a succession of alternating planes of tetrahedrally coordinated O^{2-} and Zn^{2+}along the c-axis (Figure 17), where the ionized species have been taken into account considering the relation between oxygen, highly electronegative, and zinc, barely electronegative.
This high bond polarity promotes the wurtzite structure formation rather than the zinc-blende one, where the tetrahedrally bonds have lower polarity.

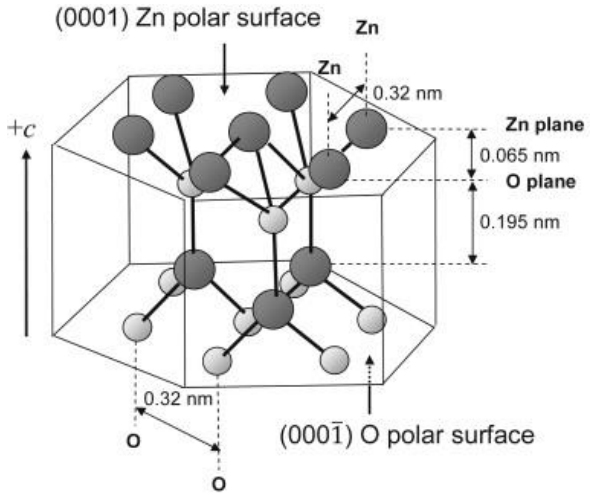

*Figure 17 - Schematic of the atomic structure and lattice polarity along the c-axis of the wurtzite ZnO crystal. From ref. (*39*)*

Being the ZnO bond polar, the stacking sequence of atomic layers is asymmetric along the c-axis and there are two possible crystallographic planes: Zn-terminated surface (0001) contains cations and it's called Zn-polarity surface; O-terminated surface $(000\bar{1})$ contains anions and it's called O-polarity surface[39]. This results in a normal dipole moment and spontaneous polarization along the c-axis as well as a variance in surface energy and chemical response[38], while along different axis this discrepancy isn't found: it will be shown later that this has an effect on the growth of anisotropic structures such as nanowires.

Optical properties are of primary importance in photovoltaic applications. ZnO, as a semiconductor, absorbs photons of a certain wavelength to create electron-hole pairs, which afterwards are collected as charge carriers in order to get electricity. Figure 9 was used to show that semiconductor materials are characterized by an absorption edge related

to their band-gap: electrons in the valence band can get the energy to move to the conduction band only if the energy supplied is enough, that is the energy gap between these two bands (band gap E_G). As previously stated, ZnO has a band-gap of ~ 3.3 eV, but it's really sensitive to morphology, presence of impurities, size and shape. Sometimes, a band-donor transition can dominate when the bulk of a ZnO single crystal is probed, showing a band-gap of 3.15 eV[40]; band-gap is also very sensitive to alloying coming from foreign species, for example ZnO nanowires have variable band-gap in the range 3.35 eV to 3.65 eV when doped with different Mg content[41]. Deposition and growth methods can extensively modify band-gap values, depending on the structural morphologies and crystal defects obtained. Electrodeposited nanowires fabricated with different salts can lead to different band-gaps: 3.42 eV from $Zn(NO_3)_2$, 3.36 eV from the same salt but in presence of hydrogen peroxide, 3.32 eV from $Zn(ClO_4)_2$; however annealing at 400°C in air produces a red-shift to 3.27 eV for these nanowires regardless of the anions, showing thermal treatments effects on the band-gap[42].

A very common procedure to estimate band-gap starts from UV-vis measurements and continues with the drawing of the so called "Tauc plot". It was found that the optical absorption intensity was related to the difference between the photon energy and band-gap through the equation:

$$(\alpha h\nu)^{1/n} = A(h\nu - E_G) \tag{14}$$

where α is the absorption coefficient, h is the Planck's constant, ν is the frequency of the photon, A is the proportionality constant, E_G is the band-gap and n denotes the electric transition in this way: $n = 1/2$ for direct allowed transitions, $n = 3/2$ for direct forbidden transitions, $n = 2$ for indirect allowed transitions and $n = 3$ for indirect forbidden transitions. Generally, allowed transitions are more likely to happen and ZnO is a direct semiconductor, so $n = 1/2$ was taken. The Tauc plot arises when plotting $(\alpha h\nu)^{1/n}$ vs $h\nu$; the obtained curve should show a region of linearity corresponding to the band-gap, whose value can be extrapolated to the x-axis intercept. This was the method used to estimate band-gap values, and results will be presented in the experimental part.

Photoluminescence properties are of primary importance in ZnO common applications such as white light-emitting devices, UV laser diodes and photodetectors. The luminescence of ZnO shows typically two emission peaks: a band edge ultraviolet (UV) emission peak, caused by exciton recombination, and a broad visible band emission peak, caused by the presence of different intrinsic defects in the material, especially on the surface. The source of the latter has been extensively studied, but the topic is still controversial: among all the possible defects, oxygen vacancies (V_O) are the most likely candidate to be the responsible of the green emission in that region (Figure 18). However, surface conditions and photoluminescence responses are heavily dependent on the synthesis method, growth mechanism and further treatments; also position and concentration of defects (both intrinsic and extrinsic ones) easily vary among samples. Annealing treatment is commonly used to achieve a passivation of the defects, leading to an increase of the ratio between the near band emission and the deep level emission (NBE/DLE ratio). Moreover, annealing can remove shallow defects and contaminations modifying oxygen absorption and desorption on the ZnO surface, which affect the photoconduction during UV irradiation. Indeed, the NBE peak is associated with free exciton recombination across the band gap: more intense peaks are related with less recombination traps within the band gap.

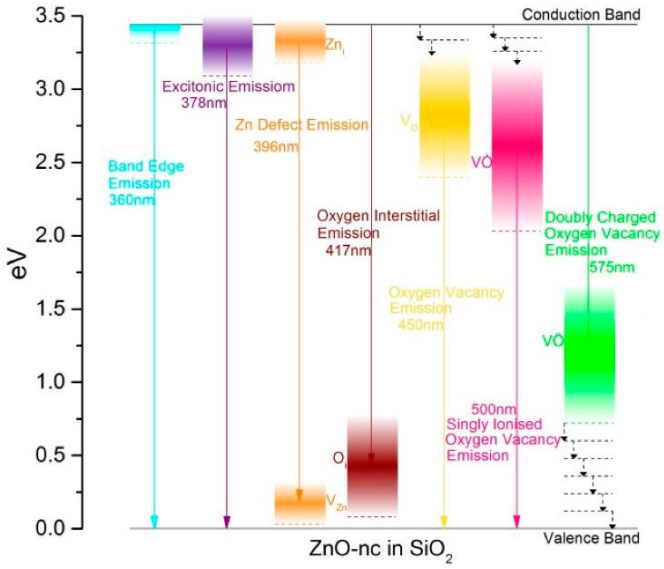

Figure 18 - Energy band diagram showing ZnO possible defects emissions. The main emissions come from oxygen related defects. From ref. (44)

A.Khayatian et al.[43] showed that annealing at high temperatures (over 300°C) can lead to a decrease of the UV emission, thus two processes have to be taken into account: release of the surface-attached chemical elements can increase NBE, but high temperatures can also create new defects, worsen the UV emission intensity.

1.6.2 Gold nanorods properties

As stated in paragraph 1.5, nanostructures of gold can exhibit plasmonic properties enhancing light absorption in solar cells. Such as the other noble metals, silver and copper, gold strongly absorbs in the visible; in fact, plasmonic absorption depends on size and shape of the material, as well as on dielectric properties of the surrounding medium. Therefore, different absorption peaks are expected for various gold nanostructures, for example spherical nanoparticles, nanorods or branched nanostructures (Figure 12). Among them, especially in the wet chemistry field, spherical nanoparticles have been intensely studied because of the possibility to obtain very stable particles by surfactant support. In this methods, Au NPs derives from the reduction of the precursor, in most cases chloroauric acid ($HAuCl_4$) or gold chloride ($AuCl_3$), by some reducing agent. Different reducing agents result in different shape and size distribution, so it's really important to use the most suitable one as well as control aging time, concentration, nature of different constituents and reduction technique[45]. M. Benkovicova et al.[46] presented a hot injection synthesis method to prepare large-scale self-assembled plasmonic nanostructures in which particles dimensions and size distribution were controlled by the utilization of different surfactants.

The possibility of tuning the plasmonic resonance on specific wavelengths varying nanostructures size and shape is also really interesting. A. Liu et al.[47] give a comprehensive guide about synthetizing many gold nanostructures (rods, cages, plates et al.) with near-infrared plasmonic resonance. As a matter of fact, differently from spherical nanoparticles, which only show plasmonic resonance at one wavelength, Au NRs can absorb light according to two plasmonic bands, because electron oscillations occur along two different axis: the transverse and the longitudinal (Figure 19a). The former band is the one more similar to the spherical nanoparticles band if the position on the spectrum is taken into account; this is also more independent from parameters like aspect ratio, assembly or dielectric characteristic of the surroundings than the latter band. For example,

a change in the aspect ratio from 1.7 to 5.2 leads to a blue-shift of the transverse band peak from 520 nm to 505 nm, and a red-shift of the longitudinal band peak from 590 nm to 935 nm[48]; the position of the resonances suggests that the transverse band is located in the visible, whereas the longitudinal band can be heavily tuned toward the near-infrared (NIR) region through the aspect ratio (Figure 19b).

A linear dependence between the nanorods aspect ratio AR and the plasmon resonance wavelength maximum λ_{max} has been defined by K. Jain et al.[31] so that:

$$\lambda_{max} = (445.4 + 90.6 \cdot AR) \tag{15}$$

clearly showing the longitudinal plasmon band redshift occurring for higher aspect ratios. Photovoltaic applications can rely upon this to trap light belonging to a different section of the solar energy distribution, which would normally be not possible to absorb and exploit.

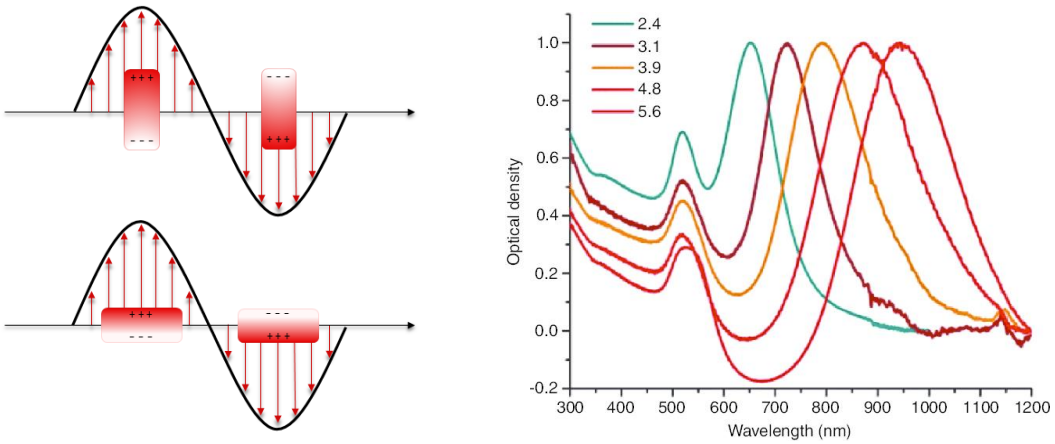

Figure 19 - Nanorods plasmonic oscillations and effect of the aspect ratio on the plasmonic wavelength. On the left, the schematic plasmonic oscillation of nanorods in the two possible directions; on the right, the red-shift of the plasmonic resonance for increasing aspect ratios. From ref. (49)

Moreover, K. R. Catchpole and A. Polman[50] compared the fraction of light scattered into the same substrate for Au particles of different shapes. As stated previously in this work, scattering is one of the way through which nanoparticles can supply more energy in a solar cell, thus it would be ideal to scatter as mush light as possible into the active layer. They showed that in the range from 500 nm to 800 nm the fraction scattered in the substrate is much higher for cylinder and hemisphere than that for the spheres, and they

attribute this result to the fact that the average spacing to the substrate is smaller for these geometries than for spheres.

The unique optical and photothermal properties of gold nanorods can be used in a wide range of applications besides photovoltaics, such as: chemical and biological sensing, environmental and food analysis, imaging, clinical testing, photothermal therapy and others[51]. Exhaustive studies have been carried out about photothermal properties for the diagnosis and treatments of cancers with gold nanorods: in this case, the absorbed light is rapidly converted into heat, involving the photothermal heating of the nanoparticle and its surroundings; when the gold NP is attached to a diseased cell (for example a cancerous one), the heat can be used to selectively melt its membrane, destroying it[52].

Chapter 2

Objectives

The main goal of the thesis is to demonstrate the possibility to enhance the absorption of visible and infrared radiation by ZnO nanowires through the decoration with plasmonic gold nanorods and to characterize the optical properties of the composite systems.

The first objective was to successfully synthesize ZnO nanowires by a two-step hydrothermal process on FTO glass substrates. The nanostructures were characterized via X-ray diffraction (XRD) and scanning electron microscopy (SEM) to get information about their morphology and crystal structure: from XRD analysis it was possible to determine the ZnO nanowires crystal structure as well as the preferred growth direction; from SEM images it was possible to dimensionally characterize the nanowires and look how homogeneous was their distribution on the FTO substrate. Furthermore, the optical properties of ZnO nanowires were analysed through UV-Vis spectroscopy and photoluminescence, to detect the typical absorption and emission of light around the position of the excitonic peak (~ 380 nm).

The second objective was to decorate these semiconducting nanostructures with gold nanorods. Different deposition methods have been tested to maximize the homogeneous dispersion of gold nanorods on the ZnO surface, minimizing the agglomeration of the rods.

The third objective was to characterize the new ZnO/Au composite system, morphologically and optically. The main purpose was to examine possible differences in properties before and after gold addition, so that the same instruments and examination techniques were repeated after decoration. In particular, the first aim was to detect plasmonic behaviour of the composite structure achieved by the interaction of ZnO with gold; new absorption peaks related to the plasmon resonance of gold nanorods were expected to come out from UV-Vis spectroscopy.

Chapter 3

Experimental Part

3.1 Nanocomposite development: FTO glass, ZnO and Au

The final material can be seen as a nanocomposite made up of three layers. The substrate is a fluorine-doped tin oxide (FTO) glass. Over its conductive face, ZnO nanowires are grown through a two-steps hydrothermal method. Afterwards, drops of gold nanorods in aqueous solution are poured on the FTO/NWs material in order to decorate ZnO with gold and achieve the absorption plasmonic properties. In a cross-section scheme, in the vertical direction, gold nanorods are expected on the top of the structure; some of them can penetrate through the nanowires and a few reach the base, depending on nanowires density and straightness (Figure 20). However, the aim is to put in contact the highest possible number of nanorods with the nanowires, avoiding losses of efficiencies due to the contact between nanorods, when they agglomerate. This might happen when high concentration of gold are added in the material.

In this paragraph, the full preparation of the single materials will be presented, as well as the decoration process.

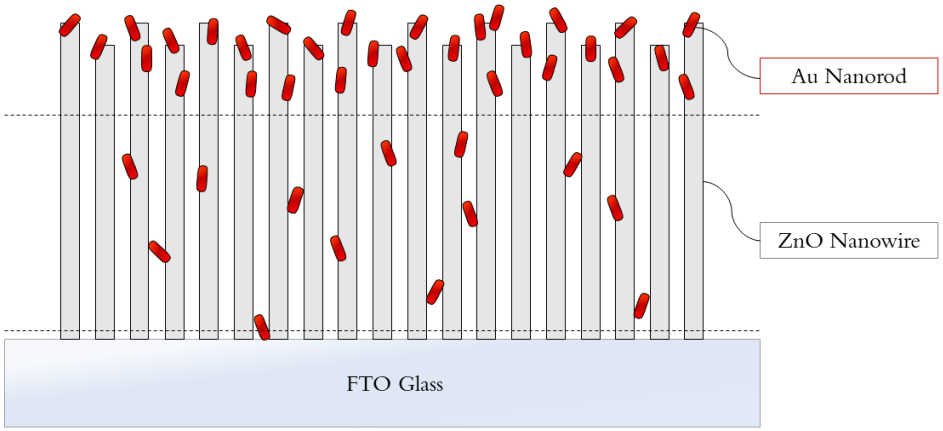

Figure 20 - Schematic structure of the nanocomposite system obtained. On the FTO substrate, ZnO nanowires are grown; later, Au nanorods are added on the top of the structure and they can be trapped by physical interaction with the nanowires after covering different distances from the top.

3.1.1 A transparent conductive substrate: FTO glass

Fluorine-doped tin oxide (FTO) glass comes under the TCO (transparent conducting oxide) materials, as well as indium tin oxide (ITO) glass. Both are widely used in photovoltaics because of their high conductivity and optical transparency. FTO is relatively stable under atmospheric conditions, chemically inert, mechanically hard, high-temperature resistant, abrasion resistant and, comparing to ITO, relatively cheap[53]. In particular, the high temperature resistance is suitable for the annealing process used to passivate surface defects on ZnO nanowires (300°C) and, even before, for the temperature requested to create the ZnO seed-layer on it (450°C). The ZnO growth process will be extensively explained in the following sub-paragraph.

To assure a correct growth of the nanowires, the FTO glass substrate is accurately treated. The glass samples used in this study have dimensions $2.5\ cm\ x\ 1.5\ cm\ x\ 2\ mm$. First, the FTO glass is accurately washed following these steps:

- First washing with a common dish soap;
- Second washing in acetone (C_3H_6O) followed by rinsing in water;
- Third washing in ethanol (C_2H_6O) followed by rinsing in water;
- Final rinsing in distilled water.

This procedure allows a good cleaning of the substrate from a wide variety of impurities, especially the ones coming from hand contact. Then, water is removed using a drier.
The procedure can be repeated until the glass surface appears completely transparent. Insufficient cleaning might cause problems in the synthesis of ZnO seed layer due to the presence of surface impurities that can lead to an inhomogeneous distribution of the zinc solution on the glass.

3.1.2 ZnO nanowire synthesis: hydrothermal process

There are many possibilities to synthesize ZnO nanostructures. The methods can be divided in two categories: solution phase synthesis and gas phase synthesis. The former deals with the evolution of the growth process in a liquid; when this is an aqueous solution, then it is referred to as hydrothermal growth process. Examples of solution phase synthesis are the ones implying zinc acetate hydrate, template assisted growth, spray pyrolysis and electrophoresis. Gas phase synthesis deals with the intermediation of a

closed chamber filled with a gaseous environment, and normally higher temperatures are reached (from 500°C to 1500°C). Examples of this method include vapour phase transport, physical and chemical vapour deposition, metal organic chemical vapour deposition and others[38].

ZnO nanowires can be successfully grown on glass and Si substrates by thermal decomposition of hexamine (also known as hexamethylenetetramine, HMT) and zinc nitrate. The process is a two-step growth where the first step consists in the formation of a thin film layer of ZnO seeds on the substrate using a spin-coating deposition. As stated by L.W. Ji et al.[54], the growth of ZnO nanowires strongly depends on seed layer: thinner seed layers with poor crystal characteristics make NWs to be poorly aligned, while thicker seed layers lead to vertical well-aligned NWs. Furthermore, increase of the seed layer thickness makes NWs diameters larger, but their density is lower. The second step is the growth of the nanowires. HMT, degrading at the synthesis temperature (which was 95°C), releases hydroxyl ions which react with zinc ions coming from the zinc nitrate to form ZnO. The process can be chemically described as follows:

$$(CH_2)_6N_4 + 6H_2O \leftrightarrow 6HCHO + 4NH_3 \quad (16)$$

$$NH_3 + H_2O \leftrightarrow NH_4^+ + OH^- \quad (17)$$

$$2OH^- + Zn^{2+} \rightarrow ZnO_{(s)} + H_2O \quad (18)$$

At the beginning, HMT decomposes into ammonia (equation 16) which in turn provides the hydroxide ions (equation 17); Zn^{2+} cations first react with NH_3 and OH^- to form ZnO nuclei, then react with more OH^- ions under a certain temperature to complete the growing step (equation 18)[55].

The function of the seed layer is to provide nucleation sites for the vertical growth of the nanowires. Other studies suggest that HMT has another important role in ZnO nanowires synthesis that is a shape-inducing molecule. The vertical growth can be guided not only by ZnO seeds, but also by hexamine, which is a long chain non-polar agent; from paragraph 1.6.1 it is known that the wurtzite structure is strongly polar along the c-axis, whereas the other facets are non-polar. HMT attaches to these before Zn^{2+} ions, which

are not able to build up the nanostructure in that directions; however, being the face (0001) polar, HMT doesn't attach to it and Zn^{2+} are free to make the nanostructure epitaxially growing in that direction: for this reason, the final structure is strongly oriented along the c-axis giving the possibility to obtain nanowires[56].

Seed layer solution

Component	Molecular weight	Quantity
$Zinc\ Acetate\ Dihydrate$ $(Zn(CH_3COO)_2 \cdot 2H_2O)$	$219.51\ \frac{g}{mol}$	$10.975\ mg$
$Ethanol\ (99\%)\ (C_2H_6O)$	$46.07\ \frac{g}{mol}$	$5\ mL$

Table 1 - Seed layer solution details for a typical synthesis in the laboratory.

Nanowire growth solution

Component	Molecular Weight	Quantity
$Zinc\ Nitrate\ (ZnNO_3)$	$297.49\ \frac{g}{mol}$	$1.785\ g$
Hexamine $(C_6H_{12}N_4)$	$140.19\ \frac{g}{mol}$	$0.84\ g$
$Distilled\ water\ (H_20)$	$18.02\ \frac{g}{mol}$	$120\ mL$

Table 2 - Nanowires growth typical preparation. Distilled water is divided in two parts of 60 mL where the two solid components are independently dissolved. Afterwards, they are also mixed together and stirred for only a few minutes.

The method followed in this project is a hydrothermal growth process mediated by zinc acetate dihydrate in ethanol, and it will be described in detail. Zinc acetate dihydrate $(Zn(CH_3COO)_2 \cdot 2H_2O)$ must be dissolved in ethanol 99% (C_2H_6O) to form a solution $1 \times 10^{-2}M$ (Table 1). An ultrasonic stirrer was employed to help the dissolution process. 100 μL of this alcoholic solution is then spin-coated on the cleaned FTO substrate at 3000 rpm. Actually, the spin coater rotates slower the first five seconds to adjust the position of the glass inside the instrument; after that, the full speed is reached and maintained for 55 seconds. The glass is afterwards warmed up on a heater plate at 120°C for 10 minutes, to make the alcohol part evaporating. Then, the entire process starts again: a second spin coating deposition is carried out followed by heating. This cycle is repeated 4 times,

pouring 100 μL of solution each time, guaranteeing a homogeneous and thick enough distribution of the solution on the FTO surface. Then, the sample is inserted in an ambient atmosphere furnace at 450°C for two hours and let it cool down slowly inside the furnace: this process leads to the formation of the ZnO seed layer on the FTO surface. The following step leads to the nanowire growth. Two aqueous solutions are prepared: one with zinc nitrate ($ZnNO_3$) and the other one with hexamethylenetetramine (HMT, $C_6H_{12}N_4$), both with concentration $1 \times 10^{-1}M$. The two solutions are stirred separately until no solid residual can be seen in the liquids; after that, they are mixed together for a few minutes. The FTO/seed layer sample is soaked in a Teflon autoclave filled with this mixed solution, and the autoclave is then closed and put in an oven at 95°C for 3 hours. After this time, the autoclave is taken from the oven, opened, and the samples are washed in distilled water to remove overgrowth superficial nanowires and surface impurities. Visually, the sample should have turned from transparent to opaque white, exhibiting the growth of ZnO nanostructures.

Figure 21 graphically describes the process from solutions preparation to the final inspection of the sample. We are giving here some more details to make the whole process perfectly reproducible.

In point 1, zinc acetate dihydrate was dissolved in ethanol (99%); the quality of the ethanol is important. In fact, also ethanol (95%) was tried to dissolve the zinc precursor, but in this case, the final solution sometimes presented inhomogeneity problems, where the zinc acetate formed a separated white cloud at the bottom of the beaker. It seems that ethanol (95%) was not able to successfully and entirely dissolve the solid precursor.

In point 3, a precise heating path was programmed in the furnace. Starting from room temperature, a heating rate of $7.5\frac{^\circ C}{min}$ is imposed to reach the treatment temperature of 450°C; the sample is left at this temperature for two hours. Afterwards, the sample cools down in the furnace on its own, so that it is kept in the furnace overnight. The aim was not to reach the treatment temperature too fast, and not to cool down the sample too quickly, to avoid thermal stresses in the sample. All the samples belonging to the same batch are located together in the middle of the furnace, simultaneously.

In point 4 one clarification is needed. First, the mixing of the two solution must not last more than 2-3 minutes, because the reaction could already start before the insertion

of the autoclave in the oven. For this reason, the sample is set into the autoclave and the mixed solution is quickly added into the autoclave after a few minutes of stirring.

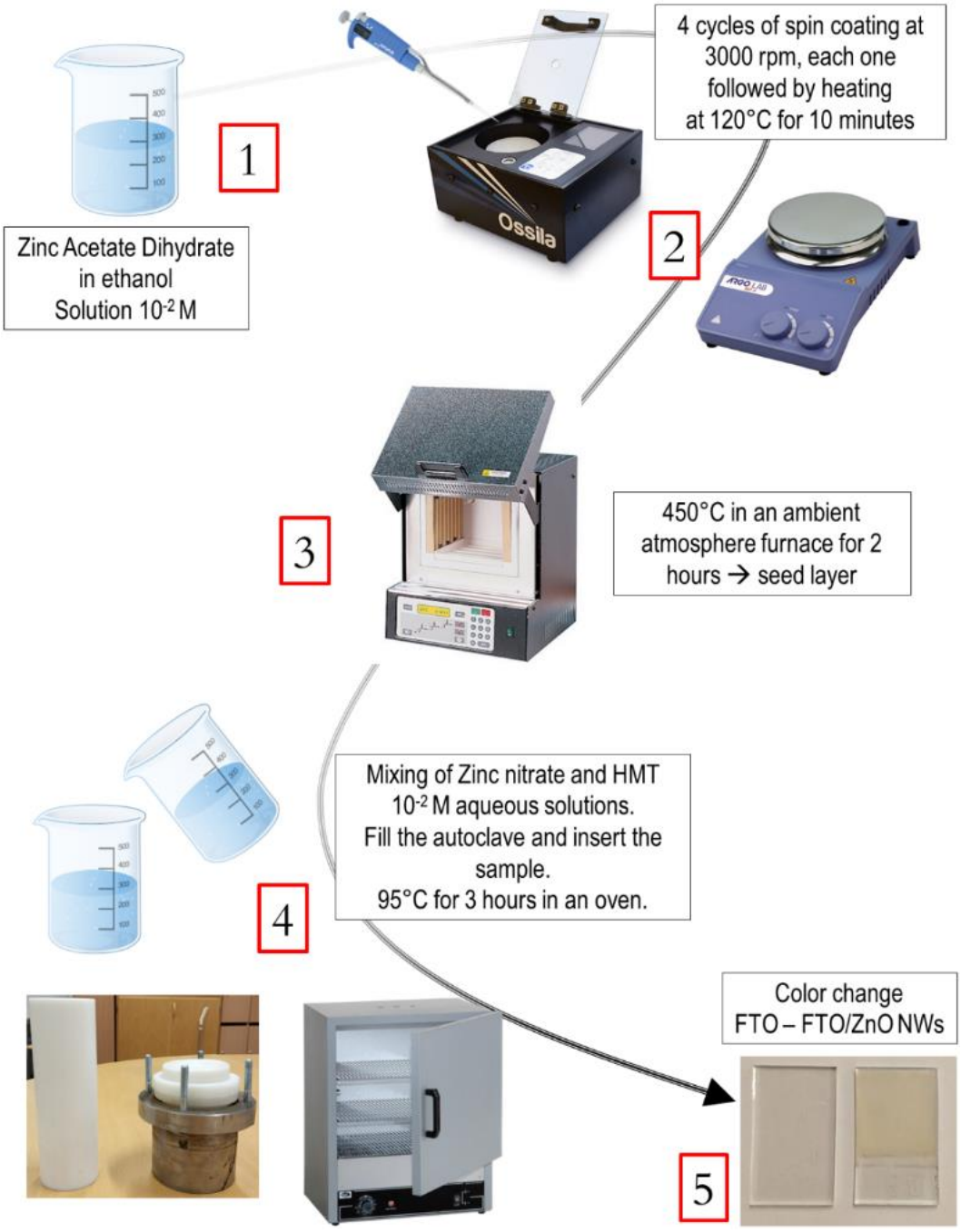

Figure 21 - Scheme of the two-step hydrothermal growth process to get ZnO nanowires. Steps 1-3 concern the synthesis of the seed layer; steps 4-5 represent the growth of ZnO nanowires. All the samples presented in this research were obtained following this procedure.

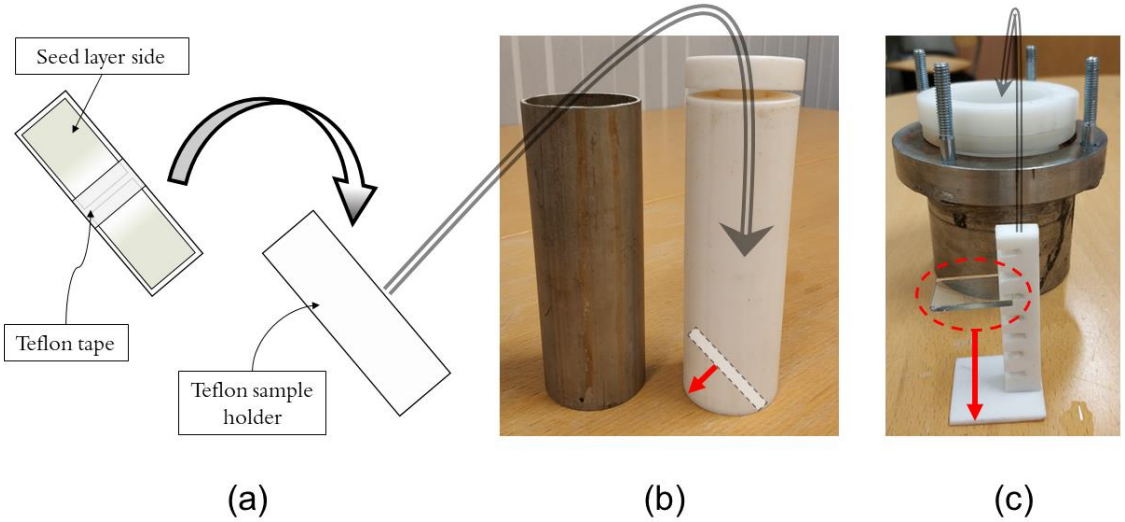

Figure 22 - Sample preparation in two different autoclaves. Two samples are adjusted on a sample holder by Teflon tape and the seed layer side is flipped upside-down (a); then everything is put inside the first autoclave, and the sample leans against the wall with a certain inclination (b). In the second type autoclave the samples are fixed in the sample holder with the seed layer side looking down, too; no tilting is needed (c). The red arrows explicit the nanowires growth direction.

In point 5, a comparison by eye is provided between an FTO glass and an FTO with ZnO nanowires grown on it. In the latter, when the deposition occurred correctly, the colour appears homogeneous on the whole surface. Transparent parts can be due to the absence of seed layer and the corresponding absence of NWs; bright white parts or points are generally related to overgrown NWs, namely nanowires that are evidently bigger in dimensions than the average of the population and result in stronger light scattering.

3.1.3 Gold nanorods synthesis: the seed-mediated method

A nanorod (NR) is a nanoparticle characterized by an aspect ratio (ratio between its length and width) generally included between 1 and 6, nearly adjustable in 0.5 increments, when silver ions are added during the growth; higher aspect ratio rods can be synthesized performing three-step seeding methods adjusting the time of reaction of each step[57]. As already stated in paragraph 1.6.2, this is really an important feature because the plasmonic properties can efficiently and easily be tuned according to the aspect ratio: more precisely, an increase of the aspect ratio causes a red-shift of the longitudinal plasmonic band, that makes the absorption of a wider part in the NIR possible. All the mechanisms of LSPR light absorption enhancement presented in Figure 15 are possible in gold nanorods:

actually, compared to spherical particles, the near electric field enhancement is even higher because of the tip-end shape.

The gold nanorods synthesis took place in the NanoEng laboratories of "Università degli studi di Padova", by professor Alessandro Martucci and Dr. Gregorio Carolo, using a so called silver-assisted seed-mediated method[58]. With this wet-chemistry approach, single crystal NRs can be grown. The first step is to obtain isotropic particles, which will be afterwards modified to get NRs, which are anisotropic particles, instead. In an aqueous solution of Cetyl trimethylammonium bromide (CTAB, $C_{19}H_{42}BrN$), supersaturated Au (III) ions are reduced to Au (0) ions by a strong reductant in excess, that is sodium borohydride ($NaBH_4$). Then, the particles obtained, similar to little seeds, are injected into a growth solution of the same CTAB, in presence of Ag^+ ions and Au (I) ions, where the latter are provided by a previous reduction made by ascorbic acid ($C_6H_8O_6$), a moderate reductant agent. Each chemical species has a fundamental role in the growth of the NRs.

The surfactant, CTAB, was proved to favour the one-dimensional growth of nanorods by capping action in the form of complex $CTA^+ - Br^- - Ag^+$. NRs are actually produced surrounded by a CTAB bilayer, where quaternary ammonium head groups lead to hydrophilic interactions, while surfactant tails interact hydrophobically in the bilayer core.

A gold precursor is necessary to give the Au (III) ions, that is, in most of the cases, tetrachloroauric acid ($HAuCl_4$). These ions produce metallic gold nuclei after the fast injection of the $NaBH_4$ solution.

The ascorbic acid promotes the reduction of Au (III) to Au (I) ions, which are added to a solution of CTAB waiting for the seeds to be inserted. This agent is chosen because it is too weak to reduce gold ions from Au (III) to Au (0) alone, so the growth step occurs on a longer period of time, which aids in anisotropic growth. Moreover, the seeds act as catalysts for the reduction on their surfaces from Au (I) to Au (0), that provides the kind of gold eventually present in the nanorods.

The role of the silver ions is still under debate, but it was strongly established that the NRs aspect ratio depends on the silver nitrate concentration in the synthesis. Three mechanisms are considered to be responsible of the silver interaction with the nanorods, and they are believed to happen also in the same pot to some extent: the action of a

$CTA^+ - Br^- - Ag^+$complex as face-specific capping agent, which preferentially blocks the growth at longitudinal crystal faces; the synergy of Ag and Br in altering the shape of CTAB micelles from spherical to cylindrical, imparting the latter shape as soft template agents; the deposition of a sub-monolayer quantity of metallic Ag on the longitudinal facets of Au NRs[59].

A final aspect to remark is that the surfactant CTAB can be found both on NRs surfaces and free after growth completion and even after purification. Centrifugation is needed at least once after synthesis, while several more controls are fundamental if NRs are planned to be used in biological applications. In fact, CTAB-coated Au NRs exhibit cytotoxicity to most cells due to the CTAB surfactant: further surface modification methods such as ligand and exchange, layer-by-layer and surface coating can be performed to grant good stability and reduced cytotoxicity[60].

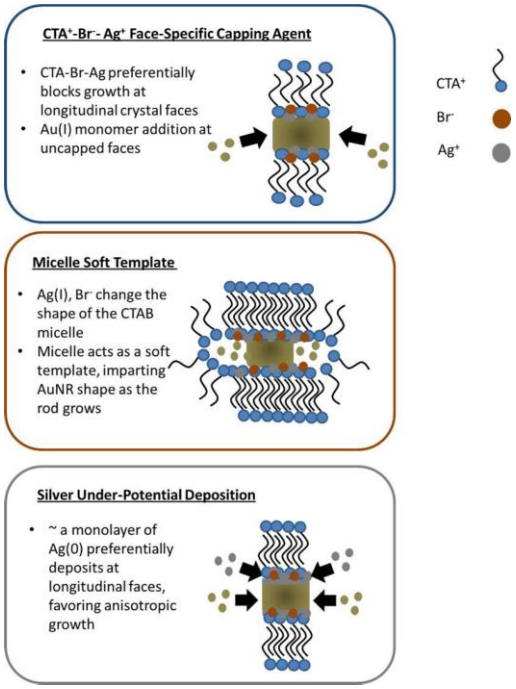

Figure 23 - Schematic representation of the mechanisms proposed to explain silver role in Au NRs growth. In any case, a strong shape-induced control is achieved. From ref. [59].

3.2 Gold deposition and further treatments

A crucial step to complete the nanocomposite material is the decoration of the ZnO NWs with the Au NRs. The purpose is to put the two materials in direct contact, trying to avoid agglomerated blocks of nanorods and in the easiest possible way. In literature, several decoration methods are presented: H.T. Chou et al.[61] immersed ZnO NRs/ITO modified with APTES solution in a solution of Au NPs for 8 hours, cleaned by distilled water and then placed in oven at 100°C for 10 minutes; J. Kim and K. Yong[62] used a ultrasonic cleaner to deposit the gold nanoparticles on ZnO nanostructures; V. Perumal et al.[63] sputtered Au NPs using an electric current of 25 mA for 2-8 min with vacuum pressure of argon process level at 10^{-2} mbar; these examples and many other depositions lead to a successful hybrid nano-heterostructure glass/ZnO/Au.

In this project, a very simple yet quite effective approach was chosen. The aqueous gold solution, $0.8\,mM\ (Au), Br^-$ stabilized, was dropped on the FTO/ZnO NWs sample using a micropipette (Figure 24). The spilled quantity was varied in different samples, in the range $5 \div 50\ \mu L$ for each drop, being 10 and 20 μL the two mostly used quantities. The number of the drops added was varied in different samples, too, to obtain different gold concentrations and to study the influence of gold concentration on the optical properties.

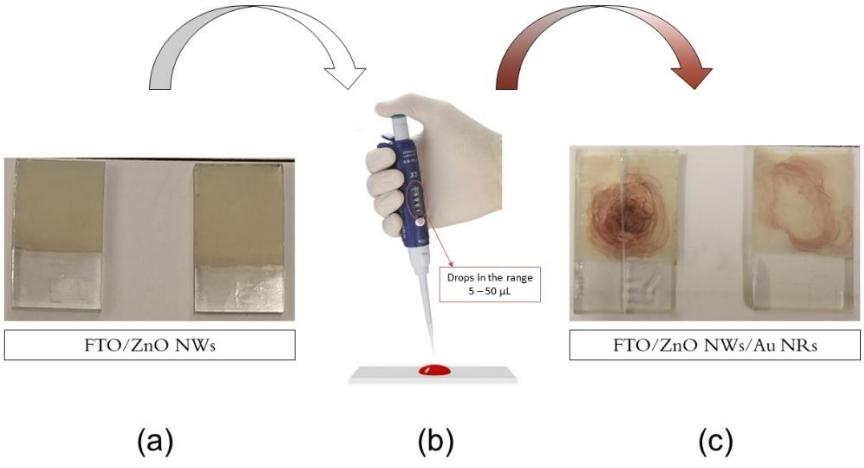

Figure 24 - Gold deposition on ZnO nanowires. FTO/ZnO NWs samples (a) lay horizontally; with a micropipette, gold solution is spilled in drops of $5 \div 50\ \mu L$ *(b). The quantity of gold may vary for each sample. When high quantity of solution are spilled, the sample acquires a dark colour (c, left); when less gold is spilled, the sample shows a lighter red colour (c, right).*

In Figure 24c, it may be noticed that the gold distribution (detected by red shades) is quite inhomogeneous throughout the surface. This is due to the spreading of the liquid drop when the sample surface is touched. Bigger drops ($\geq 20\ \mu L$) show the highest spreading, so that gold nanorods are pushed towards the glass edges; smaller drops ($\leq 10\ \mu L$) are more controllable and create a circular area around the centre. When more than one drop is spilled on a sample, weak warm air was blown from a dryer to accelerate the drying of the drop before spilling the following one. It was observed that in this way, it was easier to achieve a better control of gold spreading, consequently solution drops were more efficiently confined near the centre.

The concentration gradient assured the possibility of comparing different gold concentrations on the same substrate (Figure 25); this was fundamental to prove, in photoluminescence results, the direct correlation of the quenching of the NBE peak with gold concentration, rather than to random un-homogeneities coming from un-homogeneous nanowires.

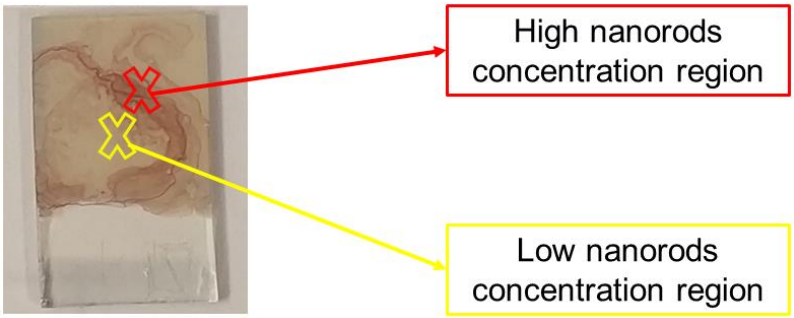

Figure 25 - Gold nanorods concentration gradient within one sample. In absorption and photoluminescence measurements it is critical to define the analysis spot, since it can strongly affect the results.

We applied supplementary treatments to the system. These processes can be applied on ZnO NWs (annealing or plasma treatments after NW synthesis) or after the nanocomposite attainment (annealing or vacuum treatment of the whole FTO/ZnO/Au system).

In particular, annealing treatments were extensively applied before gold deposition. Annealing was always performed in the same conditions, which are: heating at 300°C for one hour in an ambient atmosphere furnace. The main effect of this treatment is revealed by photoluminescence measurements of ZnO nanowires: defects emission is expected to decrease in favour of NBE enhancement. This phenomenon can be explained by hydrogen

donor formation activated by thermal annealing: as a matter of fact, generation of interstitial H is common during ZnO growth. If H does not complete its dehydration process, then hydrogen defects can arise. So initial H, interstitial H and even H complex (OH or complex with other defects) may all be present. Annealing temperatures, however, activate defects passivation which in turns makes trapped H release; interstitial H can move efficiently towards oxygen vacancies forming H_O; hydroxyl groups follow a desorption process. It is believed that the enhancement of the NBE peak comes from the formation of hydrogen donor, while the reduction of defects emission is attributed to the annihilation of hydroxyl groups[64].

Plasma treatments suppressed defects emission, too. Cold plasma of hydrogen and oxygen were applied by dr. Alessandro Patelli in Università degli Studi di Padova.

3.3 Morphological, structural and optical characterization

After NW growth, the samples first undergo a visual inspection, to check if the expected opaque white layer is formed atop the FTO. When (part of) the process is not carried out properly, it can result in in-homogenous growth. As an instance, in Figure 26 two nominally identical batches are compared: both of them followed the same procedure (Figure 21), but the they look very different. The samples on the left present a homogeneous whitish coat, while the samples on the right show discontinuities (lower density or thinner NWs) and brighter points (overgrown NWs) on the layer. The visual inspection is important to identify rough issues during NW growth and to exclude those samples from the systematic analysis.

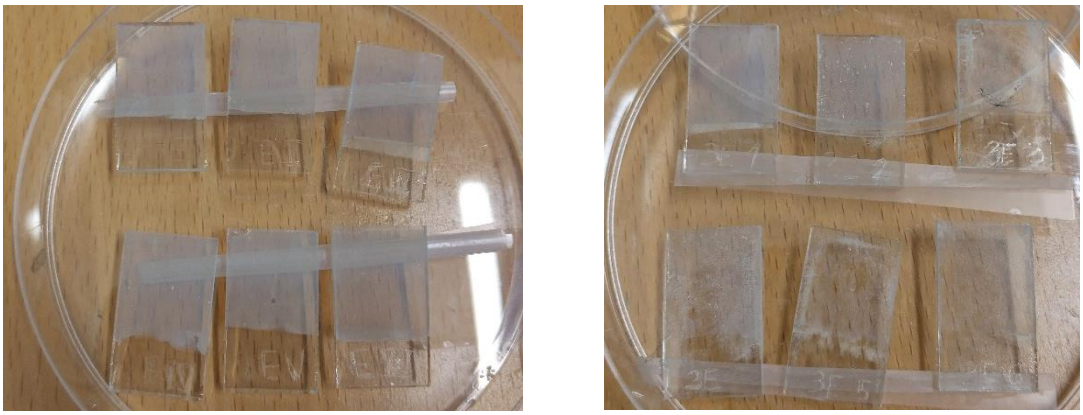

Figure 26 - Batches look comparison. The samples on the left present a homogeneous whiteish surface coming from the presence of ZnO nanowires. The samples on the right, instead, show imperfections such as transparent voids and brighter points due to lack or overgrowth of nanowires, respectively.

Further characterization includes morphological and optical analyses. The morphology of the NWs was examined through SEM and TEM; EDS was applied to get a quantitative composition of the samples and XRD analysis was applied to investigate their crystalline structure. The optical tests include mainly UV-Vis spectroscopy and photoluminescence spectroscopy. The former is particularly important to gather transmission and reflection spectra of ZnO nanowires before and after gold decoration, fundamental to identify the expected absorption increase due to nanorods. Photoluminescence measurements were carried out to remark the effect of gold nanorods, too, considering that they can be related to energy transfer processes.

In the following paragraphs, all the characterization techniques will be described, not to explain the operating principles of each instrument, but rather to point out why each technique was applied and how the results are relevant to the final considerations about the effective possibility of decorating ZnO with gold to enhance photon absorption.

3.3.1 Structural and morphological characterization: XRD and electron microscopies

XRD was performed on a PANalytical X'Pert instrument operated in reflection mode. From the literature, a preferential growth in one direction is expected. In addition, XRD was repeated after gold decoration to point out the presence of gold nanostructures.

Transmission electron microscopy (TEM) was used to characterize the gold nanorods. HR-TEM and STEM micrographs were taken on a FEI Tecnai F20 transmission electron microscope equipped with a Schottky emitter operating at 200 kV. They were all performed in the CNR-IMM department of Bologna, Italy, by Dr. Raffaello Mazzaro. Nanorods are drop-casted onto an amorphous carbon coated copper TEM grid. Afterwards, it was possible to measure length and width of several nanorods directly from TEM images. Calculations of their size distribution and their average dimensions were performed. This is important because from eq. 15 a clear relationship between aspect ratio and longitudinal plasmonic peak exists, which can be demonstrated through the analysis of absorption spectra.

Scanning electron microscopy (SEM) was used to characterize both pristine ZnO nanowires and Au-decorated NWs. SEM micrographs were collected with a FEI Magellan 400 FEG-SEM operated at 3kV, equipped with monochromator, through-lens

detector (in-lens), and X-Max 80 Silicon Drift Detector for EDS mapping (Oxford Instruments). Similar to what done on gold nanorods, length and width of several nanowires were measured to get mean values and to underline potential differences among batches. It was possible to look for the typical hexagonal tip of wurtzite structure, too. After gold decoration, SEM pictures were analysed to see how nanorods distribute on nanowires, if they agglomerate and if they reached the substrate passing through the NWs forest. Cross-section analysis was performed, too, in order to get a complete picture on the whole thickness of the sample.

3.3.2 Optical characterization: UV-Vis and photoluminescence spectroscopies

The most interesting part of the results deals with optical properties. ZnO absorbs light in the UV region, while gold rods absorb both in the visible and in the NIR. Absorbance and transmittance spectra were collected to analyse the influence of gold nanorods on ZnO NWs optical properties, looking for plasmonic bands. The instrument used was a Cary 5000 spectrophotometer from Agilent technologies; an integrating spectralon sphere with reflectance $> 95\%$ in the $300 \div 1000\ nm$ range was applied to get the diffuse reflectance, which takes into account the scattered light, too. The sample coatings could be very inhomogeneous, so it is important to clarify from which spots the measurements are taken: generally, the measurement was located in the centre of the samples; sometimes, to study the effect of different concentration of gold (detected by darker colour), the measurement was taken from different points, and the exact position was recorded through visual inspection.

Photoluminescence spectroscopy was carried out to observe the excitonic recombination emission (Near Band Emission, NBE) typical of ZnO in the UV region and the defects emission (Deep Level Emission, DLE) in the visible range; after addition of gold, the measurements were repeated to analyse potential differences. Photoluminescence excitation (PLE) and emission (PL) spectra in the visible and NIR range were recorded by an Edinburgh Instruments FLS980 Photoluminescence Spectrometer. A continuous-wave xenon lamp was used as excitation source for steady-state measurements, coupled to a double-grating monochromator for wavelength selection. The light emitted from the sample was collected by a double-grating

monochromator and recorded by a photon counting R928P PMT cooled at -20 °C (visible range) or by a R5509-73 PMT cooled at -80 °C (NIR range).

Two kinds of measurements took place. The first is a single emission scan, where the sample is excited by a lamp with wavelength $\lambda_{exc} = 325\ nm$ and the emission is collected by the detector in the range $350 \div 750\ nm$ (Figure 27a). This can be further compared to the measurement taken after annealing process or after decoration with gold. It will be shown that in both cases there will be a change in the single emission by the material. The second kind of measurement is a multiple emission scan and deals with the collection of multiple scans on the same sample, exactly on the same spot, at the same excitation $\lambda_{exc} = 325\ nm$, but where one scan starts exactly after the previous ends, for a certain number of times (Figure 27b). In this project, actually 21 scans were performed at the same conditions, to observe the variation of the emission peaks coming from the Au-decorated ZnO NWs, when continuously excited. To cover the entire range, each scan lasts around 80 seconds, so that the 21st emission scan is collected almost half an hour after the first one under continuous UV excitation.

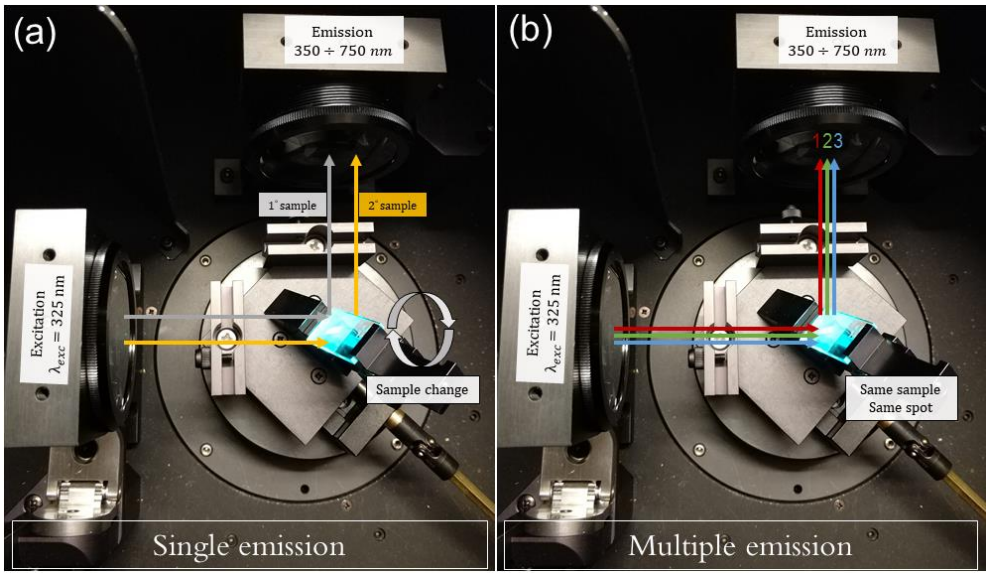

Figure 27 - Photoluminescence measurement settings. In the single emission method, one sample is excited to acquire its emission spectrum; this can be used to be further compared to the response after annealing or addition with gold on the same sample, or with different samples (a). In the multiple emission method, the same sample is excited on the same spot continuously, meaning that a certain number of emission spectra are collected one after the other (b).

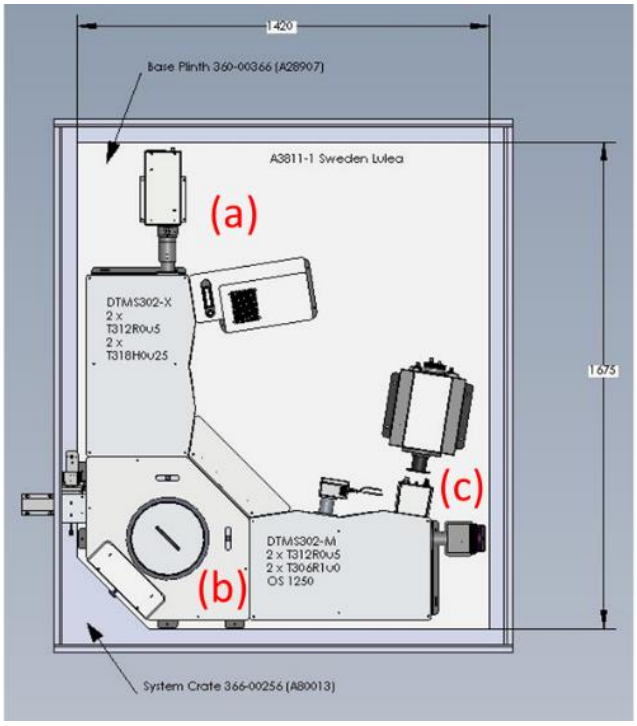

Figure 28 - Photoluminescence spectrometer scheme used in Luleå University of technology. The excitation ray source (a) is a xenon lamp; the radiation hits the sample in the chamber (b), where the excited sample emits another radiation that is in turn collected by the selected detector (c).

3.4 List of the samples

We give here full description and proper labelling of the samples considered in this study.

42 samples were synthesized in total. ZnO nanowires were synthesized and grown in groups of six, in the same day, using the same solutions; this group of samples is referred to as "batch", so that in total seven batches were studied. Actually, batches number 4 and 5 were discarded due to wrong furnace temperature setting and low nanowires quality, respectively (Table 3). We tried to minimize the differences arising from different preparation conditions during NW synthesis. The synthesis method of ZnO nanowires was always performed in the same way; however, results may vary according to slight variations in the solutions preparation, mildly longer or shorter timing passed in the ovens (whereas every batch was insert in the ovens simultaneously), random and uncontrollable impurities that survived FTO cleaning and so on. Gold deposition was carried on in the same way, too; in this case, only some samples were covered by gold and with different concentrations, according to Table 4. However, shape, dimensions, alignment of the nanowires may have an influence on the distribution of the nanorods.

BATCH	SAMPLES
1	1EI, 1EII, 1EIII, 1EIV, 1EV, 1EVI
2	2E1, 2E2, 2E3, 2E4, 2E5, 2E6
3	3E1, 3E2, 3E3, 3E4, 3E5, 3E6
4	DISCARDED
5	DISCARDED
6	6E1, 6E2, 6E3, 6E4, 6E5, 6E6
7	7E1, 7E2, 7E3, 7E4, 7E5, 7E6

Table 3 - Batches and sample labels used in this research.

Table 4 presents all the samples in detail. Columns "batches" and "samples" express the designation method already shown in Table 3. "Autoclave" column can be filled with 1 or 2, depending on which kind of autoclave was used to synthesized the corresponding sample (autoclave 1 is in Figure 22b, autoclave 2 in Figure 22c); as already stated before, every batch was synthesized in the same conditions, so only the entire batch 7 was

synthesized with a different autoclave. “Annealed” column can be filled only with “Y” if the sample underwent an annealing process (at 300°C for one hour in air); if the sample is also covered with gold, the annealing is intended to be done before the decoration. Finally, “gold” column express the total amount (expressed in µL) of gold solution spilled on the sample; in brackets, the details of deposition concerning the number of drops multiplied for the amount of each drop. This was understood to be important when it was seen that bigger drops spread more towards the edges of the glass, whereas it was

Batch	Sample	Autoclave	Annealed (300°, 1hr)	Gold (drops x amount (uL))
1	1E1	1		50uL (1x20 + 3x10)
	1E2	1		
	1E3	1		
	1E4	1		80ul (4x20)
	1E5	1		
	1E6	1		
2	2E1	1		100µL (2x50)
	2E2	1	Y	
	2E3	1		100µL
	2E4	1	Y	200µL (drops of 5 and 10 uL)
	2E5	1	Y	
	2E6	1	Y	
3	3E1	1	Y	
	3E2	1	Y	100µL
	3E3	1	Y	80µL (4x20)
	3E4	1	Y	
	3E5	1	Y	
	3E6	1	Y	
6	6E1	1		50uL (5x10) + 50uL in vacuum
	6E2	1		100uL (10x10)
	6E3	1		
	6E4	1	Y	50uL (5x10)
	6E5	1	Y	100uL (10x10)
	6E6	1	Y	
7	7E1	2		
	7E2	2		80µL (4x20)
	7E3	2		160µL (16x10)
	7E4	2		
	7E5	2		Sputtering - 4nm layer
	7E6	2		

Table 4 – Synthesized samples details. For the explanation of each column, please refer to paragraph 3.4.

preferable to keep the largest part of gold near the centre to make the characterization measurements easier and more reproducible. In this column, sample 6E1 presents some amount of gold "in vacuum": this refers to a process made to try to reduce potential impurities to the minimum, for example by promoting the evaporation of some species. Also, it was thought that using vacuum just after the gold deposition, drying the water quickly would have allowed nanorods to spread less. Sample 7E5 is marked with the word "sputtering": this different deposition technique was tried on only one sample because it was not possible to deposit gold nanorods, whereas spherical gold particles were sputtered until a layer of 4 nm was obtained. Both vacuum treatment and sputtering deposition were not further investigated and analysed for lack of time, but they represent interesting approaches for future work possibilities.

The deposition occurred always in the same way, following the scheme of Figure 24; the gold solution often spreads gold nanorods towards the edges, pushed by the water contained in the solution; generally, small drops managed to stay around the centre because of the lower amount of water involved. Uneven deposition of gold nanorods on ZnO NWs gave the possibility to study how the concentration of gold affected the optical properties of the samples. The darker colour arising on some samples derived from higher concentrations of nanorods, as proved by SEM images, and this was related to enhanced absorption shown by UV-Vis spectra and different effects on photoluminescence, as discussed in the following chapter.

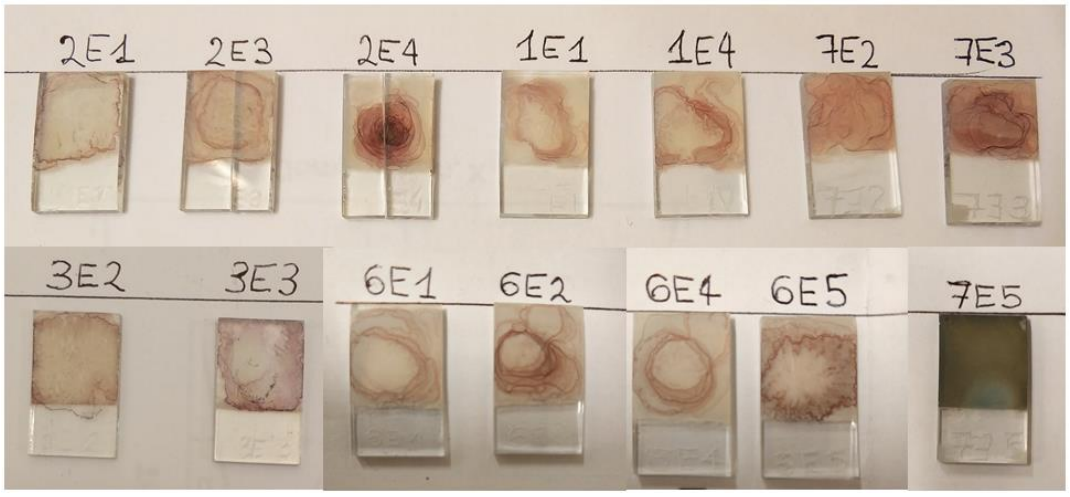

Figure 29 - Picture of the samples decorated with gold used in the laboratory and their names. Inhomogeneities come from different drops spreading and nanowires shape and alignment. See Table 4 for further samples details.

Chapter 4

Results and discussion

We are reporting here the results obtained on sample production and characterization, targeting the following objectives:

- Reproducible synthesis of ZnO nanowires through a two-step hydrothermal process on an FTO substrate;
- Deposition of gold nanorods on the FTO/ZnO system, achieving a good contact between Au and ZnO limiting as much as possible agglomeration;
- Characterization of the optical properties of the new FTO/ZnO/Au nanocomposite in terms of light absorption and charge/energy transfer between plasmonic structures and ZnO.

Morphological and structural characterization has been done to verify the first two points, while optical characterization is necessary for the third one. The results will be presented following a characterization order, beginning with the morphology (SEM and TEM), structure (XRD, TEM) and continuing with the optical properties (UV-vis and photoluminescence). Important differences arising after Au deposition will be stressed comparing the results before and after deposition.

4.1 Morphological and structural characterization

Au nanorods alone were characterized through TEM before and after their deposition on ZnO nanowires. The analysis before the synthesis enabled the accurate knowledge of their shape, size and structure. XRD analysis was applied to ZnO nanowires before and after gold decoration to analyse their crystalline structure (which is expected to be wurtzite, according to the literature) and to check the presence of the crystalline structure of gold after decoration. SEM analysis before and after gold decoration was applied to get insight into the morphology of the system and to highlight the effect of gold rods

concentration. EDS analysis helps to understand which elements are present in the system before and after gold decoration.

4.1.1 Gold nanorods – TEM characterization

The synthetic procedure of the gold nanorods applied in this thesis was described in paragraph 3.1.3; the rod-like shape comes from an isotropy break activated after the formation of spherical nanoparticles; it is not rare to observe a bunch of the ancestor particles in the final nanorods batch (Figure 30). On the other hand, the results of the synthesis lead to a non mono-dispersed AR, with some distribution in the AR values.

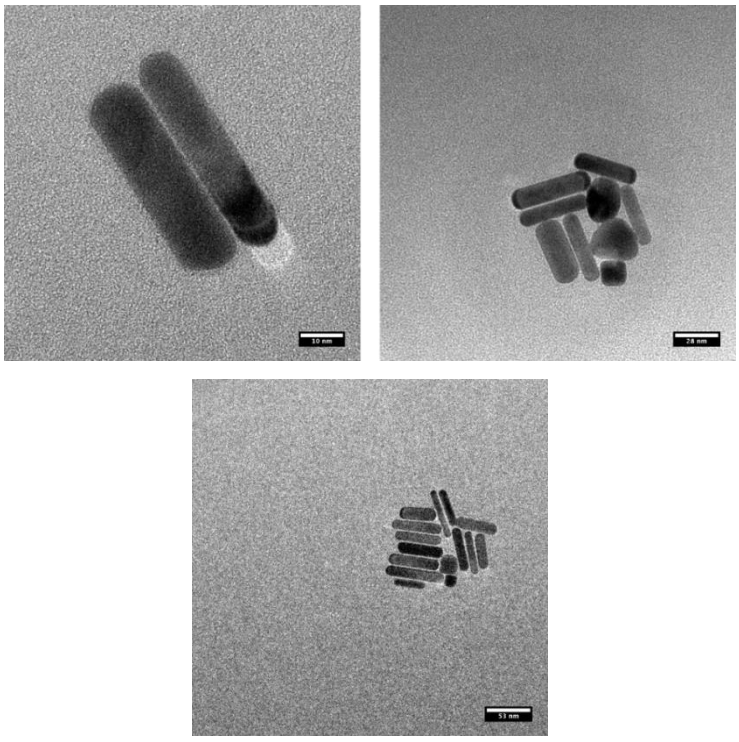

Figure 30 - TEM pictures of Au nanorods. Nanoparticles show mostly a rod-like shape; some spherical or other shapes nanoparticles are still present due to the synthesis process.

In Figure 30 TEM images of some gold NRs are reported. It is possible to measure the length, width and AR of several nanorods from the TEM pictures, in order to achieve a distribution curve of these dimensions. They equally contribute to the value of the aspect ratio, which in turn establishes the position of the plasmonic absorption peak in the near-infrared region. In Figure 31, the two distributions of the length and width are presented. Data come from the measurement of 27 nanorods.

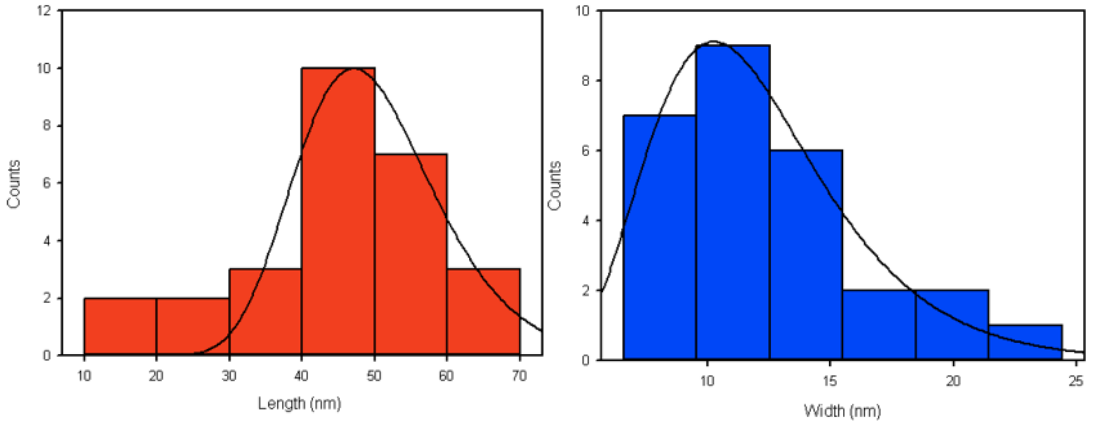

Average dimensions	
$Length = 47 \pm 11\ nm$	$Width = 10 \pm 4\ nm$

Figure 31 – Nanorods dimensions distributions coming from measurements on TEM pictures. The average length and width are reported below.

Using equation 15, with aspect ratio $AR = \frac{46.9}{10.2} = 4.6$, the longitudinal plasmon peak position should be $\lambda_{max} = 445.4 + 90.6 \cdot 4.6 = 862\ nm$. This will be verified later through transmittance spectra. However, a broad absorption region is expected to come out from the longitudinal plasmonic band, because it is strongly dependent on the aspect ratio, which in turn can vary quite a lot inside the batch, as it can be seen from Figure 31.

High-Resolution Electron Microscopy (HREM) micrographs confirm that the rods crystal structure is compatible with metallic gold one, as highlighted by Fast-Fourier Transform (FFT), performed on a single rod (Figure 32).

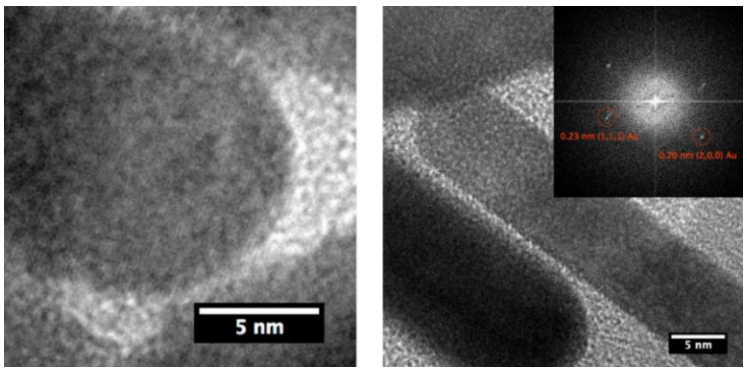

Figure 32 - HREM and FFT confirm the gold nature of the nanorods. Performed on a single rod.

4.1.2 ZnO nanowire structure and morphology: XRD and SEM

The XRD pattern obtained from ZnO nanowires on FTO is reported in Figure 33. The angular position of the peaks of the pattern is reported in Table 5. The characteristic peaks were compared with data existing in the literature about wurtzite structure for ZnO and cassiterite phase, typical of FTO film (Figure 33).

Pos (°2θ)	**Height (cts)**	**FWHM left (°2θ)**	**d-spacing (Å)**	**Rel. Intensity (%)**
26.8100	546.70	0.2558	3.3254	3.59
31.3092	56.96	0.3070	2.8570	0.37
32.0853	238.48	0.2047	2.7897	1.57
34.7390	15221.30	0.3070	2.5824	100.00
36.5694	322.39	0.3070	2.4573	2.12
38.0693	1790.92	0.2558	2.3638	11.77
47.8287	360.09	0.2047	1.9018	2.37
51.7673	373.97	0.2558	1.7660	2.46
57.0024	39.32	0.3070	1.6156	0.26
61.8708	176.13	0.3582	1.4997	1.16
63.0985	1253.49	0.2558	1.4734	8.24
65.7190	284.03	0.3582	1.4209	1.87
68.1637	54.49	0.2047	1.3758	0.36

Table 5 - XRD data of FTO/ZnO system. Peak position, its height, full width half maximum taken on the left, planes of atoms distance and relative intensity are listed for each peak recognized by the instrument. The highest intensity peak is the one corresponding to the epitaxial preferred growth direction.

As it can be seen from Figure 33, all the peaks correspond either to wurtzite hexagonal phase (Ref. code 96-900-4180) of ZnO or cassiterite (Ref. code 96-900-7434) of FTO (black and red lines in the bottom, respectively), so the results are perfectly consistent. Moreover, the relative intensity of the (002) crystallographic plane measured from the sample is much higher compared to all other reflections in the benchmarking pattern. This confirms the fact that nanowires grow in a single crystalline arrangement and follow a preferred orientation, which is the c-axis of the hexagonal wurtzite structure, and perpendicular to the FTO substrate, as later suggested by SEM analysis. All the other peaks come from different lattice planes of ZnO or from FTO cassiterite phase.

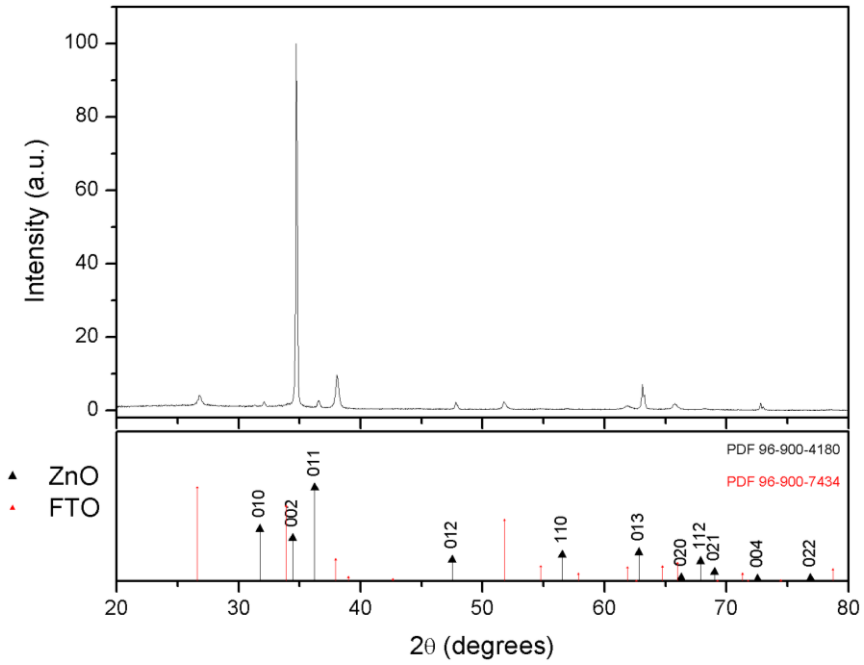

Figure 33 - XRD peaks are showed above, while the corresponding patterns of hexagonal wurtzite and cassiterite are expressed by black and red lines, respectively, at the bottom. Reference patterns come from ref. code 96-900-4180 for wurtzite and ref. code 96-900-7434 for cassiterite. The highest intensity of the (002) peak expresses the nanowires preferred growth orientation along the c-axis.

We collected SEM images both in planar and cross sectional view. The former displays the hexagonal shape of nanowires, the latter allows to see how straight the nanowires are and if there are some imperfections along the whole thickness of the sample.

In Figure 34, three planar SEM pictures are presented. The general distribution of nanowires can be seen from a low magnification view (Figure 34a), while more details can be noticed when the magnification is higher (Figure 34b), like, for instance, the hexagonal cross section, typical of the wurtzite structure for ZnO grown along the c-axis. From the lower magnification image, it may be observed that nanowires are characterized by different diameters; for this purpose, a bunch of nanowires can be measured to draw the dimensions distribution curve to get the average diameter. It is also possible to do the same with the height, but in this case cross-section images are necessary since in planar view images nanowires are hidden by others and they do not fully compare in the image. Figure 35 reports diameter measurements for three samples, each one belonging to a different batch. In the experimental part, every batch counts 6 samples; every batch is prepared exactly in the same way, adopting the procedure of Figure 21, but in different days and preparing the new solution every time.

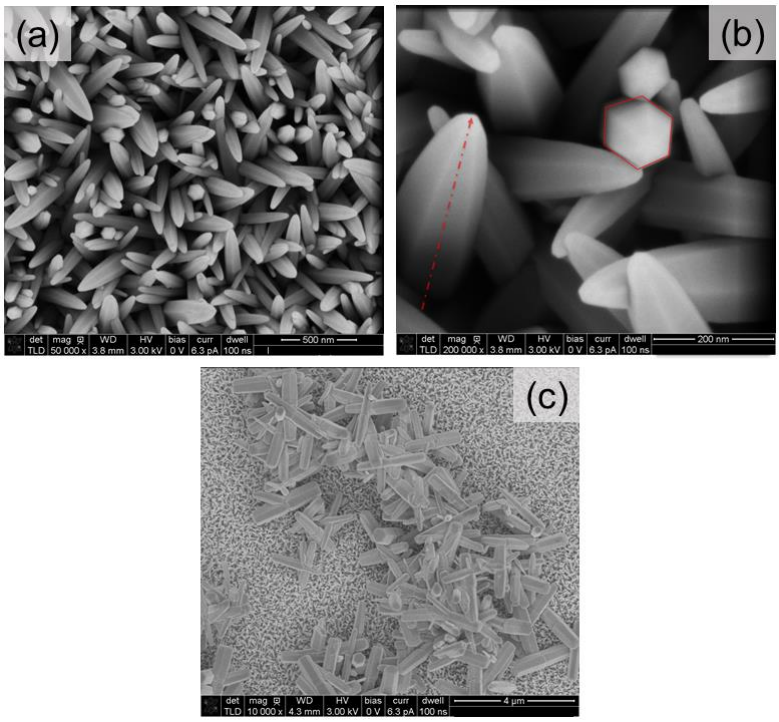

Figure 34 - SEM pictures of ZnO nanowires. Low-magnification (50.000x) allows to observe a wider range of nanowires (a); higher magnification (200.000x) allows to detect the hexagonal shape of wurtzite (red hexagon), while the red arrow highlights the preferential growth direction (b). Isolated regions in some samples can host overgrown nanowires (c), macroscopically visible like brighter white dots on the surface.

The procedure consists of many steps, and especially differences in the growth time or in the quantity of precursor may lead to different results. As written by Han Zhitao et al.[65], when increasing the growth duration the diameter and length of ZnO NWs increase, until both the dimensions start to reduce sharply. This is because at the beginning of the synthesis the zinc precursor can efficiently provide Zn^{2+}, but when it starts to be depleted, the excess OH^- ions will erode the formed ZnO NWs, instead of being consumed in the growth. For this reason, differences in the precursor concentration or in the growth time can affect the final nanowires diameter. As reported in Figure 35, mean diameters differ in every batch, where the lowest value belongs to the sample from batch 3 (46.8 nm) and the highest to the sample of batch 1 (92.2 nm). Even within one sample, diameters values can be really distant from each other: sample from batch 1 has got at least one nanowire with diameter $D = 48\ nm$ and one with diameter $D = 168.4\ nm$, reinforcing the fact that diameters are difficult to control and very sensitive to a large combination of variables.
Cross-section images are useful to obtain a full picture on the whole sample thickness and nanowire length.

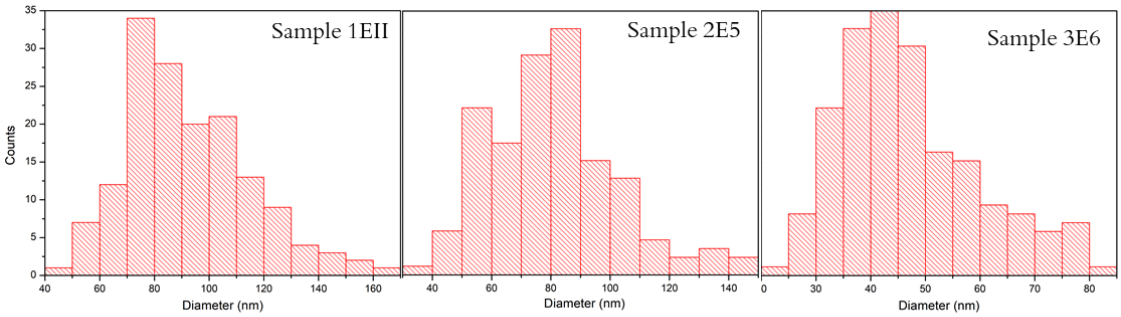

		N total	Mean	Standard Deviation	Sum	Minimum	Median	Maximum
Sample 1EII	Diameters	155	92.18193548	23.23737605	14288.2	48	88.3	168.4
		N total	Mean	Standard Deviation	Sum	Minimum	Median	Maximum
Sample 2E5	diameters	128	80.60234375	21.79993666	10317.1	39.2	79.45	149.1
		N total	Mean	Standard Deviation	Sum	Minimum	Median	Maximum
Sample 3E6	diameters	165	46.80363636	12.92775371	7722.6	24.7	44	81.1

Figure 35 - Diameters distribution of three samples belonging to different batches. On the top, the histograms for each sample are reported; on the bottom, the statistical values related to the same samples. N total is the number of nanowires measured. Mean values are different for each batch, even if they're synthesized in the same way: this suggests that diameters are strongly sensitive to operative parameters and that their values are difficult to control.

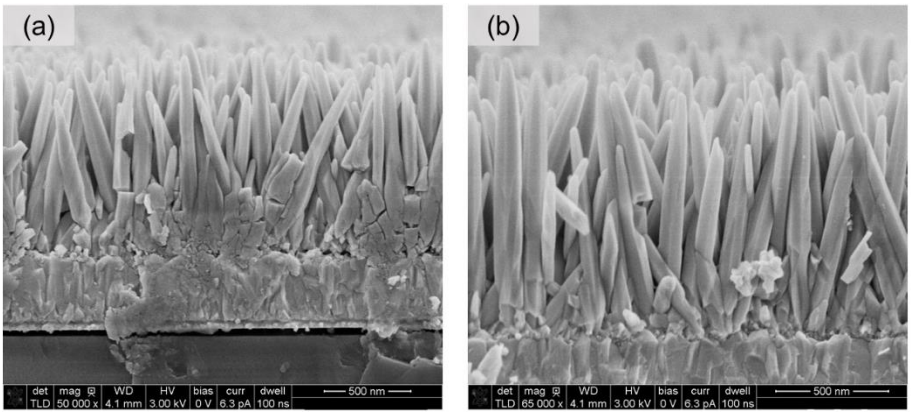

Figure 36 - ZnO nanowires in a cross-section SEM image. The nanowires grow on a seed layer made up of a zinc precursor, which lays on the FTO surface. Nanowires grow quite straight as expected from the synthesis method. Images come from the same sample at two different positions and with two different magnifications, 50.000x (a) and 65.000x (b).

In Figure 36, two images are presented. Nanowires start to grow putting roots down into the seed-layer, which is in turn laying on the FTO substrate; sometimes this region does not appear clearly for the difficulty to discern between seed-layer and nanowires that stopped growing at the beginning, forming irregular nanostructures. It is possible to modulate the instrument magnification to have a farer view (low magnification, Figure 36a) or to look in detail (higher magnification, Figure 36b).

4.1.3 Au nanorods decoration on nanowires: XRD, SEM and EDS

The first attempt to detect gold on sensitized nanowires was made with XRD analysis (Figure 37). The result coming from XRD with bare ZnO NWs (Figure 33) was reported with a black line; the new XRD result, done after Au NRs deposition, was overlapped to the previous one with a red line. A slightly different background signal divides the two curves, making the red one a bit more intense, just to clarify that the peaks are not more intense by themselves. Moreover, no new evident peaks coming from gold are easily detectable; only zooming at $2\theta \cong 45°$ the red curve shows a steeper peak, that may be related to the (002) diffraction plane of cubic gold, according to reference code 96-901-3036. The other gold peaks presented in Figure 37c are either too weak or hidden by the FTO/ZnO signal to appear on the red line, for example the one of (111) plane.

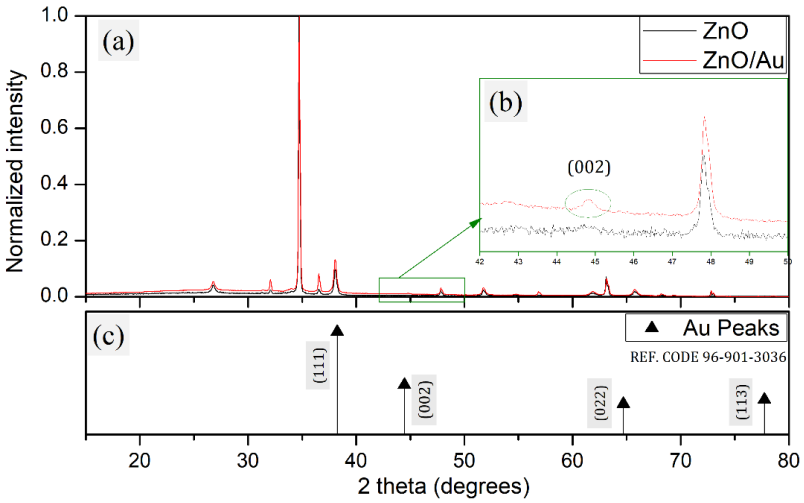

Figure 37 - XRD analysis after Au decoration. The red curve represents the result after gold decoration, while the black one is the same presented in fig.31. The presence of gold doesn't show new clear diffraction peaks (a), but zooming at about 45° an enhanced peak can be detected (b); it is believed to correspond to the (002) plane of gold according to ref. code 96-901-3036 (c).

SEM images were taken to detect the presence of nanorods on the nanowires. The higher the amount of gold solution spilled on the nanowires, the easier to find and see them through the nanowires in any part of the sample. However, being the samples not very homogeneous, the distribution of gold varies throughout the surface and darker regions (rich in gold) interchange with lighter regions (poor in gold). For this reason, even when the amount spilled on the sample is high, it is important to check several points of the sample with SEM to account for differences in the external colour. Figure 38

represents a clear example of this: the sample (ZnO NWs decorated with 200 μL Au NRs) is very dark in the centre, but it shades radially to become lighter and lighter towards the edges, for the presence of a reduced density of nanorods.

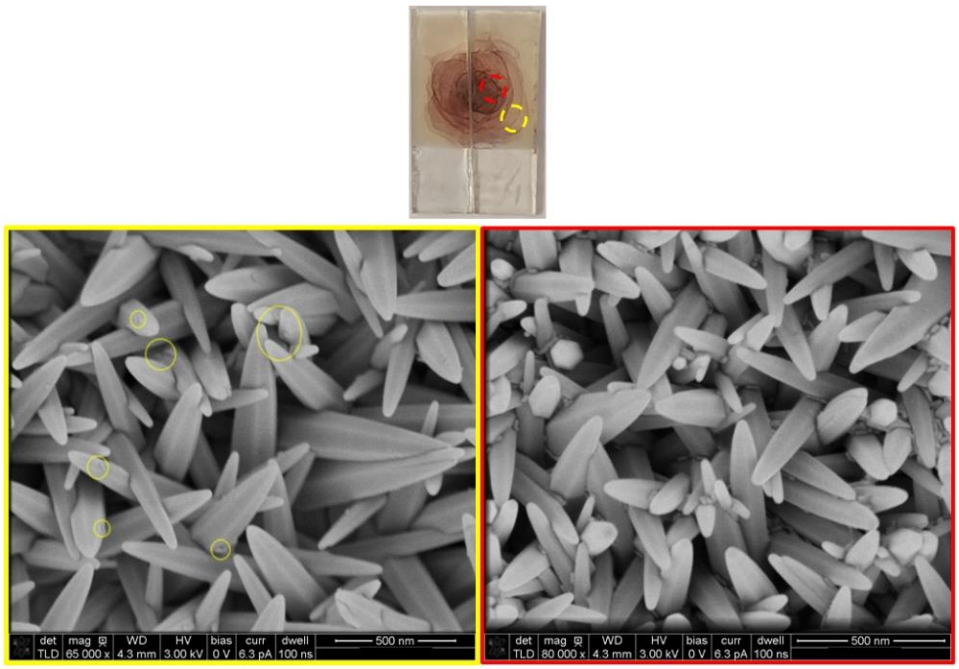

Figure 38 - SEM images taken in two parts at different gold concentrations. The yellow circle represents a low concentration region on the sample and corresponds to the yellow-boarded picture, where only a few nanorods can be seen; the red circle is located on a high concentration region on the sample and the related picture show a bigger number of nanorods throughout the nanowires.

It is therefore fundamental to analyse different regions, to correlate the macroscopic change in colour of the surface and the gradient of nanorods concentration within the sample. Above, on the SEM picture, yellow circles were added to highlight the presence of nanorods in the low concentrated region of the sample, while in the more concentrated one the presence of NRs is self-evident. Further, in this thesis it will be shown that the same concentration gradient can explain variations in optical properties, too.

EDS analysis was performed to detect the elements, which are present in the studied systems. In some regions, which exhibit a drop-like structure, EDS analysis shows the presence of Br and N, which can come from the CTAB surfactant used for the synthesis of Au NRs., considering also the high quantity of carbon revealed in that spot (Figure 39) and CTAB chemical structure (Figure 40). In nanowire region, instead, these signals are not present, and the following elements are detected: Zn, O, Au, Si and Al. Zn and O are

the main constituents of the nanowires, Au comes from nanorods, Si from the glass substrate and Al from the sample holder. EDS measurements confirm the presence of gold deposition.

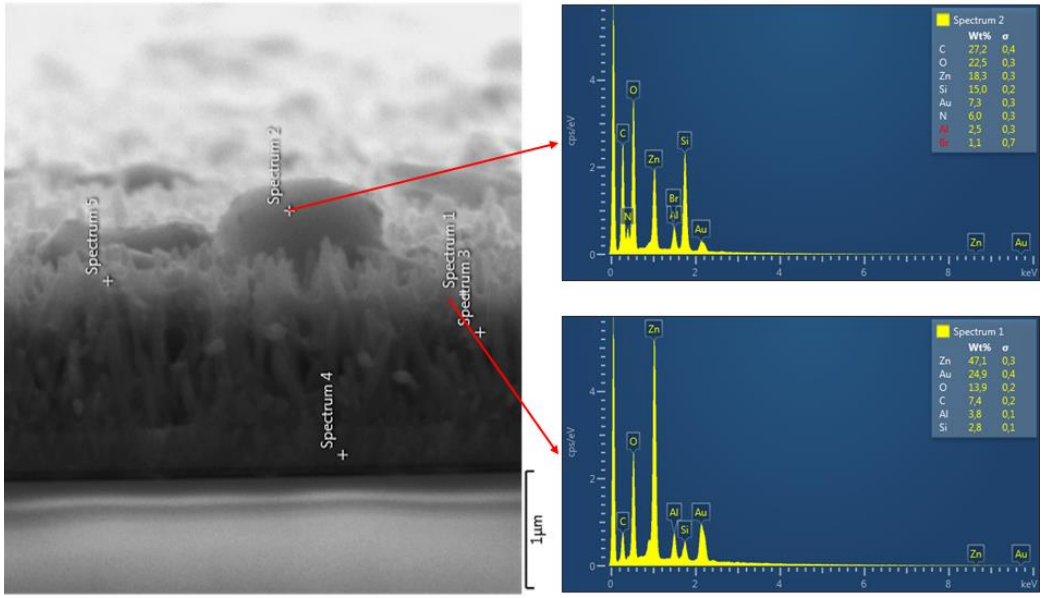

Figure 39 - EDS analysis for qualitative measurement. Spectrum 2 refers to the drop-like structure over the nanowires, which is believed to come from CTAB, being Br and N detected on it. C quantity is higher, too. Spectrum 1 refers to a random point selected on nanowires; Zn, O and Au are detected. Si comes from the glass substrate, Al is the material that makes up the sample holder.

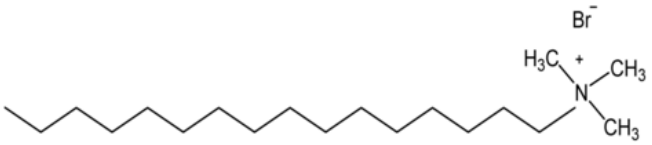

Figure 40 - CTAB chemical structure. The detection of Br and N in EDS measurements is indicative of the presence of CTAB together with Au NRs on the nanowires.

A further analysis was carried through SEM cross-section (Figure 41). In this case, a high Au-concentration sample is shown. Nanorods are clearly visible and they cover a wide area of the nanowires. The possibility of exploiting the plasmonic properties of gold NRs is expected when nanorods and nanowires are in physical contact or sufficiently close in order that the near-field effect can take place. For this reason, external elements, such as CTAB, could interfere with the optical properties, if they create an obstacle for the nanorods to get in contact with ZnO: in Figure 41a, some nanorods can be seen on structures identified as CTAB bubbles, quite far from nanowires with the risk of a loss of efficiency. In Figure 41b bunches of nanorods gather in holes forming agglomerations,

showing that the concentration spilled on the nanowires is a bit too high. However, in Figure 41c it is clear that nanorods cover a wide area on nanowires, with very limited agglomeration, which is the desired condition to study the nanowire-NR interaction.

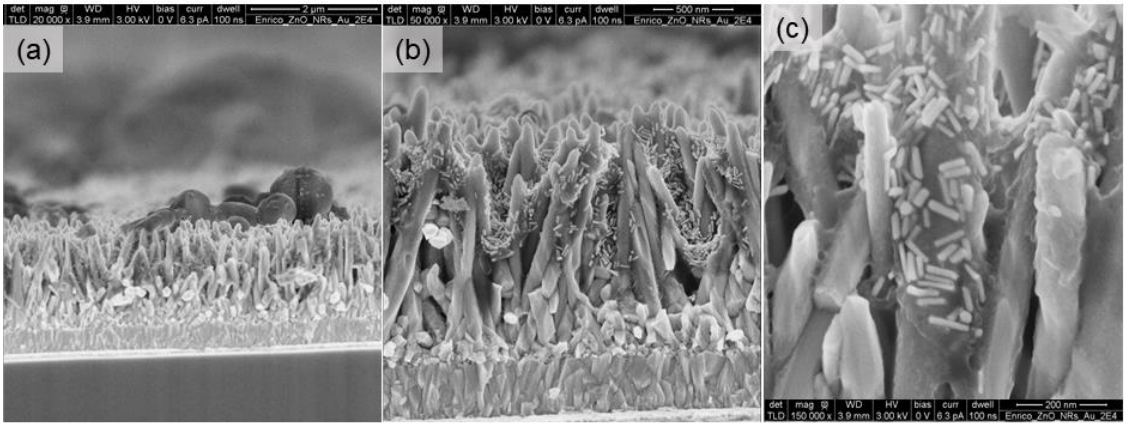

Figure 41 - SEM cross-section images after Au decoration on high concentrated sample. Pictures were taken on the same sample at three different magnification: 20.000x to have a broader view on the sample (a), 50.000x to better observe how the nanorods distribute themselves on the nanowires (b) and 150.000x to look the nanorods in detail (c). The nanorods successfully cover a wide nanowires area, but they also agglomerate laying on each other showing that the concentration added is abundant.

4.2 Optical characterization

The analysis of the optical properties of ZnO nanowires and Au-decorated ZnO nanowires is the most important part of this work. The aim of the Au NRs deposition is to achieve an enhanced absorption of light by ZnO NWs mediated by plasmonic enhancement. To identify this improvement, UV-Vis and photoluminescence measurements were carried on before and after addition of gold, comparing then the absorption and emissions peaks, respectively.

Even if the most direct way to reveal gold effect would be measure the absorption, in this work will be mainly presented transmission spectra, because a wide portion of the light sent to the sample is scattered by the nanostructures; when a steep peak is found around 520 nm, it should be clear that it is coming from gold absorption, more specifically from nanorods transversal band, so that the transmission curve will show a sudden decrease; the same behaviour is expected to be observed in the NIR range, due to the longitudinal plasmonic band of nanorods. Higher concentrations of gold spilled on nanowires are expected to cause higher plasmonic effects, because more nanorods will

absorb more light: peaks belonging to samples with variable gold concentration will be compared for this purpose.

A few diffuse reflection spectra will also be presented in order to display the decrease in the reflected and/or scattered light after addition of gold, which can promote the absorption of that fraction of light that would be scattered from the ZnO NWs.

Transmittance spectra will be also used to estimate the ZnO NWs band-gap through Tauc plot representation, to check the agreement with literature.

Photoluminescence measurements of ZnO NWs are expected to show two bands: one in the UV range caused by excitonic recombination (the so-called Near Band Emission (NBE)); the second one in the visible range caused by radiative recombination from defects levels, called Deep Level Emission (DLE). In order to make comparisons between different samples or in different days, taking into account that the intensity of the exciting beam in the instrument can oscillate giving variable absolute values, the ratio between that emissions (NBE/DLE) will be considered, to get a dimensionless number. DLE suppression is expected after annealing treatment on the sample. After gold deposition, measurements are repeated in order to highlight the changes induced by gold addition.

4.2.1 Pristine ZnO nanowires – UV-vis and PL results

Transmittance, reflectance and absorption spectra are always collected in the spectral interval 350 - 800 nm. Below 350 nm the FTO glass starts to absorb light (E_g~ 3.8 eV). At around 380 nm the absorption from ZnO is of primary importance because it is related to the band-gap energy of this material and generates electron-hole pairs, which can be exploited in photovoltaics technologies. The aim of this work is to absorb even broader wavelengths of the irradiated light through plasmonic absorption of gold nanorods, which show absorption peaks both in the visible and in the NIR because of their two plasmonic bands.

Absorption of photons with energy equal or above the band-gap by ZnO nanowires is detected easily in the following plots (Figure 42). It is easy to claim that photons with energy similar or above the band-edge of ZnO NWs are efficiently absorbed by the nanostructures. Approaching the wavelength ~377 nm both transmittance and reflectance

undergo a sudden decrease heading to zero. If transmittance is null, light must be absorbed, reflected or scattered.

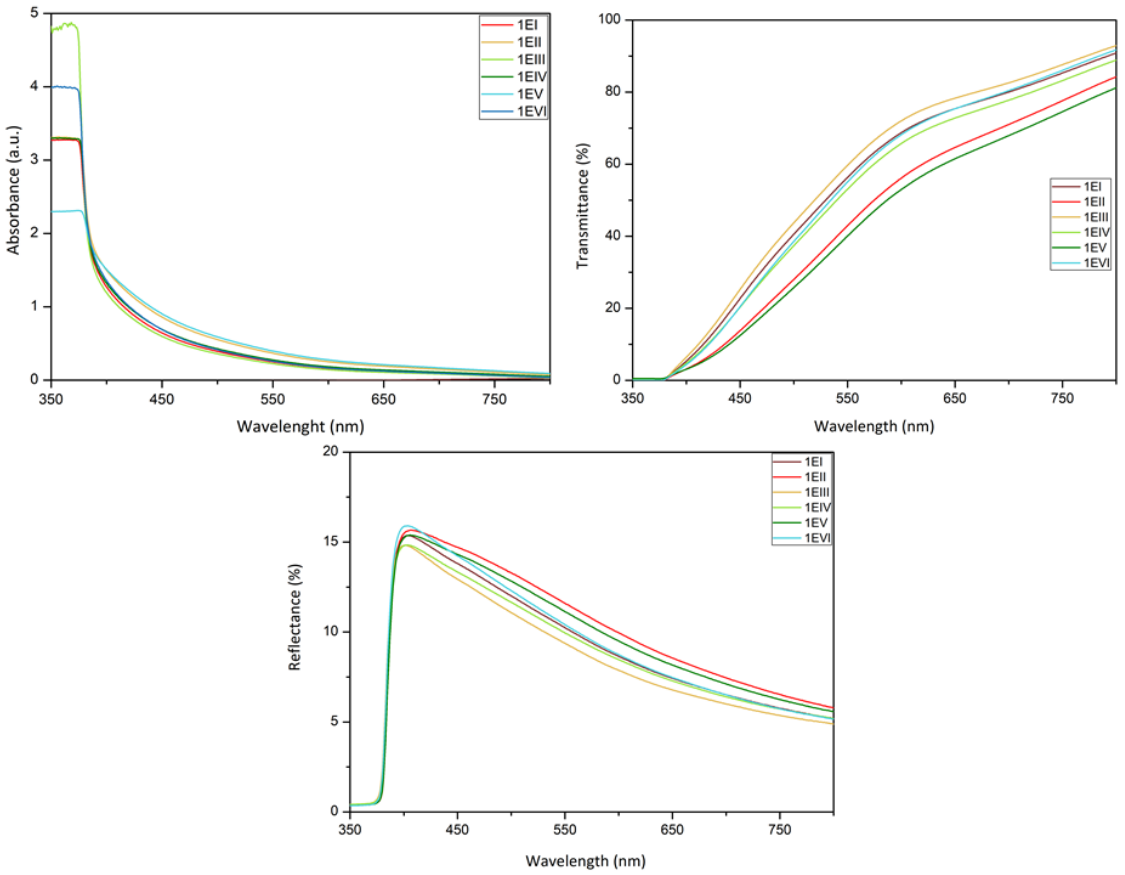

Figure 42 - Absorbance, transmittance and reflectance spectra of batch 1 ZnO samples. ZnO nanowires strongly absorb light of wavelength ~377 nm because it's the energy needed to create excitons. Higher energies are also absorbed, but the excess energy is lost as heat. Obviously, the absorption of light affects the transmission and the reflection, too, which must decrease.

The third plot of Figure 42 represents the measurement of the diffuse reflection, which considers both the normal reflection and back-scattering (reflection following different paths than the approaching one); the value for wavelengths $\leq 380\,nm$ almost zero, indicating that all this portion of spectrum must be absorbed. Generally, in the visible range it can be desirable to keep a high transmittance, especially for aesthetic reasons in building-integrated photovoltaics. It was demonstrated that longer and thicker nanowires result in lower transmittances, and the same effect can originate from less-ordered alignment of the nanowires[66].

Referring to Figure 43, the sample from batch 1, characterized by higher mean diameter ($D = 92.2\,nm$), was compared with the sample from batch 3, where the mean diameter was lower ($D = 46.8\,nm$). The higher transmittance in the visible range is

reached by the sample with thinner nanowires, while the other one is believed to scatter light more having thicker nanowires.

The samples in batch 3 present irregular surfaces, especially in samples 3E3, 3E4, 3E5, 3E6; the transparent parts derive from incomplete growth of NWs in that spots. FTO glass has better transmittance of ZnO NWs, so the result suggests the possibility that in these samples the transmittance is higher not due to enhanced scattering, but because of the synthesis voids, which substitute ZnO with glass (Figure 44).

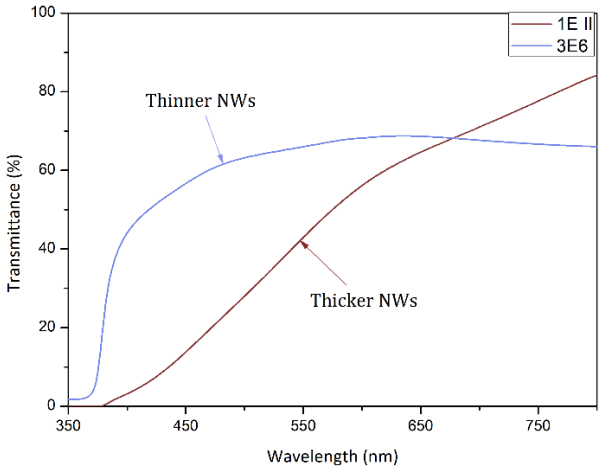

Figure 43 - Comparing transmittances of sample with different mean diameter nanowires. Data from Figure 35 suggest that sample from batch 1 (brown line) has got thicker NWs, while the sample from batch 3 (blue line) has got thinner NWs. Thicker NWs scatter light more efficiently, so that a smaller fraction can be transmitted.

Figure 44 - Picture of the samples in batch 3. Except for the first and the second, they show irregular surfaces, where many spots look more transparent because the growth of NWs was occasionally unsuccessful.

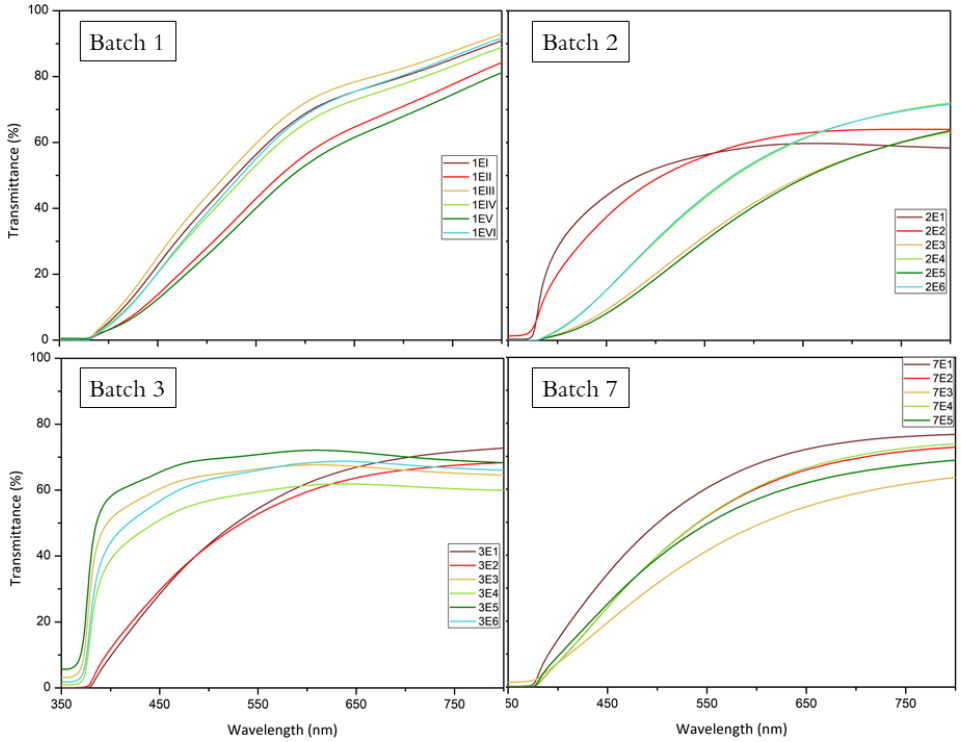

Figure 45 - Transmittance spectra of four different batches. In all of them the decrease at ~377 nm due to excitonic absorption is seen. Four samples in batch 3 show higher transmittances, but it's probably caused by voids in the synthesis that left some parts of bare glass.

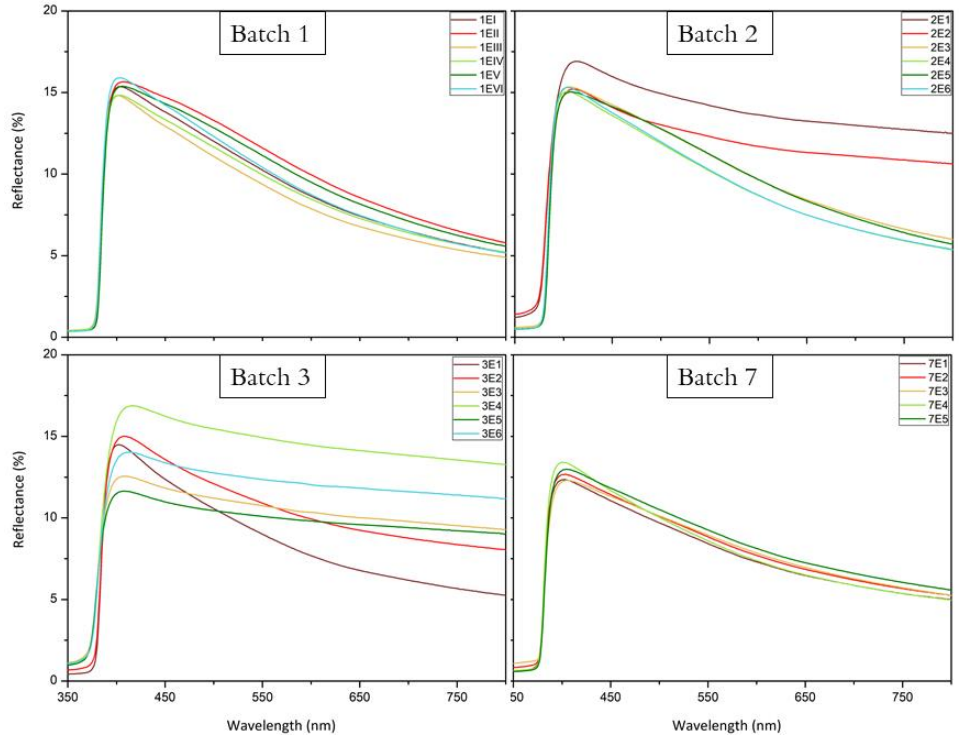

Figure 46 - Reflectance spectra of four batches. As well as seen in transmittance spectra, the decrease at ~377 nm comes from band-edge absorption. The plotted diffuse reflection takes into account both reflection and scattering.

Figure 45 collects all the transmittance spectra for the analysed batches. Batch 6 is not present because it was synthesized to focus on photoluminescence properties, so this measurement was not performed on it. For all the samples, the absorption of photons with energy similar or higher than ZnO band-gap (~ 377 nm) was perceived, and this proves the correct synthesis of ZnO nanostructures. For some samples in batches 2 and 3, a higher transmittance is preserved towards lower wavelengths; as previously stated, this can be the effect of either a stronger scattering by thicker nanowires, or the incomplete synthesis of NWs that produced some "voids" occupied by the underlying glass, characterized by higher transparency. This possibility is further strengthened by the fact that some of these samples clearly do not reach perfectly zero transmittance (%) at the band-gap energy, result of the interaction with light by glass rather than by ZnO.

Figure 46 displays the diffuse reflectance spectra of all the samples divided in batches. The signal in diffuse reflectance includes both light reflection and scattering. For every sample, the reflectance is almost zero approaching the band-edge absorption value. In some samples small signal is present even below 377 nm, most probably due to regions of the sample not fully covered by NWs, which originate non negligible reflection.

The energy gap of ZnO can be determined through the Tauc plot. As reported in the opening paragraph about ZnO (par. 1.6.1), its direct band-gap equals 3.37 eV at room temperature; this value holds when considering bulk ZnO, but it might change in nanostructured ZnO. The band-gap of different samples was estimated through Tauc plot, which can be calculated from equation 14 by plotting $(\alpha h\nu)^2$ vs $h\nu$. The absorption coefficient α can be calculated from absorption spectra as:

$$\alpha = 2.303\frac{A}{t} \tag{19}$$

where A is the absorbance derived from UV-Vis measurement and t is the thickness of the sample, in this case 2 mm.

The procedure used is shown in Figure 47 taking as example batch 1; the same extrapolation method was carried on with batches 2, 3 and 7, too. The estimated band-gaps are collected in Table 6.

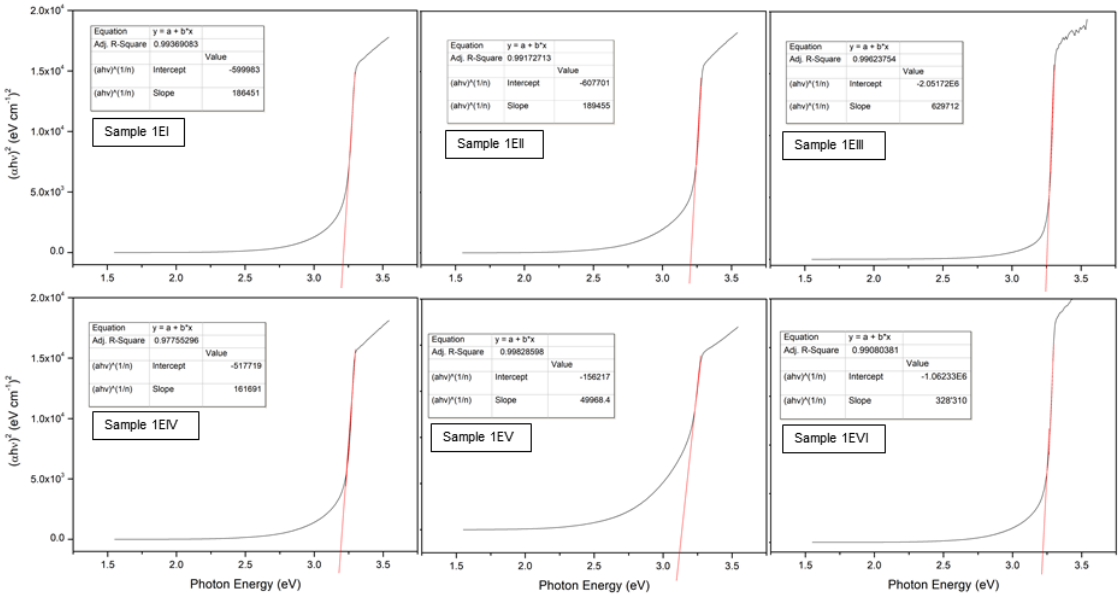

Figure 47 - Tauc plots of batch 1 samples. The linear tract was extrapolated to intersect the x-axis, which represents the photon energy, therefore an estimation of the band-gap. In the tables inset, the values of intercept and slope of every linear fit (red lines), which were used to calculate the value of x for y=0.

Sample	Band-gap	Sample	Band-gap	Sample	Band-gap	Sample	Band-gap
1EI	3.22	2E1	3.20	3E1	3.24	7E1	3.22
1EII	3.21	2E2	3.08	3E2	3.13	7E2	3.23
1EIII	3.26	2E3	3.18	3E3	3.20	7E3	3.07
1EIV	3.20	2E4	3.28	3E4	3.19	7E4	3.23
1EV	3.13	2E5	3.28	3E5	3.20	7E5	3.26
1EVI	3.24	2E6	3.29	3E6	3.19		

Table 6 - Band-gap estimation of samples belonging to batches 1, 2, 3 and 7. Values much distinguishable may come from estimations done on curve tracts not perfectly linear.

Figure 47 presents the Tauc plots of all the samples from batch 1. The linearity region was quite evident in every sample, so its extrapolation was immediate. Tauc plot allows to estimate the band-gap value of ZnO NWs just by intersecting this extrapolation with the x-axis. In some samples, the curve does not show an explicit linear region, so that the estimation is affected by larger uncertainty. This happened, for instance, in samples 1EV, 2E2, 3E2 and 7E3, which present values far from the others. Excluding these values, the mean of all the other band-gaps give 3.23 eV. As mentioned before, band-gaps are different from the one assigned to bulk ZnO (3.37 eV). The results for all the samples are listed in Table 6. They are consistent with the ones found in literature, for example it was

calculated a value between 3.17 and 3.24 eV for ZnO nanorods by Sáenz-Trevizo et al.[67]. According to V. Srikant and D. R. Clarke[40], who obtained similar results, the lower band-gap, compared to bulk value 3.37 eV, could be due to micro-strains arising from the chemical synthesis of NWs, which heavily influence the optical band-gap of the material. Other authors claim that decreasing the dimensions of ZnO structure from bulk material to nanostructure, the band gap should increase as a result of quantum confinement theory, according to which electrons and holes are confined in the respective bands by potential barriers of the surface or potential well of quantum box, making it more difficult to move on to a higher energy state; this is true but limited to very small nanostructure dimensions. For example, an increase of the band gap was confirmed by Meili Guo and X.D. Zhang in ultrathin wurtzite ZnO nanowires of less than 1 nm diameter[68]. However, the dimensions of our NWs are far above the predicted ones to have any quantum confinement effect.

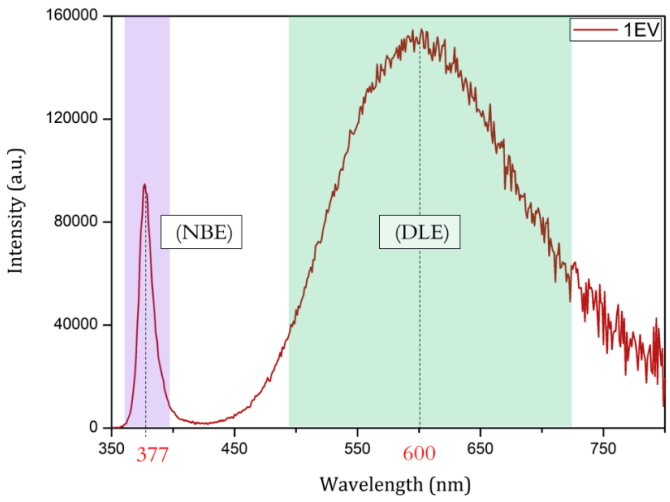

Figure 48 - Photoluminescence of ZnO nanowires. Sample 1EV is taken as example. In each ZnO sample two emissions are visible: one centred at ~ 377 nm caused by excitonic recombination (Near Band Emission, NBE), and one centred at ~ 600 nm due to defects-related emission (Deep Level emission, DLE). Excitation wavelength is $\lambda_{exc} = 325\ nm$.

Photoluminescence (PL) represents the critical part in this project. A typical PL curve resulting from the measurement in a ZnO sample is shown in Figure 48, where sample 1EV is taken as example. In photoluminescence a monochromatic radiation shines on the sample, that emits light, which is collected from a detector. The excitation wavelength is important to determine the PL emission. In this thesis we used an excitation wavelength $\lambda_{exc} = 325$ nm, which is the most commonly used for ZnO, able to

simultaneously excite both the near band edge emission (NBE) and the deep level emission (DLE) bands. The emission splits in two bands: one in the UV range, centred around 377 nm and caused by direct recombination of excitons through an exciton-exciton collision process, called near band emission (NBE); the second is in the visible range and is called deep level emission (DLE), referring to the presence of defect traps within the band-gap. The intensity in the y-axis is an absolute value that depends on the samples, on the spot chosen and on the instrument, too; it is difficult to compare results based only on this value. A more reliable comparison between samples can be done by considering the ratio between the intensity of the two emissions: NBE/DLE, which is independent from the absolute intensity of the signal. The NBE/DLE ratio present strong variations sample to sample. In some cases, in NWs after synthesis, without any surface treatment, it might happen that DLE > NBE, due to the large number of defects arising from the hydrothermal process, especially on the sample surface. An effective way to reduce the DLE emission is to passivate these defects through annealing. The heating of the sample takes place in a furnace at 300°C for one hour, in ambient atmosphere. The effect on the photoluminescence is shown in Figure 49. An increase of the NBE/DLE ratio coming from the increase of the NBE and decrease of DLE is registered.

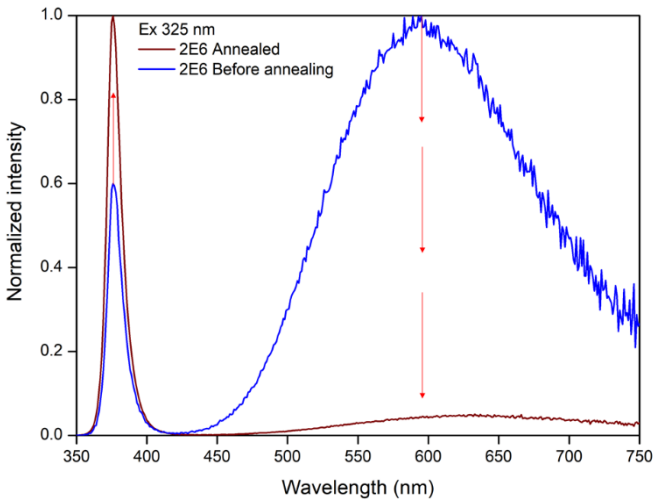

Figure 49 - Annealing effect on 2E6 sample. Blue curve represents the result of photoluminescence on the sample obtained after synthesis; red curve was obtained after annealing the sample at 300°C for one hour in ambient atmosphere. The effect of the heat treatment is to passivate defects, which show a decrease in the DLE. At the same time, an increase in the NBE is registered.

The explanation is that electron-hole pairs created by the radiation can recombine easier through the bandgap, without being trapped in defect levels, and the radiative

excitonic recombination is enhanced. After annealing, it is suggested that oxygen vacancies, which contribute to visible emission, combine with oxygen ions during the treatment, reducing the available recombination centres for electrons.

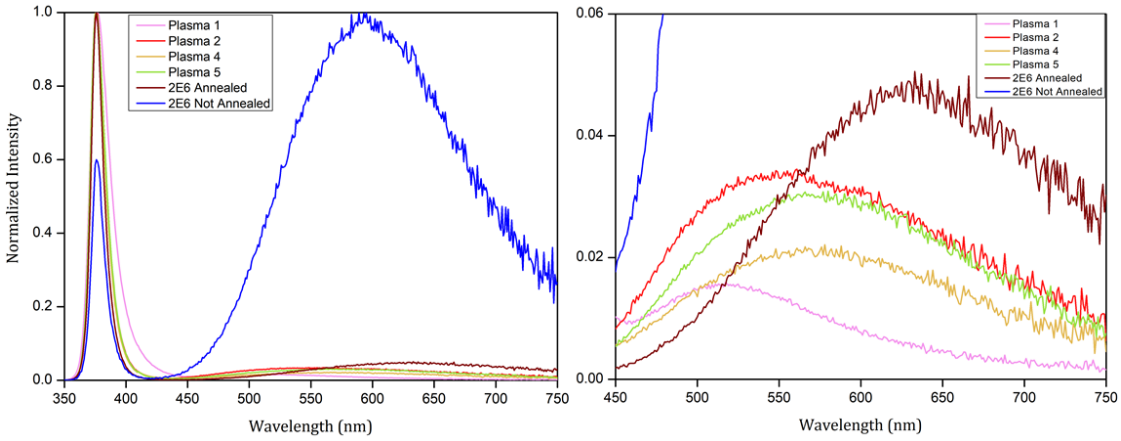

Figure 50 - Plasma treatment as alternative to annealing. The decrease of the defects emission is even stronger than the one coming from annealing. The intensities are normalized in both plots; on the right, a zoom into the defects emission is provided. Treatments in oxygen and hydrogen may move the centre of the peak towards lower wavelengths.

Plasma treatment is an alternative way for defect passivation. In Figure 50, four samples are added in comparison to the one synthesized and treated through thermal treatment in the laboratory (2E6, before and after annealing):

- Plasma 1: treatment in H_2 using 100 passes;
- Plasma 2: treatment in H_2 with only one pass;
- Plasma 4 and 5: treatment in O_2 with one pass.

It can be noticed that defects of plasma samples emit less than the ones in 2E6 sample after annealing, but this may be due to the sample itself rather than to the process. The interesting fact is that the centre of the peaks are different in plasma-treated samples: in oxygen treated samples (4 and 5) the DLE peak sets around 560 nm; in plasma 2 the peak is ~ 550 nm; in plasma 1 it moves towards ~ 520 nm. Each peak position can be attributed to a particular emission. Certainly, the emission at ~ 377 nm comes from the radiative recombination of free exciton; the peak at ~ 520 nm detected for plasma 1 sample can be related to recombination of electrons in the singly ionized oxygen vacancies with photo excited holes in the valence band[69]; for the other plasma samples with peaks ~ 550 nm the emission can be attributed to recombination of electrons with deeply trapped holes in

the oxygen interstitials, and still oxygen interstitials located at different energy levels are thought to be responsible for the radiative recombination of electrons giving the emission at ~ 600 nm[70].

4.2.2 ZnO/Au system: plasmonic enhancement

We carried out UV-vis measurements after the decoration of ZnO NWs through Au NRs to study the influence of plasmonic absorption.

Figure 51 represents the transmittance spectra of six samples: 1E2, 2E5 are ZnO bare samples, without gold; "1E1 light" and "6E4 light" are ZnO NWs decorated with Au NRs, in which the measurement is take in a spot of lighter colour (corresponding to low NR density). In the samples labelled "7E3 dark", "2E4 dark" the signal comes from a darker red colour region, with higher NR density. The measurement spots are shown by yellow and red circles, for lighter and darker samples, respectively. Moreover, for each category, two samples are presented in order to consider annealing treatments: in the plot, solid lines represent not annealed samples, whereas dash lines are attributed to annealed samples.

The transmittance of the pristine ZnO samples presents the typical curve already seen before, where the transmittance approaches zero at ~ 377 nm for the effect of ZnO absorption; no difference is observed between annealed and not annealed samples. In "light" the low concentration of NRs makes the plasmonic absorption peaks not clearly evident, even if slight changes on the slope between 510 and 520 nm can be observed. However, there is no evidence for the longitudinal plasmonic band, which should arise in the NIR region.

SAMPLE	TRANSVERSE PEAK POSITION
1E1	~ 517 nm
6E4	~ 513 nm
7E3	~ 512 nm
2E4	515 nm

Table 7 - Transverse plasmonic peak position for the four gold samples.

Finally, the two darker samples show the most evident absorption peaks, both the transverse at around 530 nm and the longitudinal one with a very broad absorption centred around 850 nm, which is near to the calculated value from equation 15 ($\lambda_{max} = 862\ nm$). The position of the transverse plasmonic peak is quite stable and its values for the gold samples are reported in Table 7.

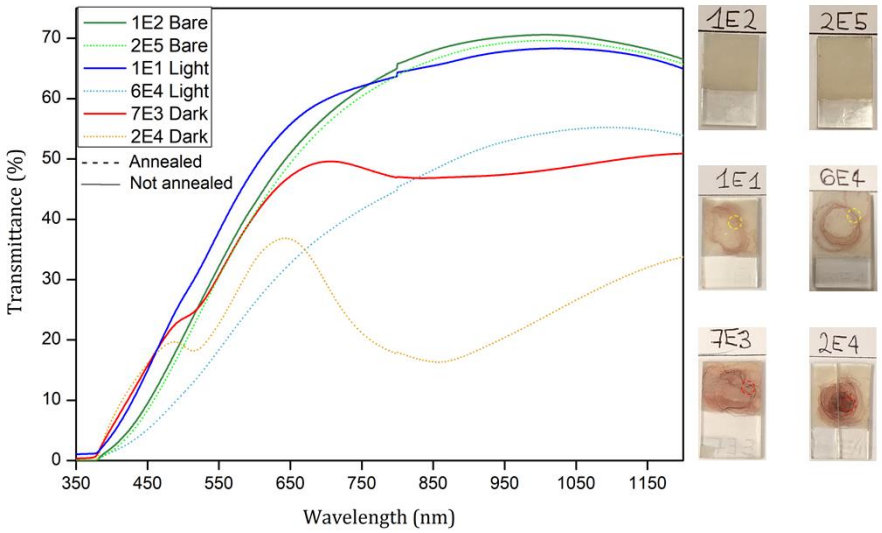

Figure 51 - Transmittance spectra of two bare ZnO samples, two "light" and two "dark" gold samples, referring to the colour and related to the concentration of gold inside. Transverse plasmonic peaks are present in the range 512 ÷ 517 nm. Longitudinal plasmonic peaks are very broad yet visible only for the dark samples. No differences are reported between annealed (dot line) and not annealed (straight line) samples. On the right, pictures presenting the six samples measured and indication of the analysed spot.

To get better insight and highlight the presence of the transverse peaks, it is possible to differentiate the data shown in Figure 51 in the region of interest. In this way, the peaks result more evident (Figure 52). As expected, darker samples show the deepest peaks also in the first derivative plot; the important result is that also the lighter samples show plasmonic peaks, giving the proof that even in smaller amount gold has a primary role in absorbing more light. Diffuse reflection spectra are affected by plasmonic absorption, too. In Figure 53 the comparison of the reflectance collected by sample 2E4 before and after addition of gold NRs are reported. The blue line is the curve related to the bare ZnO sample, and only shows the band-edge absorption at ~ 377 nm due to the nanowires. The dark red curve was obtained after Au decoration; it clearly shows that reflectance falls down rapidly according to the two plasmonic bands in the visible and in the NIR.

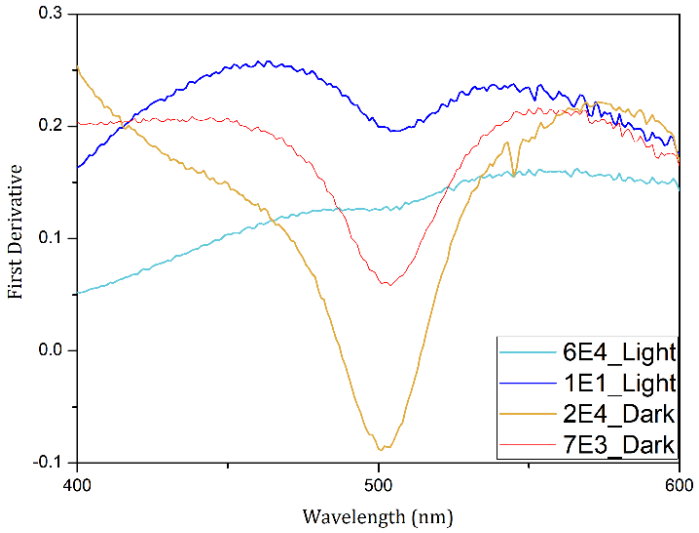

Figure 52 - First derivative of the transmittance data. In this way, the peaks become more evident and a new proof of the plasmonic absorption is given. As expected, the peaks height is higher for darker samples, where the plasmonic absorption was already distinguishable from the transmittance plot.

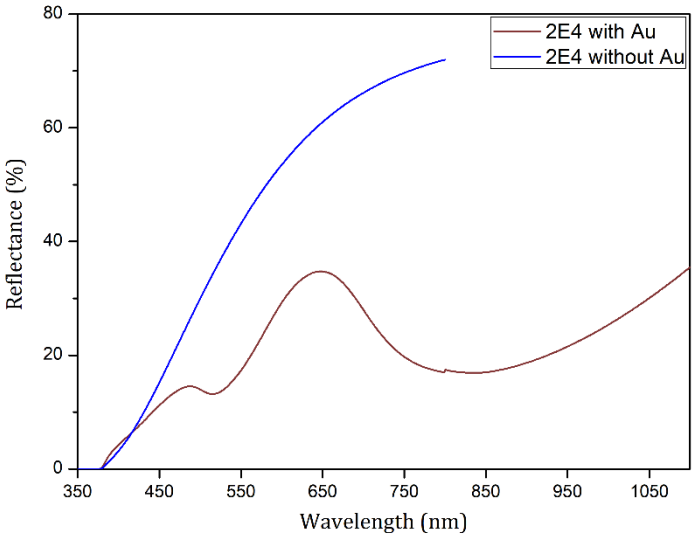

Figure 53 - Reflectance of 2E4 sample before (blue line) and after (red line) addition of gold. The appearance of the two plasmonic bands is evident, even if for the bare ZnO sample the measurement range was limited until 800 nm.

These plots further demonstrate that in presence of gold nanorods, light is absorbed rather than reflected or scattered, so that they can be useful in enhancing absorption in solar cells.

4.2.3 ZnO/Au system: single emission photoluminescence

Figure 48 showed a typical photoluminescence curve for bare ZnO NWs. The decoration with gold brings a new species in the system, so that differences in photoluminescence response may be expected. In literature, it is demonstrated that gold can actually improve NBE through an energy transfer process.

R. Khan et al.[71] found that NBE of ZnO nanorods/Au NPs had a peak magnitude 2 times higher in comparison with ZnO without gold, and that this increase was accompanied with a decrease in the DLE. Na Zhang et al.[72] even showed an increase of up to 92 times in a system with ZnO nanowires and sputtered gold. The latter nanocomposite was studied by Tsai-Ching Chiang et al[73], too, who related different NBE enhancement ratios according to variable sputtering deposition times. All these articles explain the result considering a pumping effect on the electrons in ZnO defect levels to the conduction band of ZnO exploiting LSPR of gold. The conduction band of ZnO is at -4.19 eV with respect to absolute vacuum scale, whereas the Au Fermi level sets at -5.30 eV: the band alignment explains the suppression of defects emission. The defect level in ZnO is around the Au Fermi level, which means that the emitted visible light photon energy of ZnO NWs matches the SPR energy of Au. When the resonance is reached, the electrons in gold are excited through surface polariton waves. Afterwards, these electrons are transferred back to the conduction band of ZnO. The overall effect is a transfer of energy from defect levels to the conduction band of ZnO, and the process is mediated by LSPR of gold, that can be excited by defect emission of ZnO. The result is that the band-edge emission is enhanced, while the visible emission is quenched, as effect of the electron density variation in these levels. The explained mechanism is schematically presented in Figure 54.

In some studies, instead, a suppression of the NBE emission is registered after decoration with gold. In this case, the electron transfer from the conduction band of ZnO to Au dominates, so that NBE can be reduced. This behaviour was proved in ZnO with negligible defects: after coating Au NPs on ZnO NRs, the excitonic emission decreased because, without surface plasmon resonance induced by defect emission, the electrons in Au particles stay in lower energy levels without the possibility to move towards the ZnO conduction band[74].

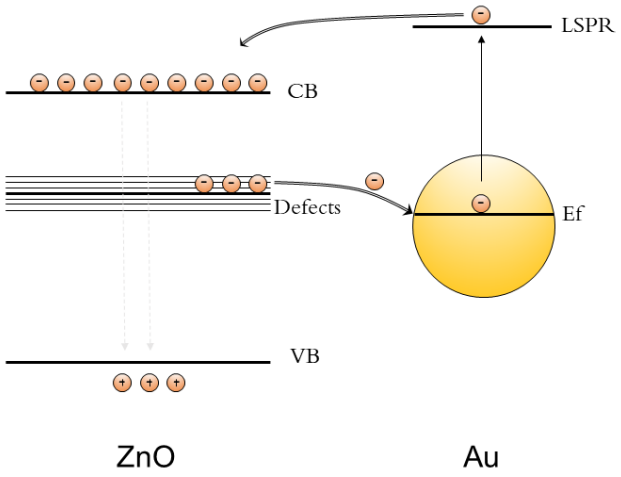

Figure 54 - NBE enhancement after decoration with gold. The mechanism includes the transfer from defect levels of ZnO to Au Fermi level due to band alignment. Then, visible emission of ZnO activates LSPR in gold, because the wavelengths match: this allows electrons to gain energy. Finally, the electrons can be transferred back to the conduction band of ZnO. The effect is the increase of NBE and decrease of DLE.

Instead, in depositions of gold films by sputtering, it is possible that, when the deposited film is too thick, the emissions from ZnO are shadowed by gold, for example when the sputtering time is too long[74].

M. M. Brewster et al[75] explained different photoluminescence results according to presence or absence of gold nanoparticles, while ZnO nanowires are grown: in Au-assisted growth the quenching is lower as effect of higher Schottky energy barrier produced (1.06 eV versus 0.67 eV of non-assisted growth), so that electrons diffusion from ZnO conducting band to Au Fermi level is more difficult. Ya-Ping Hsieh et al.[76] linked photoluminescence variations to the quantity of gold decorated on CdSe quantum dots: the emission quenching originates from electron transfer at the interface semiconductor/metal when higher concentration of gold causes a distance reduction with CdSe quantum dots, making the flow of electrons easier. It is even possible that electrons moved from ZnO conduction band to Au Fermi level will be eventually delivered again towards ZnO defect levels, if they are situated below Fermi level of gold, causing a suppression of NBE and enhancement of DLE[77]. Moreover, there are many examples of electron transfer from ZnO to gold in photocatalysis applications, where metals are used as redox catalysts. For example, A. Wood et al.[78] observed electron transfer from ZnO quantum dots to Ag, Au and Cu islands deposited onto them; UV irradiation makes electrons accumulate on ZnO and then depleted toward metal islands, where they are stored until some solvent (in their case ethanol) applies a scavenging effect on them. The

Fermi level in the metal is shifted until it merges with the quantum dot conduction energy level, since almost all excess electrons accumulate on the metal island. It must be said that, in presence of air, a supplementary and faster scavenging action is carried on by oxygen, that manages to deplete both sides of the nanojunctions; blowing nitrogen in the system, the action of oxygen may be cancelled, but in this case quantum dot hole depletion can still occur because of the oxidation process that interest ethanol, producing ethanal.

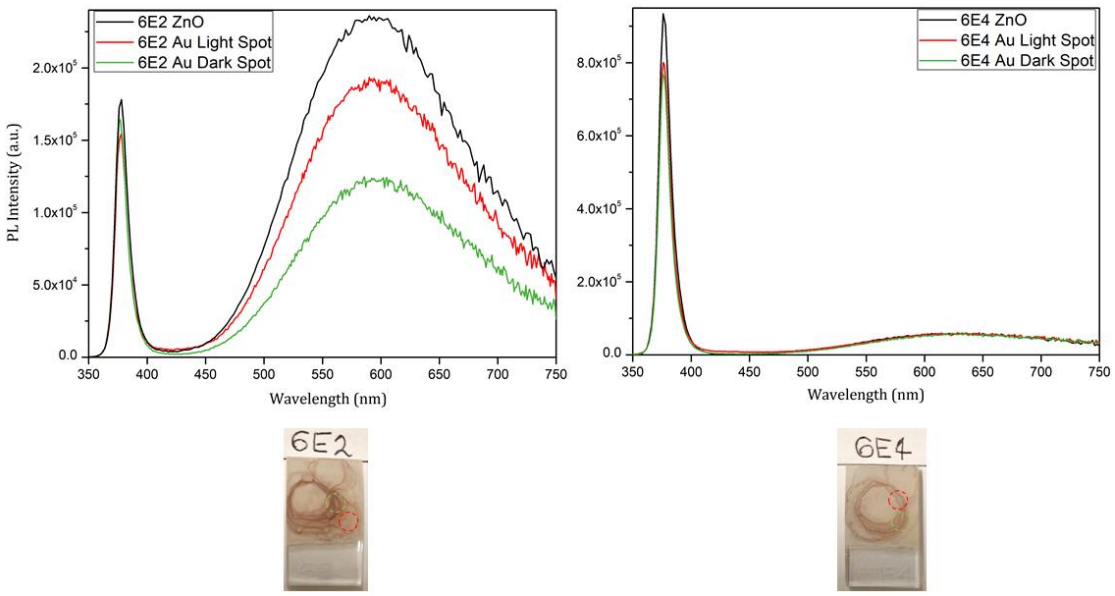

Figure 55 - Photoluminescence results before and after Au addition for not-annealed (6E2) and annealed (6E4) samples. Measurements were taken two times, in different spots to account for different concentrations. Not-annealed sample shows an enhancement of NBE/DLE ratio on the darker spot, while on the light spot no difference is seen. Annealed sample shows NBE suppression on both spots, while DLE is stable. Spots positions are reported on the samples pictures below.

Figure 55 represents the results of photoluminescence measurements on two ZnO/Au samples. On the left, a picture of 6E2 sample shows two different concentrations spots where the measurements took place: the red circle represents a low Au-concentrated region whereas the green one represents a high Au-concentrated region. The same was made for sample 6E4, on the right. The difference is that sample 6E2 is not annealed, whereas 6E4 was annealed after ZnO NWs synthesis and before decoration with Au NRs, in the conditions explained previously in this thesis. In the above plots, the curves are related to pristine ZnO response (black line), low Au concentration spot (red curve) and high Au concentration spot (green curve). Looking at the black curves, it is clear that

defects emission in 6E4 was suppressed by the annealing process; in 6E2 sample, instead, $DLE > NBE$.

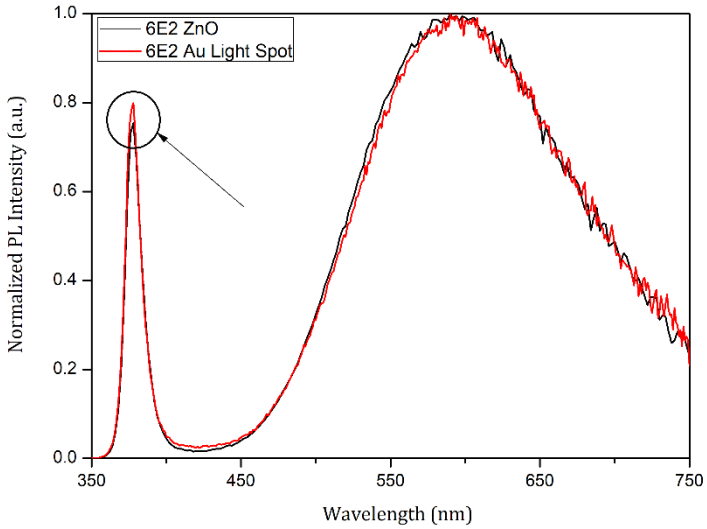

Figure 56 - Sample 6E2 NBE and DLE peaks before and after gold addition, normalized to the highest value of each DLE. The sample without gold (black curve) has a lower NBE peak than the decorated sample, so that NBE/DLE ratio increases after gold addition.

	Pristine 6E2	Au 6E2 Light Spot	Au 6E2 Dark Spot
NBE/DLE Ratio	0.75	0.80	1.32

Table 8 - NBE/DLE ratio values of not-annealed 6E2 sample. After Au addition, the ratio increases slightly in the light region and evidently in the dark region compared to the pristine ZnO sample.

The measurement was repeated after decoration with gold. In the not annealed sample, the situation doesn't change that much according to the light spot: both NBE and DLE are slightly suppressed, even if the latter is decreased a little more. This can be highlighted normalizing in respect to DLE peaks the two spectra; NBE peak of sample 6E2 with low amount of gold is slightly higher than NBE peak of pristine 6E2 ZnO (Figure 56). However, the evident change is discerned on the dark spot: while the NBE is slightly decreased, a large decrease in the DLE is seen, so that the NBE/DLE ratio is evidently increased (Table 8). 6E4 annealed sample is characterized by a stable defects emission before and after Au decoration, no matter which spot was taken. In both the points, a suppression of the NBE was registered, so that the NBE/DLE ratio became lower after addition of gold. The absolute decrease of the peaks in both samples is tricky to explain; as mentioned before, the absolute intensities given by the detector are easily influenced by the instrument mechanics, so that it is necessary to describe gold effect in

terms of NBE/DLE ratio, being a dimensionless value. In the end, it is possible to state that the not-annealed sample is characterized by an improvement of the NBE/DLE ratio, whereas the opposite condition is found on the annealed sample.

The different behaviour between annealed and not-annealed samples might be described according to what was stated earlier in this sub-paragraph. The not-annealed sample is characterized by a wide and strong defects emission, which can activate LSPR effects on the gold nanorods. Some electrons from ZnO defect levels can move to Au Fermi level, being the latter located at a more negative potentials. After UV-excitation, DLE from ZnO may activate plasmonic resonance in Au NRs; the effect is that electrons manage to reach higher-energy states pushed by the resonance. These electrons can move back to ZnO, in the conduction band, because now it is at an energy level below the one reached by the electrons. This is why in sample 6E2 (dark spot) an evident suppression of DLE is detected and so the increase in NBE/DLE ratio. In the lighter spot, this effect is less evident, yet present. In this case, the lighter colour expresses a lower amount of nanorods present in that region, as shown in Figure 38a. Considering the photoluminescence response, it can be stated that a small number of gold nanoparticles does not effectively pump electrons from ZnO defects levels to ZnO conduction band through LSPR, so that only a limited number of electrons can suppress DLE in favour of NBE.

The annealed sample is characterized by a lower DLE, for the passivation of defects originated by the annealing process. It was underlined earlier that emissions suppressions have been detected in literature, but more than one explanations have been given in order to explain the phenomenon. In the not-annealed sample, the resonance effect was activated by this kind of ZnO emission; it is clear that when this emission fades away, the LSPR effect is not reached anymore. Indeed, this is believed to happen in the annealed sample: the defects emission from ZnO is too low to activate LSPR in gold nanoparticles, which are not able anymore to pump electrons coming from defect levels of ZnO toward its conduction band. This can also explain why there it not such a big difference between darker and lighter spots: if LSPR condition is not achieved, the number of nanorods present in the region does not have any further effect in the photoluminescence response. The only thing that may vary is that some electrons could pass from ZnO to Au Fermi level to get an equilibrium between their energy levels (as in a Schottky barrier). This

may explain why NBE is slightly lower after addition of gold, and also gives a hint about why in the darker spot the decrease is more evident: more nanoparticles might catch more electrons from ZnO. On the other hand, it is not clear if the aqueous solution or the CTAB that are present together with nanorods may affect the process: one possibility is that carriers are scavenged by some species, being depleted from both conduction or valence bands and resulting in a double suppression.

4.2.4 ZnO/Au system: multiple emission photoluminescence

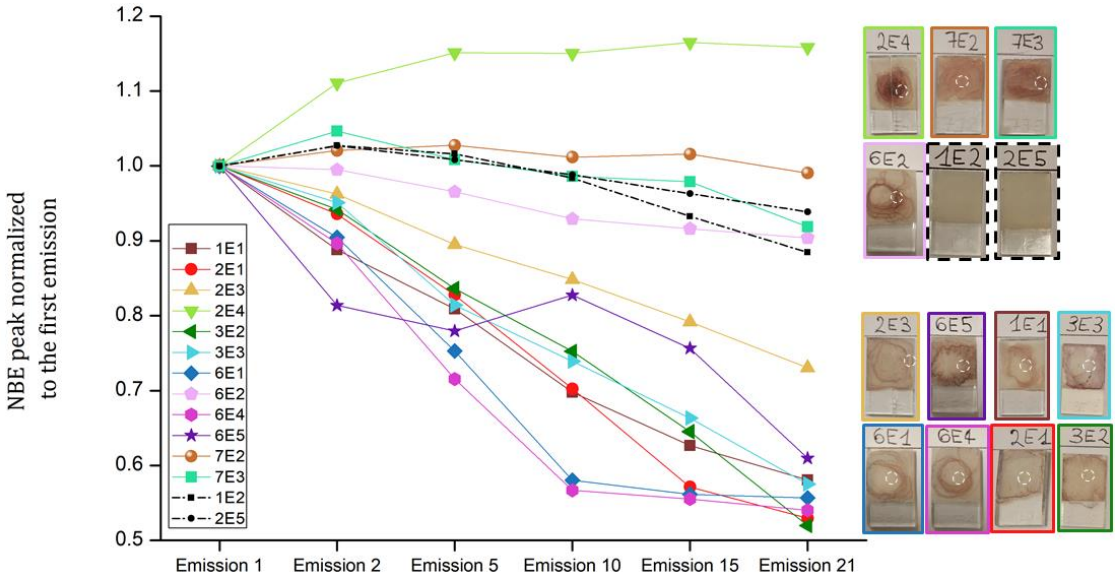

Figure 57 - Multiple emission scans of Au-decorated ZnO NWs. The y-axis is the NBE peak intensity normalized to the first emission intensity at 377 nm for each sample. The other values are collected after 2, 5, 10, 15 and 21 scans. Darker samples (on the right), measured on the white circle spot, show stable or increase of the NBE peak intensity after 21 scans; lighter samples are related to deeper decrease of the NBE peak intensity. Bare ZnO samples (1E2 and 2E5, black lines) act similar to dark samples.

To understand the dynamic behaviour of the samples under continuous irradiation, we studied photoluminescence under continuous excitation for 21 scans one after the other (Figure 27b). It is believed that the response from the sample was related to the amount of gold added on nanowires: darker samples show a stable or even increasing NBE peak intensity during the multiple scan session, while lighter samples are more likely to decrease NBE intensity during the experimental measurement. Figure 57 collects the data from all the Au-decorated samples plus two pristine ZnO samples (1E2 and 2E5). The y-axis represents the NBE peak intensity at the excitonic wavelength of 377 nm at an excitation of 325 nm, normalized to the value of the first NBE intensity for each sample.

This means that the first value is always 1, then for each emission (actually 2nd, 5th, 10th, 15th, 21st emission scans were chosen) the plotted value x is defined as:

$$Value\ (x) = \frac{Value\ (emission\ x)}{Value\ (emission\ 1)} \tag{20}$$

It is clear that if some quenching of the emission occurs during the measurement, then $Value\ (x) < 1.0$. From the figure one can state that samples 2E4, 7E2, 7E3 and 6E2, together with the two pristine ZnO samples 1E2 and 2E5 show a different behaviour comparing to all the other samples, which present a clear suppression of the NBE peak intensity. Since this result appears quite solid, it is believed that the amount of gold is a key factor in the photoluminescence emission: when the spot measured is set on a high Au-concentrated region, then the quenching effect does not appear or it is weaker; in low-concentrated regions, instead, it looks like NBE suppression is more and more evident. Moreover, the two pristine ZnO samples has the same behaviour as the high-concentrated Au samples. This is quite tricky to explain, as there is no sure explanation of the reason why this quenching effect appears. Whatever effect is modifying photoluminescence response of ZnO, it looks like that when a lot of nanorods cover NWs they are able to hide or cover this effect.

To exclude an effect of NWs in determining the aforementioned behaviour, the same sample (with the same NWs) was analysed in two different spots: one set in a darker region, the other in a lighter region. This was thought to underline the effect of the amount of gold, excluding any interfering effect due to different NW condition. Figure 58 shows the results for sample 6E2. As well as other samples, the distribution of Au NRs on it is not homogeneous, so darker and lighter parts can be found (Figure 58d). Multiple emission scans are performed on both spots singularly. The visible result limited nearby the position of the NBE peak is presented in Figure 58a for the dark spot and in Figure 58b for the light spot. The difference is significant: the suppression after 21 scans brings down the NBE peak intensity for a 10% in the dark and a 32% in the light region. The succession of the same six emissions chosen earlier shows that the intensity value for the light spot falls quickly whereas the dark one stays more stable (Figure 58c).

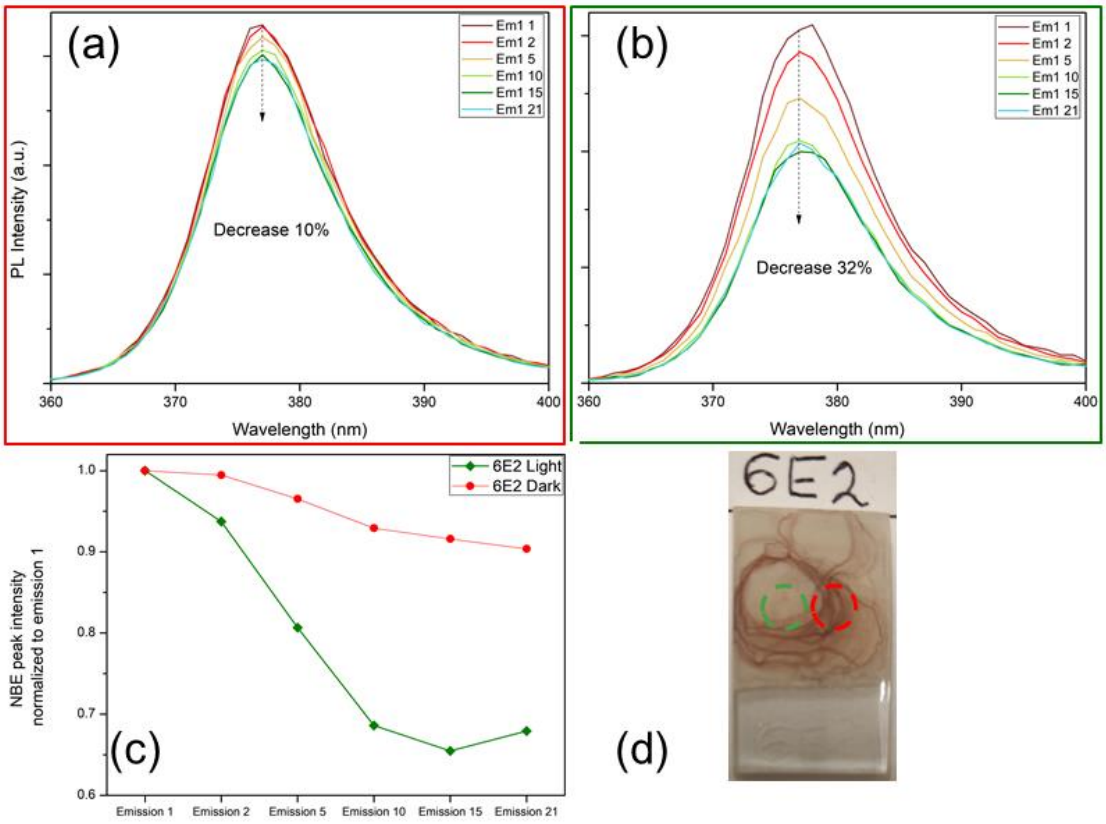

Figure 58 - Photoluminescence emissions on different spots of the same sample. Red and green lines correspond to dark and light regions, respectively. NBE peak intensity at excitation of 325 nm decreases by around 10% in the dark region (a) and 32% in the light region (b). The succession of the peak intensities normalized to the first emission clearly shows that in the light region the emission quenches more (c). The spots on which measurement were taken are represented with circles of the same colours in the picture (d).

Until now, the results focussed on the NBE intensity evolution during multiple emission scans. It was adequately explained before that defects emit, too, in the visible region. The photoluminescence response is even more difficult to explain when DLE is watched carefully. Figure 59 presents a selection of different situations: first of all, 6E1 and 1E1 are not annealed whereas 3E2 and 2E4 are annealed, as clearly evinced by the NBE/DLE ratios. 6E1 and 1E1 are studied in two different spots to account for differences in light and dark regions. In the light spots of both of them, DLE increases during the multiple scan experiment; however, 6E1 increases very strongly, whereas in 1E1 the NBE is strongly quenched and DLE emission is strongly increased, so that the final enhancement is smoother. In the dark regions, 6E1 DLE peak decreases softly, while in 1E1 the opposite trend is recorded, with a slight increase of the DLE peak. Moreover, in the annealed samples, the defect emission looks stable, no matter the concentrations of gold nor the behaviour of the NBE, which is quenched in 3E2 and enhanced in 2E4.

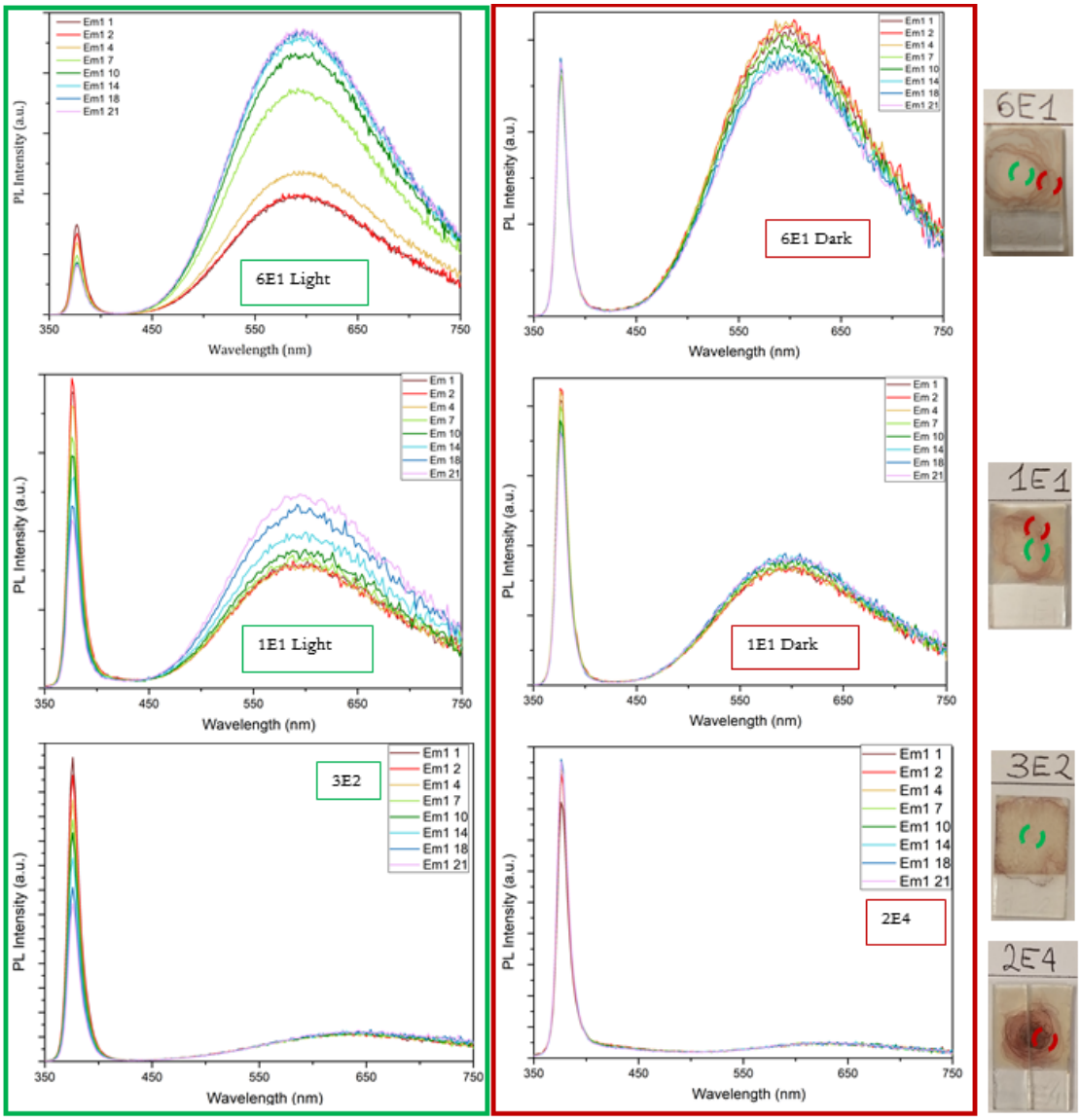

Figure 59 - Focus on the DLE for three dark and three light spots. 6E1 and 1E1 are not annealed. They show an evident DLE increase in the light spots. In their dark side, DLE increase is weaker and less evident. 3E2 and 2E4 are annealed. Their DLE are stable. On the right, samples pictures and identification of analysed spots.

The behaviour of DLE looks not associated with the one of NBE: when NBE peak quenches, DLE peak can rise much more (6E1 light), can rise almost for the same relative quantity (1E1 light), can be stable (3E2). Moreover, it does not even look completely related to concentration of gold, since 6E1 and 1E1 are both high-concentrated in gold, but the former shows a decrease in DLE, while 1E1 shows a slight increase.

The very different responses do not allow an easy explanation of the phenomenon. It is believed that new non-radiative processes may arise during the experiment, making it difficult to understand what the excitation beam causes. It is good to recall that defect

emission are mostly traced back to the presence of oxygen vacancies or interstitials; multiple emission scans are performed in air, so oxygen in some way is believed to play a primary role in the defect emissions. As described in the previous paragraph, NBE quenching could be related to electron transfer from ZnO band conduction to Au Fermi level; these electrons can further move to ZnO defect levels to cause an increase of DLE (6E1 light, 1E1 light and 1E1 dark); simultaneous quenching of NBE and DLE could be explained by consumption of electrons in ZnO conduction band and holes in ZnO valence band with species present in the system, such as oxygen and organic compounds coming from the CTAB surfactant; NBE quench with no changes in DLE could be due to electron transfer from ZnO conduction band to Au Fermi level (3E2). Heating processes were excluded because the samples never seemed to be warmer when taken out from the instrument chamber. Response changes due to morphological differences between light and dark samples were considered: possible formation of thin films of gold in high concentration Au samples could interfere with the excitation and give abnormal emissions. By the way, SEM images taken from dark samples had never confirmed presence of Au films (Figure 38b is an example of high concentration Au NRs distribution).

Some ideas concerning how to get a wider knowledge about the phenomena involved will be suggested in the following chapter.

Chapter 5

Conclusion and future work

Zinc oxide nanowires (ZnO NWs) were successfully synthesized on Fluorine-doped tin oxide glass (FTO) through a two-step hydrothermal method. The presence of HMT efficiently boosts the growth of pre-synthesized seed of ZnO in a preferential orientation along the c-axis. The crystalline structure was confirmed to be a hexagonal wurtzite structure by XRD analysis; preferentially growing along the c-axis. The deposition of gold was performed by simply dropping an aqueous solution containing gold nanorods (Au NRs) stabilized by CTAB over the samples. XRD was carried on again to get a signal from gold traces, even if weak. SEM analysis was carried out before and after decoration with gold. On pristine ZnO NWs, SEM was useful to measure a bunch of nanowires diameters from different samples; it was shown that different batches presented different mean diameters, ranging from 46 nm to 92 nm for the thickest. Gold nanorods were studied by TEM and were characterized by a mean length of 46.9 nm and a mean width of 10.2 nm. After deposition of these NRs on NWs, SEM images were taken to see how gold distributed on ZnO. Differences in the sample surface colour were related to higher concentration of Au (darker colour) and lower concentration of Au (lighter colour) by SEM pictures. EDS analysis suggested the presence of organic compounds still present on the system, most probably coming from Au NRs synthesis and attributable to CTAB. Optical characterization was performed by UV-vis and photoluminescence measurements. Absorption, transmittance and diffuse reflection spectra were observed before and after addition of gold. Concerning pristine ZnO NWs, it was demonstrated that they absorb light at ~ 377 nm due to excitons formation; as a result, transmission and reflection responses approach zero nearby this wavelength. It was also shown that higher transmittance values were related either to thinner nanowires or empty spots on FTO due to inhomogeneous synthesis. Tauc plots were derived from transmittance spectra in order to estimate band-gap values of nanowires, which was around 3.23 eV, in agreement with the expected value. Photoluminescence of ZnO NWs presented an emission in the UV range due to excitonic recombination (Near Band Emission, NBE) at ~ 377 nm and an

emission in the visible range due to trap levels coming especially from oxygen vacancies or interstitials (Deep Level Emission, DLE) centred between 600 nm and 615 nm. Moreover, it was shown that processes such as annealing and plasma treatments can successfully suppress defects emission by their passivation. After deposition of gold, plasmonic absorption peaks were observed in the visible range and in the NIR; the intensity of the peaks were related to the concentration of gold deposited: in fact, the longitudinal bands were evident only in high-concentration samples. The presence of gold influences ZnO photoluminescence emission: it was shown that in annealed samples NBE was quenched, whereas in not-annealed samples it was enhanced. This was explained by electron transfer from ZnO defects levels to Au Fermi level, where electrons can increase their energy when excited by green emission, coming from ZnO defects themselves (LSPR effect), and then passed to ZnO conduction band, enhancing the NBE. Annealed samples cannot activate LSPR, instead, because of their weak DLE, due to defect passivation. Multiple emission scans were also performed on ZnO/Au samples. It was seen that after continuous UV excitation at 325 nm, NBE peaks are quenched more in sample with less Au NRs, whereas in samples rich in gold the suppression becomes weak. On the other hand, DLE of many samples do not seem to follow a precise trend. Only annealed samples show stable DLE, no matter the behaviour of the NBE.

A clear understanding of all the experimental results has not reached yet. A series of further investigations could be helpful for the purpose. First of all, electrical properties could be studied, too. Current-voltage curves before and after gold deposition could be used to account for possible electron transfer from gold NRs to ZnO to get stronger response in photovoltaic devices. Alternative deposition methods could be tried: for example, electrodeposition and spin-coating seem promising approaches to get more homogeneous gold distributions. The scheme of transfer processes happening between the two systems needs stronger validation. Alumina layers could be deposited on ZnO in order to get a separation from Au NRs; when the distance increases, LSPR effects that require a direct contact between the two species can be suppressed. This might help in the understanding which transfer processes are most likely to happen in the system, comparing the responses before and after the alumina layer deposition. Finally, photoinduced absorption (PIA) can be useful to investigate the interaction between gold and ZnO with the final purpose to implementing this system in solar cells

Italian Summary

La ricerca riportata in questa tesi è stata condotta presso Luleå University of Technology a Luleå (Svezia), nell'ambito del tirocinio finalizzato alla stesura della tesi magistrale per il corso di laurea in Ingegneria dei Materiali dell'Università degli Studi di Padova.

Il progetto di ricerca ha riguardato la sintesi di *nanowires* di ossido di zinco e la loro decorazione con *nanorods* di oro per applicazioni fotovoltaiche. La parte sperimentale riguarda innanzitutto la sintesi dei nanofilamenti, poi la loro decorazione e le successive caratterizzazioni, morfologiche e ottiche, mirate a individuare analogie e differenze nelle proprietà prima e dopo l'addizione di oro. La sintesi dei *nanorods* è invece avvenuta nei laboratori NanoEng del Dipartimento di Ingegneria Industriale dell'Università di Padova, a cura del prof. Alessandro Martucci e del dr. Gregorio Carolo.

L'interesse per questo progetto è legato all'importanza di aumentare l'efficienza delle celle solari, dispositivi capaci di convertire direttamente l'energia solare in elettricità per effetto fotovoltaico; il loro impiego risulta fondamentale al fine di ridurre le emissioni di CO_2 nell'atmosfera, una delle cause principali dell'effetto serra, a sua volta potenzialmente legato al surriscaldamento globale.

L'aumento di efficienza è possibile nel momento in cui venga assorbita una maggior quantità di luce solare alla base dello strato attivo della cella fotovoltaica. Nel progetto in esame, lo strato attivo è rappresentato dai nanofilamenti di ossido di zinco, mentre l'elemento che comporta un incremento nell'assorbimento di fotoni è l'oro che, sotto forma di *nanorods*, assume le caratteristiche di una nanoparticella plasmonica. I plasmoni sono oscillazioni coerenti della nuvola elettronica della nanoparticella che possono interagire con un campo elettromagnetico incidente (in questo caso la luce solare), trovandosi in condizioni di risonanza con esso a specifiche lunghezze d'onda. La particolare conformazione dei *nanorods,* geometricamente caratterizzati da due assi di simmetria, consente alla nuvola elettronica di oscillare in due possibili direzioni: una sull'asse trasversale e una su quello longitudinale. Il fenomeno di risonanza sarà allo stesso modo riconducibile a due lunghezze d'onda, dipendenti dal tipo di materiale plasmonico, dalla sua forma e dalla costante dielettrica del materiale circostante.

La prima conseguenza di questo fenomeno, denominato LSPR (Localized Surface Plasmon Resonance), è un accentuato assorbimento di luce alle lunghezze d'onda che causano la risonanza. Inoltre, vari studi sulle nanoparticelle plasmoniche hanno portato a definire il loro contributo all'interno della cella solare in quattro effetti: *scattering*, concentrazione del campo elettrico attorno alla nanoparticella, iniezione di *hot electrons* e PIRET (*Plasmon-Induced Resonance Energy Transfer*). Con varie modalità, ognuno di questi meccanismi comporta un aumento di portatori di carica nel vicino semiconduttore, i quali possono essere efficacemente utilizzati per ricavare elettricità.

La sintesi dei nanofilamenti di ZnO è avvenuta con un procedimento idrotermale in due fasi: prima è stato sintetizzato un *seed layer* su un substrato vetroso (FTO, Fluorine-doped tin oxide), poi sono stati fatti crescere i nanofilamenti su questi precursori. I provini ottenuti sono stati caratterizzati morfologicamente al SEM e con analisi XRD. Da quest'ultima è stato possibile risalire alla fase cristallina dell'ossido di zinco, che si è rivelata essere la wurtzite; inoltre, un picco di intensità molto superiore a quella degli altri, ha denotato una crescita fortemente preferenziale nella direzione (002), perpendicolare al substrato vetroso. Dalle immagini al SEM è stata visualizzata la conformazione esagonale dei nanofilamenti, tipica della fase wurtzite.

La caratterizzazione ottica si è concentrata su spettrofotometria UV-Vis e fotoluminescenza. Per quanto riguarda i nanofilamenti di ZnO, riflettanza diffusa (che comprende riflettanza e scattering) e trasmittanza hanno mostrato un annullamento del segnale a 377 nm; questa lunghezza d'onda è associata all'energia di band-gap dell'ossido di zinco, pertanto a questa energia i fotoni vengono assorbiti per creare coppie elettrone-lacuna nel semiconduttore. Misure di fotoluminescenza hanno invece l'obiettivo di sperimentare il fenomeno di ricombinazione delle coppie elettrone-lacuna. Il provino, eccitato ad una lunghezza d'onda fissa $\lambda_{exc} = 325\ nm$, emette a sua volta una radiazione caratterizzata da due picchi: uno nell'UV, definito Near Band Emission (NBE), e uno nel visibile, detto Deep Level Emission (DLE). Il primo picco è causato dalla ricombinazione di un elettrone dalla banda di conduzione con una lacuna nella banda di valenza, accompagnato dall'emissione di un fotone con energia pari a quella del band-gap del semiconduttore; il secondo, invece, rappresenta una ricombinazione mediata da livelli energetici "trappola", con emissione di fotoni meno energetici. La DLE risulta particolarmente intensa in provini con una più alta densità di difetti, in quanto

direttamente associati alla presenza di livelli trappola. Trattamenti successivi alla sintesi, come ad esempio trattamenti termici o trattamenti al plasma, consentono di ridurre la densità di difetti e dunque aumentare il rapporto delle intensità dei picchi NBE/DLE.

La deposizione della soluzione acquosa contenente *nanorods* di oro è avvenuta col solo ausilio di una pipetta per controllare la quantità di soluzione versata sul sistema FTO/ZnO. I provini presentano disomogeneità nella distribuzione dell'oro, denotata dalle diverse sfumature rossastre che colorano la superficie del vetro. La dispersione dei *nanorods* segue una trama a "goccia": dal punto in cui viene posizionato il puntale della pipetta, la soluzione si espande radialmente verso i bordi del provino. Immagini al SEM confermano una correlazione tra intensità del colore e concentrazione di *nanorods*: sfumature più scure sono riconducibili a regioni del materiale più ricche in oro.

La caratterizzazione è stata ripetuta sul sistema FTO/ZnO/Au. L'analisi XRD ha mostrato la comparsa di un picco corrispondente a un piano cristallografico dell'oro, se pur molto debole. La caratterizzazione ottica ha invece portato a risultati ben definiti e chiari. Spettri di trasmittanza evidenziano picchi di assorbimento alle lunghezze d'onda per cui sussista il fenomeno della LSPR, più evidenti in provini dalle sfumature più scure, ovvero più ricchi in oro. Ciò definisce una proporzionalità diretta tra l'assorbimento plasmonico e la quantità di *nanorods* depositati. Misure di fotoluminescenza hanno restituito risultati differenti su provini che hanno subito trattamento di *annealing* o meno. In provini non trattati, l'aggiunta di oro provoca un aumento del rapporto NBE/DLE, mentre in provini trattati la situazione è opposta, con un abbassamento del rapporto NBE/DLE. Ciò viene spiegato attraverso il fenomeno della LSPR, che in questo caso agisce come una pompa di elettroni da livelli trappola dell'ossido di zinco alla sua banda di conduzione, provocando un aumento della NBE rispetto alla DLE. L'attivazione della LSPR è mediata dall'emissione in fotoluminescenza dello stesso ZnO, in quanto alcuni dei fotoni generati dalla ricombinazione di elettroni-lacune da livelli trappola ha energie adatte ad eccitare i *nanorods* di oro in risonanza. Gli elettroni eccitati dall'oro possono passare alla banda di conduzione dell'ossido di zinco, che si trova ad un livello energetico inferiore.

Altri risultati interessanti derivano dalla fotoluminescenza in emissioni multiple, ovvero quando uno stesso provino viene eccitato e lasciato emettere in continuazione (per 21 volte consecutive), una misurazione dopo l'altra. Si è constatato che il picco della NBE

decresce se relazionato al picco della prima emissione, in misura dipendente dalla quantità di *nanorods* presenti sul provino. Con ottima ripetibilità è stato osservato che provini con alte quantità di *nanorods* mostrano picchi di NBE più stabili, mentre provini con minor concentrazione di *nanorods* rispondono con una decrescita decisa dell'intensità del picco. La complessità del fenomeno, che potrebbe comprendere il sorgere di nuove transazioni non-radiative, non consente una spiegazione teorica dello stesso; è però prerogativa di ricerche future uno studio più approfondito degli effetti della LSPR e delle interazioni tra nanoparticelle di oro e ossido di zinco.

In conclusione, i risultati più significativi conseguiti con questa ricerca sono: corretta sintesi di *nanowires* di ossido di zinco su un substrato vetroso con un processo idrotermale a due fasi; verifica sperimentale dell'assorbimento di fotoni con energia pari o superiore al band-gap da parte dei nanofilamenti; verifica sperimentale delle bande di assorbimento plasmonico dovute a fenomeni di risonanza di plasmoni superficiali dei *nanorods* di oro; osservazione di una transizione di elettroni da livelli trappola a banda di conduzione di ZnO, mediata da LSPR. Per quanto riguarda ricerche di approfondimento future, curve IV possono dimostrare l'effettivo utilizzo del *surplus* di elettroni misurando la corrente ottenuta prima e dopo decorazione; sistemi alternativi di deposizione quali elettrodeposizione e spin-coating possono essere testati al fine di promuovere una miglior omogeneità del campione; lo studio del fenomeno di LSPR e l'interazione ZnO-Au possono essere approfonditi con misure PIA (Photo-Induced Absorption) e con deposizione di un materiale isolante frapposto tra ZnO e oro, ad esempio allumina.

Bibliography

1. Towler, B. F. *The future of energy*. (Elsevier Inc., 2014).
2. Siegel, E. How Much Fuel Does It Take To Power The World? *Starts with a bang* (2017). Available at: https://www.forbes.com/sites/startswithabang. (Accessed: 28th June 2018)
3. Demirbas, A. Progress and recent trends in biofuels. *Prog. Energy Combust. Sci.* **33,** 1–18 (2007).
4. Das, U. K. *et al.* Forecasting of photovoltaic power generation and model optimization: A review. *Renew. Sustain. Energy Rev.* **81,** 912–928 (2018).
5. US Department of Commerce, N. E. S. R. L. ESRL Global Monitoring Division - Global Greenhouse Gas Reference Network.
6. Moriarty, P. & Honnery, D. What is the global potential for renewable energy? *Renew. Sustain. Energy Rev.* **16,** 244–252 (2012).
7. Jacobson, M. Z. & Delucchi, M. A. Providing all global energy with wind, water, and solar power, Part I: Technologies, energy resources, quantities and areas of infrastructure, and materials. *Energy Policy* **39,** 1154–1169 (2011).
8. U.S. Energy Information Administration. International Energy Outlook 2017. *Int. Energy Outlook* **IEO2017,** 143 (2017).
9. Letcher, T. M. *Future Energy: improved, sustainable and clean options for our planet*. (Elsevier Ltd, 2014).
10. Sayigh, A. *Comprehensive renewable energy*. *Comprehensive Renewable Energy* **1,** (2012).
11. Solar constant - MY NASA DATA. Available at: https://mynasadata.larc.nasa.gov/glossary/solar-constant-2/. (Accessed: 24th July 2018)
12. Biernat, K., Malinowski, A. & Gnat, M. The possibility of future biofuels production using waste carbon dioxide and solar energy. in *Biofuels - Economy, Environment and Sustainability* (Intech, 2013). doi:10.5772/intechopen.68815
13. Green, M. a. Solar Cells: Operating Principle: Technology and System Applications. 2 (1982). doi:10.1063/1.4922493

14. Kalogirou, S. The potential of solar industrial process heat applications. **76,** 337–361 (2003).
15. Chan, H. Y., Riffat, S. B. & Zhu, J. Review of passive solar heating and cooling technologies. *Renew. Sustain. Energy Rev.* **14,** 781–789 (2010).
16. Raisul Islam, M., Sumathy, K. & Ullah Khan, S. Solar water heating systems and their market trends. *Renew. Sustain. Energy Rev.* **17,** 1–25 (2013).
17. Panwar, N. L., Kaushik, S. C. & Kothari, S. State of the art of solar cooking: An overview. *Renew. Sustain. Energy Rev.* **16,** 3776–3785 (2012).
18. Sharon, H. & Reddy, K. S. A review of solar energy driven desalination technologies. *Renew. Sustain. Energy Rev.* **41,** 1080–1118 (2015).
19. Creutzig, F. *et al.* The underestimated potential of solar energy to mitigate climate change. *Nat. Energy* **2,** (2017).
20. Atwater, H. A. & Polman, A. Plasmonics for improved photovoltaic devices. *Nat. Mater.* **9,** 205–213 (2010).
21. Conibeer, G. Third-generation photovoltaics. *Mater. Today* **10,** 42–50 (2007).
22. Altermatt, P. P., Schenk, A., Geelhaar, F. & Heiser, G. Reassessment of the intrinsic carrier density in crystalline silicon in view of band-gap narrowing. *J. Appl. Phys.* **93,** 1598–1604 (2003).
23. Hubbard, S. *Photovoltaic Solar Energy: From Fundamentals to Applications*. **1,** (John Wiley & Sons, Ltd., 2017).
24. Mertens, K. *Photovoltaics - Fundamentals, Technology and Practice*. (John Wiley & Sons, Ltd., 2014).
25. Tran, H. N., Nguyen, V. H., Nguyen, B. H. & Vu, D. L. Light trapping and plasmonic enhancement in silicon, dye-sensitized and titania solar cells. *Adv. Nat. Sci. Nanosci. Nanotechnol.* **7,** (2016).
26. Guo, C. F., Sun, T., Cao, F., Liu, Q. & Ren, Z. Metallic nanostructures for light trapping in energy-harvesting devices. *Light Sci. Appl.* **3,** 1–12 (2014).
27. Peiris, S., Mcmurtrie, J. & Zhu, H. Metal nanoparticle photocatalysts : emerging processes for green organic synthesis. *Catal. Sci. Technol.* **6,** 320
28. Jans, H. & Huo, Q. Gold nanoparticle-enabled biological and chemical detection and analysis. *Chem. Soc. Rev.* **41,** 2849–2866 (2012).
29. Bohren, C. F. & Huffman, D. R. *Absorption and Scattering of Light by Small*

Particles. *Research supported by the University of Arizona and Institute of Occupational and Environmental Health New York WileyInterscience 1983 541 p* **1,** (1998).

30. Valenti, M., Jonsson, M. P., Biskos, G., Schmidt-Ott, A. & Smith, W. A. Plasmonic nanoparticle-semiconductor composites for efficient solar water splitting. *J. Mater. Chem. A* **4,** 17891–17912 (2016).
31. Jain, P. K., Lee, K. S., El-sayed, I. H. & El-sayed, M. A. Calculated Absorption and Scattering Properties of Gold Nanoparticles of Different Size , Shape , and Composition : Applications in Biological Imaging and Biomedicine. *J. Phys. Chem. B* 7238–7248 (2006).
32. Mertz, J. of a classical dipole near a lossless interface : a unified description. **17,** 1906–1913 (2000).
33. Bala, K. J. DDSCAT and electric field at plasmon resonance. (2010). Available at: http://juluribk.com/2010/05/26/ddscat-and-electric-field-at-plasmon-resonance/. (Accessed: 16th July 2018)
34. Jang, Y. H. *et al.* Plasmonic Solar Cells: From Rational Design to Mechanism Overview. *Chem. Rev.* **116,** 14982–15034 (2016).
35. Jeevanandam, J., Barhoum, A., Chan, Y. S., Dufresne, A. & Danquah, M. K. Review on nanoparticles and nanostructured materials: History, sources, toxicity and regulations. *Beilstein J. Nanotechnol.* **9,** 1050–1074 (2018).
36. Van der Spoel, E., Rozing, P. & Jeanine J. Nanomaterials : a review of the definitions, applications, health effects. How to implement secure development E. *Aging (Albany. NY).* **7,** 956–963 (2015).
37. Li, L., Zhai, T., Bando, Y. & Golberg, D. Recent progress of one-dimensional ZnO nanostructured solar cells. *Nano Energy* **1,** 91–106 (2012).
38. Baruah, S. & Dutta, J. Hydrothermal growth of ZnO nanostructures. *Sci. Technol. Adv. Mater.* **10,** (2009).
39. Motohashi, K., Ikeda, T., Kojima, T. M. & Suzuki, Y. Highly charged ion scattering on single-crystalline (0001) and ð 0001 Þ zinc-oxide surfaces. *Vaccum* **104,** 22–28 (2014).
40. Srikant, V. & Clarke, D. R. On the optical band gap of zinc oxide. *J. Appl. Phys.* **83,** 5447–5451 (1998).

41. Singh, J. *et al.* Synthesis, band-gap tuning, structural and optical investigations of Mg doped ZnO nanowires. *CrystEngComm* **14,** 5898–5904 (2012).
42. Anthony, S. P., Lee, J. I. & Kim, J. K. Tuning optical band gap of vertically aligned ZnO nanowire arrays grown by homoepitaxial electrodeposition. *Appl. Phys. Lett.* **90,** 19–22 (2007).
43. Khayatian, A., Kashi, M. A., Azimirad, R., Safa, S. & Akhtarian, S. F. A. Effect of annealing process in tuning of defects in ZnO nanorods and their application in UV photodetectors. *Optik (Stuttg).* **127,** 4675–4681 (2016).
44. Mangalam, V. & Pita, K. Energy Transfer Efficiency from ZnO-Nanocrystals to Eu3+ Ions Embedded in SiO2 Film for Emission at 614 nm. *Materials (Basel).* **10,** 930 (2017).
45. Louis, C. & Pluchery, O. *Gold Nanoparticles for Physics, Chemistry and Biology*. (2012). doi:10.1142
46. Benkovicova, M. *et al.* Preparation of gold nanoparticles for plasmonic applications. *Thin Solid Films* **543,** 138–141 (2013).
47. Liu, A., Wang, G., Wang, F. & Zhang, Y. Gold nanostructures with near-infrared plasmonic resonance: Synthesis and surface functionalization. *Coord. Chem. Rev.* **336,** 28–42 (2017).
48. Abidi, W. *et al.* One-pot radiolytic synthesis of gold nanorods and their optical properties. *J. Phys. Chem. C* **114,** 14794–14803 (2010).
49. Huang, X., El-Sayed, I. H., Qian, W. & El-Sayed, M. A. Cancer cell imaging and photothermal therapy in the near-infrared region by using gold nanorods. *J. Am. Chem. Soc.* **128,** 2115–2120 (2006).
50. Catchpole, K. R. & Polman, A. Design principles for particle plasmon enhanced solar cells. *Appl. Phys. Lett.* **93,** 2006–2009 (2008).
51. Wang, J., Zhang, H. Z., Li, R. S. & Huang, C. Z. Localized surface plasmon resonance of gold nanorods and assemblies in the view of biomedical analysis. *TrAC - Trends Anal. Chem.* **80,** 429–443 (2016).
52. Huang, X., Jain, P. K., El-Sayed, I. H. & El-Sayed, M. A. Plasmonic photothermal therapy (PPTT) using gold nanoparticles. *Lasers Med. Sci.* **23,** 217–228 (2008).
53. Fluorine doped Tin Oxide (FTO) Glass - Substrates | Sigma-Aldrich. Available at: https://www.sigmaaldrich.com/materials-science/material-science-

products.html?TablePage=106837645. (Accessed: 25th July 2018)

54. Ji, L. *et al.* Effect of seed layer on the growth of well-aligned ZnO nanowires. *J. Phys. Chem. Solids* **70,** 1359–1362 (2009).

55. Shaziman, S., Ismailrosdi, A. S., Mamat, M. H. & Zoolfakar, A. S. Influence of Growth Time and Temperature on the Morphology of ZnO Nanorods via Hydrothermal. *IOP Conf. Ser. Mater. Sci. Eng.* **99,** (2015).

56. Sugunan, A., Warad, H. C., Boman, M. & Dutta, J. Zinc oxide nanowires in chemical bath on seeded substrates: Role of hexamine. *J. Sol-Gel Sci. Technol.* **39,** 49–56 (2006).

57. Murphy, C. J. *et al.* Gold nanorod crystal growth: From seed-mediated synthesis to nanoscale sculpting. *Curr. Opin. Colloid Interface Sci.* **16,** 128–134 (2011).

58. Gragorio, C., Martucci, A. & Liz-Marzàn, L. M. Flow synthesis of anisotropic Au nanoparticles. (Università degli studi di Padova, 2018).

59. Lohse, S. E. & Murphy, C. J. The quest for shape control: A history of gold nanorod synthesis. *Chem. Mater.* **25,** 1250–1261 (2013).

60. Ma, Z. Y. *et al.* Applications of gold nanorods in biomedical imaging and related fields. *Chinese Sci. Bull.* **58,** 2530–2536 (2013).

61. Chou, H. T., Huang, W. H., Wu, T. M., Yu, Y. K. & Hsu, H. C. LSPR effects of Au nanoparticles/ZnO nano-composite films. *Sens. Bio-Sensing Res.* **14,** 17–20 (2017).

62. Kim, J. & Yong, K. A facile, coverage controlled deposition of Au nanoparticles on ZnO nanorods by sonochemical reaction for enhancement of photocatalytic activity. *J. Nanoparticle Res.* **14,** (2012).

63. Perumal, V. *et al.* Characterization of gold-sputtered zinc oxide nanorods—A potential hybrid material. *Nanoscale Res. Lett.* **11,** (2016).

64. Hang, D.-R. *et al.* Annealing effects on the optical and morphological properties of ZnO nanorods on AZO substrate by using aqueous solution method at low temperature. *Nanoscale Res. Lett.* **9,** 632 (2014).

65. Han, Z., Li, S., Li, J., Chu, J. & Chen, Y. Facile synthesis of ZnO nanowires on FTO glass for dye-sensitized solar cells. *J. Semicond.* **34,** (2013).

66. Muchuweni, E., Sathiaraj, T. S. & Nyakotyo, H. Low temperature synthesis of ZnO nanowires on GAZO thin films annealed at different temperatures for solar cell

application. *Mater. Sci. Semicond. Process.* **68,** 80–86 (2017).

67. Angelica, S.-T., Miki-yoshida, M., Patricia, A.-M., Pizà-Ruiz, P. & Antùnez-Flores, W. Optical Band Gap Estimation of ZnO Nanorods. **19,** 33–38 (2016).
68. Guo, M. & Zhang, X. D. Band gap widening and quantum confinement effects of ZnO Nanowires by first-principles calculation. **677,** 243–246 (2011).
69. Zeng, H. *et al.* Blue luminescence of ZnO nanoparticles based on non-equilibrium processes: Defect origins and emission controls. *Adv. Funct. Mater.* **20,** 561–572 (2010).
70. Raji, R. & Gopchandran, K. G. ZnO nanostructures with tunable visible luminescence: Effects of kinetics of chemical reduction and annealing. *J. Sci. Adv. Mater. Devices* **2,** 51–58 (2017).
71. Khan, R., Yun, J. H., Bae, K. Bin & Lee, I. H. Enhanced photoluminescence of ZnO nanorods via coupling with localized surface plasmon of Au nanoparticles. *J. Alloys Compd.* **682,** 643–646 (2016).
72. Zhang, N., Tang, W., Wang, P., Zhang, X. & Zhao, Z. In situ enhancement of NBE emission of Au-ZnO composite nanowires by SPR. *CrystEngComm* **15,** 3301–3304 (2013).
73. Chiang, T.-C., Chiu, C.-Y., Dai, T.-F., Hung, Y.-J. & Hsu, H.-C. Surface-plasmon-enhanced band-edge emission and lasing behaviors of Au-decorated ZnO microstructures. *Opt. Mater. Express* **7,** 313 (2017).
74. Lin, H. Y. *et al.* Enhancement of band gap emission stimulated by defect loss. *Opt. Express* **14,** 2372–2379 (2006).
75. Brewster, M. M., Zhou, X., Lim, S. K. & Grade, S. Role of Au in the Growth and Nanoscale Optical Properties of ZnO Nanowires. 586–591 (2011).
76. Hsieh, Y. P., Liang, C. Te, Chen, Y. F., Lai, C. W. & Chou, P. T. Mechanism of giant enhancement of light emission from Au/CdSe nanocomposites. *Nanotechnology* **18,** (2007).
77. Ruiz Peralta, M. D. L., Pal, U. & Zeferino, R. S. Photoluminescence (PL) quenching and enhanced photocatalytic activity of Au-decorated ZnO nanorods fabricated through microwave-assisted chemical synthesis. *ACS Appl. Mater. Interfaces* **4,** 4807–4816 (2012).
78. Wood, A., Giersig, M. & Mulvaney, P. Fermi level equilibration in quantum dot-

metal nanojunctions. *J. Phys. Chem. B* **105,** 8810–8815 (2001).